Time-Dependent Phenomena in Quantum Transport

Dissertation

zur Erlangung des akademischen Grades

Doctor rerum naturalium

vorgelegt von

Elham Khosravi

Fachbereich Physik

Institut für Theoretische Physik

Freie Universität Berlin

December 2011

1. Gutachter: Prof. Dr. E. K. U. Gross

2. Gutachter: Prof. Dr. F. von Oppen

Tag der mündlichen Prüfung: 16. April 2012

Abstract

The standard approach to quantum transport combines the Landauer-Büttiker formalism with ground-state density functional theory (DFT). The basic assumption of this approach is that a steady state is eventually achieved after turning on a time-independent bias. Here we show that this assumption is *not* valid in general. We identify a variety of situations where - within the approximations made - no steady state exists. In these cases a time-dependent description of transport is essential. To deal with these cases we have applied time-dependent density functional theory (TDDFT) as well as many-body perturbation theory (MBPT). For strictly non-interacting electrons, the presence of bound states in a biased system is shown analytically and numerically to lead to persistent, localized current oscillations which can be much larger than the steady part of the current. The bound-state contribution to the time-averaged density turns out to be history-dependent as well and leads to a natural definition of the bound-state occupations out of equilibrium. For the interacting case, the discontinuity of the exchange-correlation potential of DFT in the context of electron transport for an interacting nanojunction attached to biased leads, gives rise to a dynamical state characterized by correlation-induced current oscillations in the Coulomb-blockade regime. In addition, for multistable systems, the time-dependent approach describes if and how a solution of the steady-state equation can be reached in time and how to switch reversibly between the stable solutions by applying a proper time-dependent gate. From our numerical results in this regime, it turned out that even when the evolution to a steady state is expected, the time-dependent current(density) can exhibit persistent oscillations in the long-time limit within adiabatic and spatially local approximations of the time-dependent exchange-correlation potential. Furthermore, we address the fundamental issue whether the bistability phenomenon survives when dynamical exchange-correlation effects are taken into account. We compare, for a model system, TDDFT and MBPT results with results obtained by the time-dependent density matrix renormalization group (tDMRG) method to gain insight into the performance of the various approximations employed throughout the thesis.

Contents

List of Figures

List of Tables

Abbreviations

1DHM	one Dimensional Hubbard model
2B	Second Born
a.u.	atomic units
ABALDA	Adiabatic Bethe Ansatz Local Density Approximation
ALDA	Adiabatic Local Density Approximation
BALDA	Bethe Ansatz Local Density Approximation
DBRT	Double-Barrier Resonant Tunneling
DFT	Density Functional Theory
HF	Hartree-Fock
HO	Highest occupied
KB	Kadanoff-Baym
KS	Kohn-Sham
L+DFT	Landauer plus Density Functional Theory
LDA	Local Density Approximation
MBPT	Many-Body Perturbation Theory
NDR	Negative Differential Resistance
NEGF	Non-Equilibrium Green Functions
QD	Quantum Dot
QMC	Quantum Monte Carlo
TD	Time Dependent
TDDFT	Time-dependent Density Functional Theory
TDKS	Time Dependent Kohn-Sham
tDMRG	time-dependent Density-Matrix Renormalization Group
XC	Exchange-Correlation

Chapter 1

Introduction

The proposal of using single molecules as basic units (transistors, etc.) of highly miniaturized electronic devices dates back to the seminal work of Aviram and Ratner [1] in 1974, which is often cited as the birth of the research field of "molecular electronics". This is certainly a fascinating proposal, especially in view of the fact that the semiconductor industry has followed a steady path of constantly shrinking the size of devices which has been reduced to tens of nanometers so far. The suggestion of Aviram and Ratner remained a dream until the advent of scanning probe microscopes in the 1980s, which gave researchers the tools to probe individual molecules. Turning individual molecules into devices was not far behind. In 1997 two groups led by Robert Metzger [2] and Chong-Wu Zhou [3] produced the first molecular diodes. Since then there has been tremendous experimental progress, especially in the areas of metallic wires and nanotubes. However, comparison between theory and experiment has been much less satisfactory for molecular electronics.

On the theory side, the generic task is to calculate the current-voltage characteristics of a single molecule or an atomic wire connected to semi-infinite metallic leads. This task is exceedingly difficult since a non-equilibrium situation has to be treated for an extended but non-periodic system. In fact, most current ab initio treatments of transport are limited to the steady-state regime and based on the Landauer formalism combined with density functional theory (DFT). While groundstate DFT is quite reliable for calculating the electronic structure of molecules and solids, a similar quality is generally not achieved in transport calculations. The agreement between the Landauer-plus-DFT (L+DFT) approach and experiment is often poor, particularly for devices weakly coupled to the leads. From a fundamental point of view, the use of static DFT which is an equilibrium

theory is not justified to describe non-equilibrium situations.
In addition, the L+DFT approach by construction, inherits the main assumption of the Landauer formalism that for a system driven out of equilibrium by a dc bias, a steady current will eventually be achieved. In other words, the dynamical formation of a steady state does not follow from the formalism but rather constitutes an assumption.

In this thesis we study several situations in which the steady-state assumption is not valid within the approximations made. In these cases, a time-dependent (TD) description of transport is essential.

For the non-interacting case, the presence of bound states in a biased system is shown analytically and numerically to lead to persistent, localized current oscillations which can be much larger than the steady part of the current. The amplitude of these oscillations depends on the entire history of the applied potential. The bound-state contribution to the static density is history dependent as well. Moreover, the time-dependent formulation leads to a natural definition of the bound-state occupations out of equilibrium.
For the interacting case in the Coulomb-blockade regime the discontinuity of the exchange-correlation (XC) potential of DFT in the context of electron transport for an interacting nanojunction attached to biased leads gives rise to a dynamical state, characterized by correlation-induced current oscillations. In other words, by following the time evolution of an interacting nanojunction attached to biased leads, we find that, instead of evolving to a steady state, the system reaches a dynamical state characterized by current oscillations that are shown to be intimately related to Coulomb blockade. Our results establish a dynamical picture of Coulomb blockade manifesting itself as a periodic sequence of the charging and discharging of the nanostructure. In essence Coulomb blockade is due to an electrostatic barrier induced by the electrons in the device which prevents further electrons from tunneling in, unless the bias is sufficiently increased to supply the necessary charging energy of the device.

Clearly in the real world, phonon scattering will lead to the damping of the oscillations described above. However, phonon scattering occurs on the time scale of pico-seconds while the electronic oscillations have oscillation periods of femto-seconds or less. Hence, if the ultimate goal of molecular electronics is to achieve switching times on the electronic time scale, the oscillations predicted here will be very relevant.

In addition, in the interacting case, the system can exhibit multistability. In this case, the standard approach can only tell us if multiple steady-state solutions exist. Furthermore, the fixed-point theorem specifies which solutions are stable, i.e., can be calculated by iteration. However, the important question if and how these solutions can be reached through time evolution and how to switch reversibly between them can only be addressed by a time-dependent description. In particular, the time evolution determines which solution(s) are accessible by time propagation. Interestingly, our results reveal that even in the case when the fixed-point theorem predicts a solution to be stable, the time evolution of the system is not guaranteed to reach that solution: sometimes persistent oscillations can be observed. The oscillations die out provided the time-dependent gate or bias is applied in an adiabatic fashion. Furthermore, we address the fundamental issue whether the bistability phenomenon survives when dynamical XC effects are taken into account.

Finally, we study electron transport through an interacting Anderson impurity model within Time-dependent Density Functional Theory (TDDFT) and Many-Body Perturbation Theory (MBPT) frameworks. Results obtained in the groundstate, transient and steady-state regimes are compared with numerically exact time-dependent Density-Matrix Renormalization Group (tDMRG) values.

Chapter 2

Foundations of Time-Dependent Density Functional Theory

Time-dependent density functional theory is an extension of groundstate density functional theory to describe the time evolution of a quantum many-body system in terms of the time-dependent particle density. This theory constitutes an efficient way to determine the dynamics of a quantum mechanical system because the density depends only on a single coordinate $\boldsymbol{r}$, in addition to the time variable t. This is an enormous computational advantage over the direct approach of solving the time-dependent many-body Schrödinger equation because the wavefunction depends on the position of *all* electrons and time. Even putting aside the time-dependence, the problem of finding the groundstate scales exponentially with the number of electrons and becomes prohibitively expensive as the number of electrons grows.

TDDFT is founded on two basic theorems first proven by Runge and Gross [4]: (i) the one-to-one correspondence between time-dependent densities and local external potentials for a given initial state (ii) the time-dependent density of a system of interacting electrons can be obtained from a fictitious system of non-interacting electrons moving in a time-dependent effective potential, whose density is precisely that of the real system.

Historically, the first applications of time-dependent DFT were performed by Ando [5, 6], Peuckert [7], and Zangwill and Soven [8] where the existence of a time-dependent Kohn-Sham (KS) theorem was assumed. The first significant steps towards a rigorous foundation of TDDFT were taken by Deb and Ghosh [9–12] for time-periodic potentials and by Bartolotti [13] for adiabatic processes. The breakthrough for modern TDDFT

was achieved in 1984 when Runge and Gross [4] proved the uniqueness of the mapping between time-dependent densities and potentials. However, to establish a time-dependent KS (TDKS) scheme they had to postulate non-interacting v-representability. It was shown later by van Leeuwen [14] that under mild restrictions on the initial states and boundary conditions it is always possible to find an effective single-particle potential which yields a given density of an interacting many-particle system. This solved the long standing v-representability problem of TDDFT and provided the full legitimation for the TDDFT approach. In this chapter we give a short outline of the basic foundations of time-dependent DFT.

2.1 Runge-Gross Theorem

The time-dependent extension of the Hohenberg-Kohn theorem of static DFT is directly based on the many-body Schrödinger equation

$$i\frac{\partial}{\partial t}|\Psi(t)\rangle = \hat{H}(t)|\Psi(t)\rangle\cdot \tag{2.1}$$

This is a first-order differential equation in time and hence the initial wavefunction must be specified

$$|\Psi(t=t_0)\rangle = |\Psi_0\rangle\cdot \tag{2.2}$$

For a system of N nonrelativistic electrons, mutually interacting via the Coulomb repulsion, in a time-dependent external potential, the many-body Hamiltonian $\hat{H}$ reads

$$\hat{H} = \hat{T} + \hat{V}_{ee} + \hat{V}_{\text{ext}} \tag{2.3}$$

where $\hat{T}$ describes the kinetic energy of the electrons

$$\hat{T} = -\frac{1}{2}\sum_{i=1}^{N}\nabla_i^2\cdot \tag{2.4}$$

The electron-electron Coulomb repulsion is given by

$$\hat{V}_{ee} = -\frac{1}{2}\sum_{i\neq j}^{N}\frac{1}{|\boldsymbol{r}_i - \boldsymbol{r}_j|} \tag{2.5}$$

where the factor of 1/2 avoids double counting. Finally, we consider time-dependent potentials of the form

$$\hat{V}_{\text{ext}} = \sum_{i=1}^{N} v_{\text{ext}}(\boldsymbol{r}_i, t) \tag{2.6}$$

which are assumed to be Taylor expandable around the initial time t_0, i.e.,

$$v_{\text{ext}}(\boldsymbol{r}, t) = \sum_{k}^{\infty} \frac{v_k(\boldsymbol{r}, t_0)}{k!}(t - t_0)^k \quad \text{with} \quad v_k(\boldsymbol{r}, t_0) = \frac{\partial^k}{\partial t^k} v_{\text{ext}}(\boldsymbol{r}, t)\Big|_{t=t_0} \tag{2.7}$$

For different systems, *only* the time-dependent external potential $v_{\text{ext}}(\boldsymbol{r}, t)$ and the particle number N differ in the many problems. As the system evolves in time from some initial point under the influence of the external potential, its one-particle density changes. This electron density is given by

$$n(\boldsymbol{r}, t) = N \int \mathrm{d}^3 r_2 \ldots \int \mathrm{d}^3 r_N |\Psi(\boldsymbol{r}, \boldsymbol{r}_2, \ldots, \boldsymbol{r}_N, t)|^2 \tag{2.8}$$

where $n(\boldsymbol{r}, t)\mathrm{d}^3 r$ is the probability of finding any electron in a region $\mathrm{d}^3 r$ around $\boldsymbol{r}$ at time t. The density is normalized to the number of electrons

$$N = \int \mathrm{d}^3 r \; n(\boldsymbol{r}, t). \tag{2.9}$$

The analog of the Hohenberg-Kohn theorem for time-dependent problems is the one-to-one correspondence proven by Runge and Gross [4]. The theorem states that the densities $n(\boldsymbol{r}, t)$ and $n'(\boldsymbol{r}, t)$ evolving from a common initial state $|\Psi_0\rangle$ under the influence of two Taylor expandable potentials $v_{\text{ext}}(\boldsymbol{r}, t)$ and $v'_{\text{ext}}(\boldsymbol{r}, t)$ eventually differ provided that the potentials differ by more than a purely time-dependent function:

$$v_{\text{ext}}(\boldsymbol{r}, t) - v'_{\text{ext}}(\boldsymbol{r}, t) \neq c(t) \tag{2.10}$$

This is a physical condition, because by adding a *purely time-dependent* constant to the potential the wavefunction changes by just a purely time-dependent phase and hence the resulting density remains unchanged.

Note that Eq. 2.10 assures that there exists an integer $k > 0$ for which the Taylor coefficients (see Eq. 2.7) $v_k(\boldsymbol{r}, t_0)$ and $v'_k(\boldsymbol{r}, t_0)$ differ by more than a constant.

Under these conditions, there is a one-to-one mapping between time-dependent densities and potentials, which implies that the potential is a functional of the density. The proof

of the theorem employs the continuity equation, i.e.,

$$\frac{\partial n(\boldsymbol{r},t)}{\partial t} = -\nabla \cdot \boldsymbol{j}(\boldsymbol{r},t). \tag{2.11}$$

This identity expresses the conservation of the total particle: the change in the number of electrons within a certain volume equals the flux through it surfaces. Here $\boldsymbol{j}(\boldsymbol{r},t)$ is the current density and is given by

$$\boldsymbol{j}(\boldsymbol{r},t) = N \int \mathrm{d}^3 r_2 \ldots \int \mathrm{d}^3 r_N \mathrm{Im}\left\{\Psi(\boldsymbol{r},\boldsymbol{r}_2,\ldots,\boldsymbol{r}_N,t)\nabla\Psi^*(\boldsymbol{r},\boldsymbol{r}_2,\ldots,\boldsymbol{r}_N,t)\right\} \tag{2.12}$$

As the first step the Runge-Gross theorem shows

$$\begin{aligned}\frac{\partial}{\partial t}[\boldsymbol{j}(\boldsymbol{r},t) - \boldsymbol{j}'(\boldsymbol{r},t)]_{t=t_0} &= -n(\boldsymbol{r},t_0)\nabla\left\{v_{\mathrm{ext}}(\boldsymbol{r},t_0) - v'_{\mathrm{ext}}(\boldsymbol{r},t_0)\right\} \\ &= -n(\boldsymbol{r},t_0)\nabla\left\{v_0(\boldsymbol{r},t_0) - v'_0(\boldsymbol{r},t_0)\right\}\end{aligned} \tag{2.13}$$

Thus we see that if, already at the initial time, the two potentials differ (by more than just a constant) the first derivative of the current densities must differ infinitesimally later than t_0.

Otherwise, we take a higher time derivative

$$\frac{\partial^{k+1}}{\partial t^{k+1}}[\boldsymbol{j}(\boldsymbol{r},t) - \boldsymbol{j}'(\boldsymbol{r},t)]_{t=t_0} = -n(\boldsymbol{r},t_0)\nabla\left\{v_k(\boldsymbol{r},t_0) - v'_k(\boldsymbol{r},t_0)\right\}. \tag{2.14}$$

As there is at least one integer k for which $v_k(\boldsymbol{r},t_0) - v'_k(\boldsymbol{r},t_0)$ is not constant, the current densities $\boldsymbol{j}(\boldsymbol{r},t)$ and $\boldsymbol{j}'(\boldsymbol{r},t)$ deviate for $t > t_0$. This is the first part of the theorem, which establishes a one-to-one correspondence between current densities and external potentials.

In the second part, the proof is extended to the densities. Using Eq. 2.14 and the continuity equation Eq. 2.11 we have

$$\frac{\partial^{k+2}}{\partial t^{k+2}}[n(\boldsymbol{r},t) - n'(\boldsymbol{r},t)]_{t=t_0} = \nabla \cdot [n(\boldsymbol{r},t_0)\nabla\ \left\{v_k(\boldsymbol{r},t_0) - v'_k(\boldsymbol{r},t_0)\right\}]. \tag{2.15}$$

For physically reasonable potentials (e.g. potentials which are produced by moving charges) in both the primed and unprimed system it can be shown that the right hand side of Eq. 2.15 cannot vanish identically. Consequently, the densities $n(\boldsymbol{r},t)$ and $n'(\boldsymbol{r},t)$ become different infinitesimally later than t_0. In other words, the time-dependent density $n(\boldsymbol{r},t)$ uniquely determines the time-dependent potential $v_{\mathrm{ext}}(\boldsymbol{r},t)$ up to a purely time-dependent function $c(t)$. The wavefunction is in turn determined up to a time-dependent

phase. However, the ambiguity in the phase cancels when constructing expectation values of any quantum mechanical operator. Thus the expectation value of any operator is a unique functional of the time-dependent density and initial state.

2.2 Time-Dependent Kohn-Sham Equations

The Runge-Gross theorem established the one-to-one correspondence between time-dependent potentials and time-dependent densities for an arbitrary but fixed particle interaction $\hat{V}_{ee}$. In particular, the interaction can be zero, corresponding to non-interacting electrons. Therefore, one can relate interacting and non-interacting systems with identical time-dependent densities. Suppose we are interested in an interacting system with a given time-dependent density $n(\boldsymbol{r},t)$. Due to the one-to-one correspondence, the time-dependent effective potential of a *non-interacting* system that reproduces the density $n(\boldsymbol{r},t)$ of the *interacting* system (starting in the initial state Φ_0), is uniquely determined. As a result, one can introduce a fictitious system of non-interacting electrons that satisfy TDKS equations:

$$i\frac{\partial}{\partial t}\psi_j(\boldsymbol{r},t) = \big(-\frac{\nabla^2}{2} + v_{\mathrm{KS}}[n](\boldsymbol{r},t)\big)\psi_j(\boldsymbol{r},t) \qquad j=1,\ldots,N. \tag{2.16}$$

By construction, the density

$$n(\boldsymbol{r},t) = \sum_{j=1}^{N} |\psi_j(\boldsymbol{r},t)|^2 \tag{2.17}$$

of the non-interacting KS system corresponds to the interacting density. In analogy to groundstate DFT, the effective single-particle potential $v_{\mathrm{KS}}(\boldsymbol{r},t)$ is written according to

$$v_{\mathrm{KS}}(\boldsymbol{r},t) = v_{\mathrm{ext}}(\boldsymbol{r},t) + v_{\mathrm{H}}(\boldsymbol{r},t) + v_{\mathrm{xc}}(\boldsymbol{r},t), \tag{2.18}$$

where the first term is the external potential while the second one

$$v_{\mathrm{H}}(\boldsymbol{r},t) = \int \mathrm{d}^3r' \frac{n(\boldsymbol{r}',t)}{|\boldsymbol{r}-\boldsymbol{r}'|} \tag{2.19}$$

denotes the time-dependent Hartree potential, describing the potential produced by of classical electronic charge distributions. The only unknown piece is the exchange-correlation potential , v_{xc} which is a functional of the *entire* history of the density,

$n(\boldsymbol{r}, t)$, the initial wavefunction of the interacting system $|\Psi_0\rangle$, and the initial KS wavefunction $|\Phi_0\rangle$. This functional is an extremely complex object. In practice, it has to be approximated.

To conclude this section, a few remarks about some properties of the TDKS scheme are in order:

i) *Initial-state dependence:* Due to the fact that the one-to-one correspondence is established for fixed initial states, the TDKS potential in general is not only a functional of the time-dependent density, but also a functional of the initial many-body wavefunction $|\Psi_0\rangle$ and the initial KS Slater determinant $|\Phi_0\rangle$. This is a serious complication, compared to groundstate DFT. It means that for every possible initial wavefunction, a different density functional is required, a property that would render TDDFT useless in practice. Fortunately, the initial-state dependence of the TDKS potential drops out provided the initial state is a nondegenerate groundstate. In this case the initial wavefunction is a functional of the groundstate density according to the Hohenberg-Kohn theorem of static DFT [15] and hence the TDKS potential becomes a functional of the time-dependent density only. Most practical calculations are covered by this case.

ii) *Time-dependent potential:* The Runge-Gross theorem is proven for Taylor-expandable potentials. Consequently, time-dependent potentials which contain an adiabatic switching of the form $\exp(-\gamma|t|)$ with $\gamma \to 0$ are not covered by the KS scheme. Such potentials possess an essential singularity at the initial time $t_0 = -\infty$.

iii) *Construction of potential*: The one-to-one correspondence establishes only the *uniqueness* of the potential that generates a given density from a given initial state, but does not prove its *existence*. In the original work of Runge and Gross the non-interacting v-representability was postulated, i.e. the existence of such a potential was assumed. It was demonstrated later by van Leeuwen [14], that under mild restrictions on the initial states and boundary conditions such a potential can always be found. A feature of this proof is that it leads to the explicit construction of the KS potential.

iv) *Time-dependent current:* The first step of the Runge-Gross proof provided a one-to-one mapping between the external potential and the current-density, while the second step invoked continuity, with the help of a surface condition, to prove the one-to-one density-potential mapping. In fact in TDDFT only the longitudinal parts of the interacting current-density and the KS current-density are clearly equivalent, because both

current-densities satisfy the continuity equation with the same density, i.e.

$$\frac{\partial n(\boldsymbol{r},t)}{\partial t} = -\nabla \cdot \boldsymbol{j}(\boldsymbol{r},t) = -\nabla \cdot \boldsymbol{j}_{\mathrm{KS}}(\boldsymbol{r},t) \tag{2.20}$$

However, they may differ by a purely transversal component, i.e., $\boldsymbol{j}(\boldsymbol{r},t) = \boldsymbol{j}_{\mathrm{KS}}(\boldsymbol{r},t) + \boldsymbol{j}_{\mathrm{xc}}(\boldsymbol{r},t)$, where

$$\boldsymbol{j}_{\mathrm{xc}}(\boldsymbol{r},t) = \nabla \times K(\boldsymbol{r},t) \tag{2.21}$$

with some $K(\boldsymbol{r},t)$.

In the context of quantum transport, however, one is interested in the total current I through a device which can be computed from a surface integral of the form

$$I(t) = e \int \boldsymbol{j}_{\mathrm{KS}}(t) \cdot \hat{\mathbf{n}}\, dS \tag{2.22}$$

where $\hat{\mathbf{n}}$ is the unit vector perpendicular to the surface element.

Note that if we choose a plane perpendicular to the longitudinal geometry of the system for the surface S, only the longitudinal current density contributes to the integral and hence TDDFT yields, in principle, the correct (time-dependent) total current of the system.

Chapter 3

A Practical Approach to Time-dependent Quantum Transport

To address electronic transport on the molecular scale theoretically, one needs a full quantum description of the electronic dynamics (see for example Ref. [16]) . The typical experimental setup is displayed in Fig. 3.1 where a central region C of meso- or nanoscopic size, is coupled to two metallic electrodes which play the role of charge reservoirs. The whole system is initially (at time $t_0 < 0$) in a well defined equilibrium configuration, described by a *unique* temperature and chemical potential. Then the system is driven out of equilibrium by exposing the electrons to an external time-dependent potential which is local in time and space, e.g., an electric field can be applied by putting the system between two capacitor plates far away from the system boundaries. For metal-

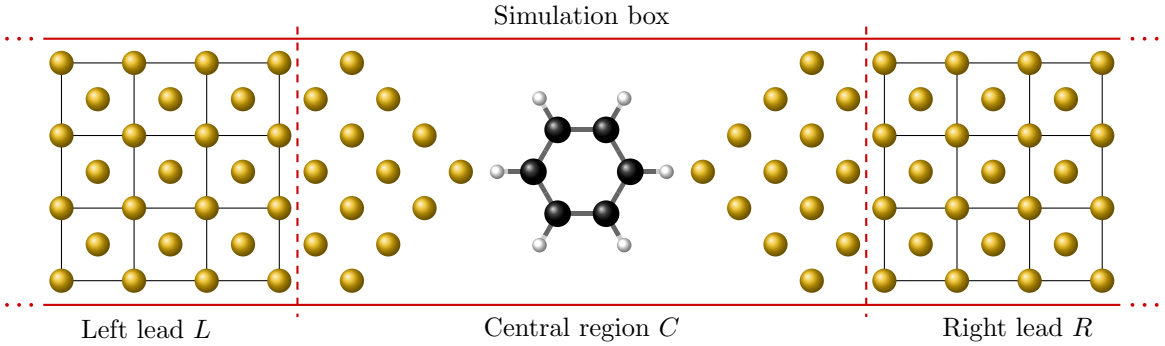

FIGURE 3.1: Sketch of the experimental setup described in the main text. A central region which also includes few layers of the left (L) and right (R) electrodes is coupled to macroscopically large metallic reservoirs.

lic leads the dynamical formation of dipole layers screens the potential drop along the electrodes such that the potential drop is entirely limited to the central region (which also includes few atomic layers of the left and right tip). Therefore, the total effect of the applied bias turns out to be a uniform shift in the potential of the left (L) and right (R) electrodes. As the system size increases, the remote parts are less disturbed by the junction, and the density inside the electrodes approaches the equilibrium bulk density.

On the theoretical side, there has been considerable activity to describe transport phenomena through systems like the one in Fig. 3.1. Most approaches are limited to the steady-state regime and are based on the combination of the Landauer-Büttiker formula [17–25] with (static) DFT which allows to take the atomistic structure of both the molecule and the contacts into account. In these approaches, exchange and correlation is approximated by the static Kohn-Sham potential and the charge density is obtained self-consistently in the presence of the steady current. Furthermore, the transmission functions computed from static DFT have resonances at the non-interacting Kohn-Sham excitation energies which in general do not coincide with the true excitation energies. For a recent critical review of this methodology, the reader is referred to Ref. [26]. On the other hand, approaches based on the TDDFT formulation to describe quantum transport, as opposed to the static DFT formulation, access the true excitation energies of interacting systems [27]. In addition, as these approaches are not limited to the steady-state regime, one can study transients and also investigate situations where no steady state develops. This theory is, therefore, in principle well suited for the treatment of nonequilibrium transport problems [28].

It is worth mentioning at this point that using non-equilibrium Green functions (NEGF) techniques, as an alternative approach to quantum transport, it has been shown [29] that a steady-state regime develops provided that 1) the KS Hamiltonian *globally* converges to an asymptotic KS Hamiltonian in the long time limit 2) the electrodes form a continuum of states , and 3) the local density of states is a smooth function in the central region. The question if and how the system dynamically reaches a steady state will be addressed further in the next chapters.

In this chapter, a practical scheme to study quantum transport in the time domain, originally proposed by Kurth et al. [30] , is presented. The main idea is to propagate the KS orbitals in region C only, without dealing explicitly with the infinite and non-periodic system.

3.1 Quantum Transport: A practical Scheme

As our lead-device-lead system is non-periodic and infinite, the transport problem seems exceedingly difficult to treat. However, as we will see below, in practice we only need to deal with a finite portion of the system, namely the device region. The numerical method is based on the propagation of the wavefunction projected in the central region C by applying the correct boundary conditions and by treating the lead-device interaction in an efficient way [30].

We consider non-magnetic systems at zero temperature and we denote with $\psi(\boldsymbol{r},0) \equiv \langle \boldsymbol{r}|\psi(0)\rangle$ the eigenstates of $\boldsymbol{H}^0 \equiv \boldsymbol{H}(t<0)$, here we set t_0 to zero. Note that $\boldsymbol{H}(t)$ is a single-particle Hamiltonian, i.e. it represents either a strictly non-interacting system or the KS Hamiltonian of an interacting system. The time-dependent density can then be computed in the usual way by $n(\boldsymbol{r},t) = \sum_{\text{occ}} |\psi(\boldsymbol{r},t)|^2$, where the sum is over the occupied wavefunctions and $|\psi(t)\rangle$ is the solution of the Schrödinger equation $i\frac{\partial}{\partial t}|\psi(t)\rangle = \boldsymbol{H}(t)|\psi(t)\rangle$.

The total current can be written as $I_\alpha(t)$ as

$$I_\alpha(t) = -e\sum_{\text{occ}} \int_{S_\alpha} \mathrm{d}\sigma\, \hat{\mathbf{n}} \cdot \mathrm{Im}\left[\psi^*(\boldsymbol{r},t)\boldsymbol{\nabla}\psi(\boldsymbol{r},t)\right] \tag{3.1}$$

where $\hat{\mathbf{n}}$ is the unit vector perpendicular to the surface element $\mathrm{d}\sigma$ and the surface S_α is perpendicular to the longitudinal geometry of our system.

Note that the Hamiltonian $\boldsymbol{H}(t)$ is a matrix of infinite dimension, and to propagate the wavefunction in practice we partition the system into three regions: a central region C consisting of the junction and a few atomic layers of the left and right electrodes and two regions L, R which describe the left and right bulk electrodes. The time-dependent single-particle Schrödinger equation then reads

$$i\frac{\partial}{\partial t}\begin{bmatrix} |\psi_L(t)\rangle \\ |\psi_C(t)\rangle \\ |\psi_R(t)\rangle \end{bmatrix} = \begin{bmatrix} \boldsymbol{H}_{LL}(t) & \boldsymbol{H}_{LC} & \mathbf{0} \\ \boldsymbol{H}_{CL} & \boldsymbol{H}_{CC}(t) & \boldsymbol{H}_{CR} \\ \mathbf{0} & \boldsymbol{H}_{RC} & \boldsymbol{H}_{RR}(t) \end{bmatrix} \begin{bmatrix} |\psi_L(t)\rangle \\ |\psi_C(t)\rangle \\ |\psi_R(t)\rangle \end{bmatrix}, \tag{3.2}$$

In general, the lead-lead coupling matrices ($\boldsymbol{H}_{LR}, \boldsymbol{H}_{RL}$) are negligible and due to the local multiplicative nature of the Kohn-Sham potential the lead-device coupling matrices ($\boldsymbol{H}_{CL}$, $\boldsymbol{H}_{CR}$, $\boldsymbol{H}_{LC}$ and $\boldsymbol{H}_{RC}$) are time-independent. Here $|\psi_\alpha(t)\rangle$ is the projected wavefunction onto the region $\alpha = L, R, C$. Note that in the case of interacting electrons

$\boldsymbol{H}$ can be replaced by $\boldsymbol{H}_{\mathrm{KS}}$, in this case $|\psi_\alpha(t)\rangle$ is the Kohn-sham wavefunction projected onto the region α.

In order to solve Eq. 3.2 we introduce the retarded Green function $\boldsymbol{g}^{\mathrm{R}}_{\alpha\alpha}$ which is a solution of

$$\left(i\frac{\partial}{\partial t} - \boldsymbol{H}_{\alpha\alpha}(t)\right)\boldsymbol{g}^{\mathrm{R}}_{\alpha\alpha}(t,t') = \delta(t-t') \tag{3.3}$$

with the boundary conditions $\boldsymbol{g}^{\mathrm{R}}_{\alpha\alpha}(t^+,t) = -i$ and $\boldsymbol{g}^{\mathrm{R}}_{\alpha\alpha}(t,t^+) = 0$.
Then, from $i\frac{\partial}{\partial t}|\psi_\alpha(t)\rangle = \boldsymbol{H}_{\alpha\alpha}|\psi_\alpha(t)\rangle + \boldsymbol{H}_{\alpha C}|\psi_C(t)\rangle$ for lead $\alpha = L, R$, the time-dependent wavefunction in the leads is given by

$$|\psi_\alpha(t)\rangle = i\boldsymbol{g}^{\mathrm{R}}_{\alpha\alpha}(t,0)|\psi_\alpha(0)\rangle + \int_0^t \mathrm{d}t'\boldsymbol{g}^{\mathrm{R}}_{\alpha\alpha}(t,t')\boldsymbol{H}_{\alpha C}|\psi_C(t')\rangle. \tag{3.4}$$

Using Eq. 3.4, the equation for ψ_C can be written as

$$i\frac{\partial}{\partial t}|\psi_C(t)\rangle = \boldsymbol{H}_{CC}(t)|\psi_C(t)\rangle + \int_0^t \mathrm{d}t'\boldsymbol{\Sigma}^{\mathrm{R}}(t,t')|\psi_C(t')\rangle + i\sum_{\alpha=L,R}\boldsymbol{H}_{C\alpha}\boldsymbol{g}^{\mathrm{R}}_{\alpha\alpha}(t,0)|\psi_\alpha(0)\rangle, \tag{3.5}$$

where the term $\boldsymbol{\Sigma}^{\mathrm{R}} = \sum_{\alpha=L,R}\boldsymbol{H}_{C\alpha}\boldsymbol{g}^{\mathrm{R}}_{\alpha\alpha}\boldsymbol{H}_{\alpha C}$ is called the retarded embedding self energy.

Equation 3.5 reformulates the time-dependent Schrödinger equation (Eq. 3.2) of the full system in terms of an equation for the central (device) region *only*. In fact, Eq. 3.5 has the structure of a time-dependent Schrödinger equation with two extra terms which mediate the coupling to the leads in a formally exact way. The first additional term is called the "memory integral", since it requires the knowledge of the wavefunction in the central region at all previous times during the propagation. The second term, describes the injection of particles into the central region due to the time evolution of the lead part of the initial wavefunction. Here, we wish to point out that these memory effects are of different origin than those which are usually discussed in the context of TDDFT arising from the dependence of the exchange-correlation functional on the full history of the time-dependent density.

Since Eq. 3.5 is first order with respect to the time coordinate, we need to specify an initial state to be propagated in time. In principle one can start from any initial state, but in this thesis we are interested in studying the time evolution of systems perturbed out of their equilibrium groundstate. As discussed in Chapter 2, by this choice the initial-state dependence of the time-dependent Kohn-Sham potential drops out. In the

case of a noninteracting system or effectively noninteracting Kohn-Sham system, the groundstate is the Slater determinant of the occupied eigenstates of the full, extended Hamiltonian in equilibrium, $\boldsymbol{H}^0$. Below we show how these eigenstates can be obtained and propagated in time without having to deal explicitly with the extended Hamiltonian.

3.1.1 Computation of the Groundstate

Let $\psi^{(0)}_{Ej}(\boldsymbol{r}) \equiv \psi_{Ej}(\boldsymbol{r}, t=0)$ be the j-th degenerate eigenstate of energy E of the Hamiltonian $\boldsymbol{H}^0$ in equilibrium and $\boldsymbol{\mathcal{G}}$ denote the Green functions the undisturbed system which only depends on the difference $t-t'$. In absence of magnetic fields $\boldsymbol{H}^0$ is invariant under time-reversal and the imaginary part of the Fourier transformed $\boldsymbol{\mathcal{G}}^{\mathrm{R}}$ is simply given by

$$-\frac{1}{\pi}\mathrm{Im}\left[\langle \boldsymbol{r}|\boldsymbol{\mathcal{G}}(E)|\boldsymbol{r}'\rangle\right] = \sum_{E'}\delta(E-E')\sum_{j=1}^{d_{E'}}\psi^{(0)}_{E'j}(\boldsymbol{r})\psi^{*(0)}_{E'j}(\boldsymbol{r}')\,. \tag{3.6}$$

It can be shown that

$$-\frac{1}{\pi}\int_C \mathrm{d}\boldsymbol{r}\int_C \mathrm{d}\boldsymbol{r}' a^*_{El}(\boldsymbol{r})\mathrm{Im}\left[\langle \boldsymbol{r}|\boldsymbol{\mathcal{G}}(E)|\boldsymbol{r}'\rangle\right] a_{El'}(\boldsymbol{r}') = \delta_{ll'}\lambda_l^2(E)\sum_{E'}\delta(E-E'), \tag{3.7}$$

where $a_{El}(\boldsymbol{r})$ are new eigenfunctions defined as $a_{El}(\boldsymbol{r}) = \sum_{n=1}^{d_E} a_n^{(l)}(E)\psi^{(0)}_{En}(\boldsymbol{r})$. Therefore Eq. 3.7 shows explicitly that the functions $a_{Ej}(\mathbf{r})$ diagonalize $\mathrm{Im}\left[\boldsymbol{\mathcal{G}}_{CC}(E)\right]$ in the central region and that the eigenvalues are positive. Since any linear combination of degenerate eigenstates is again an eigenstate, diagonalizing $\mathrm{Im}\left[\boldsymbol{\mathcal{G}}_{CC}(E)\right]$ gives us one set of linearly independent, degenerate eigenstates of energy E. In our practical implementation we diagonalize

$$-\frac{1}{\pi D_C(E)}\mathrm{Im}\left[\boldsymbol{\mathcal{G}}_{CC}(E)\right] \tag{3.8}$$

where $D_C(E) = -\frac{1}{\pi}\mathrm{Tr}\left\{\mathrm{Im}\left[\boldsymbol{\mathcal{G}}_{CC}(E)\right]\right\}$ is the total density of states in the central region. Clearly, if we use N grid points to describe the central region, the diagonalization in principle gives N eigenvectors but only the ones with non-vanishing eigenvalues have the physical meaning of extended eigenstates at a given energy E. Note that diagonalization of Eq. 3.8 gives eigenvectors which are normalized to the central region. To normalize the eigenfunctions to the whole system, we match the wavefunction for the central region to the known form of the wavefunction in the macroscopic leads.

As this procedure for finding the extended eigenstates requires an inversion and diagonalization of an $N \times N$ matrix, it becomes computationally too expensive for more

than one dimensional systems. For two and three dimensional systems one can use the Lippmann-Schwinger approach with the restriction that the leads must be symmetric (for a detailed discussion of the Lippmann-Schwinger approach see Ref. [31] for example).

It should be emphasized that the two procedures mentioned above for calculations of eigenstates of the extended system in practice are only capable of finding the eigenstates with eigenenergies in the continuous part of the spectrum. This is due to the sharp peak of the delta function in the discrete part of the spectrum. Eigenstates in the discrete part of the spectrum can be found instead from the static Schrödinger equation for the full system: $\boldsymbol{H}^0\psi^{(0)} = E\psi^{(0)}$. Using the block structure of the Hamiltonian (see Eq. 3.2) an effective static Schrödinger equation for the central region only is found:

$$\left(\boldsymbol{H}^0_{CC} + \sum_{\alpha=L,R} \boldsymbol{H}_{C\alpha}\frac{1}{E\mathbf{1}_{\alpha\alpha} - \boldsymbol{H}_{\alpha\alpha}}\boldsymbol{H}_{\alpha C}\right)|\psi^{(0)}_C\rangle = E|\psi^{(0)}_C\rangle. \tag{3.9}$$

This equation has solutions only for certain values of E which are the *discrete* eigenenergies of the full Hamiltonian $\boldsymbol{H}$. As the effective Hamiltonian itself depends on the eigenenergy E through the real part of the retarded/advanced self-energy in equilibrium, to solve the problem we first need to find the roots of the equation

$$det\left(\boldsymbol{H}^0_{CC} + \sum_{\alpha=L,R} \boldsymbol{H}_{C\alpha}\frac{1}{E\mathbf{1}_{\alpha\alpha} - \boldsymbol{H}_{\alpha\alpha}}\boldsymbol{H}_{\alpha C} - E\mathbf{1}_{CC}\right) = 0 \tag{3.10}$$

The resulting energies E are then inserted into Eq. 3.9, and the corresponding bound eigenstates are found. Bound states as well as fully reflected waves will contribute to the density and the current as we will see in next the chapter.

3.1.2 Algorithm for the Time Evolution

In order to calculate the longitudinal current in an electrode-junction-electrode system we need to have the time-dependent wavefunction. In this Section we describe an algorithm well suited for delocalized initial states, as well as for localized ones, evolving with a time-dependent Hamiltonian.

Let $\boldsymbol{H}(t)$ be the time-dependent Hamiltonian of the system. The wavefunction of the system at time step $m+1$, $|\psi(t_{m+1} = (m+1)\Delta t)\rangle = |\psi^{(m+1)}\rangle$ can be calculated knowing

the wavefunction at the previous time step m, $|\psi^{(m)}\rangle$

$$|\psi^{(m+1)}\rangle = \boldsymbol{U}(t_{m+1}, t_m)|\psi^{(m)}\rangle \tag{3.11}$$

where $\boldsymbol{U}(t, t')$ is the evolution operator of the system. Among different existing approximations for the evolution operator [32] we use the Crank-Nicholson evolution operator which is norm-conserving (unitary) and second-order in time and is applicable when the system has time-reversal symmetry.

The Crank-Nicholson evolution operator reads

$$\boldsymbol{U}_{CN} = \frac{1 - i\delta\boldsymbol{H}^{(m)}}{1 + i\delta\boldsymbol{H}^{(m)}} \tag{3.12}$$

here $\delta = \Delta t/2$, Δt being the time step. The Hamiltonian $\boldsymbol{H}^{(m)} = \boldsymbol{H}(t_m + \delta)$ is calculated from

$$\boldsymbol{H}^{(m)} = \frac{1}{2}\left[\boldsymbol{H}(t_{m+1}) + \boldsymbol{H}(t_m)\right]. \tag{3.13}$$

The explicitly treated region C includes the first few atomic layers of the left and right electrodes. The boundaries of the central region are chosen such that the density at the interface of C and the lead α is accurately described by an equilibrium bulk density of the lead. This guarantees that all essential physical scattering processes are contained in region C. Considering metallic electrodes it is reasonable to assume perfect instantaneous screening in the leads. With this approximation, the TDKS potential in the leads $v_{\mathrm{KS},\alpha}(\boldsymbol{r}, t) = v_{\mathrm{ext},\alpha}(\boldsymbol{r}, t) + v_{\mathrm{H},\alpha}(\boldsymbol{r}, t) + v_{\mathrm{xc},\alpha}(\boldsymbol{r}, t)$ reduces to $v_{\mathrm{KS},\alpha}(\boldsymbol{r}, t) = v_{\mathrm{ext},\alpha}(\boldsymbol{r}, 0) + v_{\mathrm{H},\alpha}(\boldsymbol{r}, 0) + v_{\mathrm{xc},\alpha}(\boldsymbol{r}, 0) + U_\alpha(t)$. Therefore, $\boldsymbol{H}_{\alpha\alpha}(t)$ can be written as the sum of the static part of the lead Hamiltonian $\boldsymbol{H}^0_{\alpha\alpha} = \boldsymbol{H}_{\alpha\alpha}(0)$ and an explicitly time-dependent term $\boldsymbol{U}_\alpha(t)$, i.e., $\boldsymbol{H}_{\alpha\alpha}(t) = \boldsymbol{H}^0_{\alpha\alpha} + \boldsymbol{U}_\alpha(t)$. In configuration space $\boldsymbol{U}_\alpha(t)$ is diagonal at any time t and spatially constant for metallic electrodes. Thus, $\boldsymbol{U}_\alpha(\boldsymbol{r}, t) = U_\alpha(t)\mathbf{1}_{\alpha\alpha}$. We write $\boldsymbol{H}(t) = \tilde{\boldsymbol{H}}(t) + \boldsymbol{U}(t)$ with

$$\tilde{\boldsymbol{H}}(t) = \begin{bmatrix} \boldsymbol{H}^0_{LL} & \boldsymbol{H}_{LC} & \mathbf{0} \\ \boldsymbol{H}_{CL} & \boldsymbol{H}_{CC}(t) & \boldsymbol{H}_{CR} \\ \mathbf{0} & \boldsymbol{H}_{RC} & \boldsymbol{H}^0_{RR} \end{bmatrix}, \quad \text{and} \quad \boldsymbol{U}(t) = \begin{bmatrix} U_L(t)\mathbf{1}_{LL} & \mathbf{0} & \mathbf{0} \\ \mathbf{0} & \mathbf{0} & \mathbf{0} \\ \mathbf{0} & \mathbf{0} & U_R(t)\mathbf{1}_{RR} \end{bmatrix}. \tag{3.14}$$

In this way, the only term in $\tilde{\boldsymbol{H}}(t)$ that depends on t is $\boldsymbol{H}_{CC}(t)$. Starting from any given initial state $|\psi(0)\rangle = |\psi^{(0)}\rangle$ we calculate $|\psi^{(m)}\rangle$ by using a generalized form of the

Cayley method

$$\left(\mathbf{1}+i\delta\tilde{\boldsymbol{H}}^{(m)}\right)\frac{\mathbf{1}+i\frac{\delta}{2}\boldsymbol{U}^{(m)}}{\mathbf{1}-i\frac{\delta}{2}\boldsymbol{U}^{(m)}}|\psi^{(m+1)}\rangle=\left(\mathbf{1}-i\delta\tilde{\boldsymbol{H}}^{(m)}\right)\frac{\mathbf{1}-i\frac{\delta}{2}\boldsymbol{U}^{(m)}}{\mathbf{1}+i\frac{\delta}{2}\boldsymbol{U}^{(m)}}|\psi^{(m)}\rangle, \tag{3.15}$$

with $\tilde{\boldsymbol{H}}^{(m)}=\frac{1}{2}[\tilde{\boldsymbol{H}}(t_{m+1})+\tilde{\boldsymbol{H}}(t_m)]$, $\boldsymbol{U}^{(m)}=\frac{1}{2}[\boldsymbol{U}(t_{m+1})+\boldsymbol{U}(t_m)]$ and $\delta=\Delta t/2$. Using the fact that $U^{(m)}$ is diagonal and nonzero only within the leads, Eq. 3.15 simplifies to

$$\left(\mathbf{1}+i\delta\tilde{\boldsymbol{H}}^{(m)}\right)\begin{bmatrix}|\psi_L^{(m+1)}\rangle/u_L^{(m)}\\|\psi_C^{(m+1)}\rangle\\|\psi_R^{(m+1)}\rangle/u_R^{(m)}\end{bmatrix}=\left(\mathbf{1}-i\delta\tilde{\boldsymbol{H}}^{(m)}\right)\begin{bmatrix}|\psi_L^{(m)}\rangle u_L^{(m)}\\|\psi_C^{(m)}\rangle\\|\psi_R^{(m)}\rangle u_R^{(m)}\end{bmatrix} \tag{3.16}$$

with

$$u_\alpha^{(m)}=\frac{1-i\frac{\delta}{2}U_\alpha^{(m)}}{1+i\frac{\delta}{2}U_\alpha^{(m)}} \tag{3.17}$$

This gives for the wavefunction in the central region

$$\begin{aligned}\left(\mathbf{1}_{CC}+i\delta\boldsymbol{H}_{CC}^{(m)}\right)|\psi_C^{(m+1)}\rangle=&\left(\mathbf{1}_{CC}-i\delta\boldsymbol{H}_{CC}^{(m)}\right)|\psi_C^{(m)}\rangle\\&-i\delta\sum_{\alpha=L,R}\boldsymbol{H}_{C\alpha}\left(\frac{|\psi_\alpha^{(m+1)}\rangle}{u_\alpha^{(m)}}+u_\alpha^{(m)}|\psi_\alpha^{(m)}\rangle\right).\end{aligned} \tag{3.18}$$

For the left and right part of the wavefunction one obtains

$$|\psi_\alpha^{(m+1)}\rangle=\frac{(\mathbf{1}_{\alpha\alpha}-i\delta\boldsymbol{H}_{\alpha\alpha}^0)}{(\mathbf{1}_{\alpha\alpha}+i\delta\boldsymbol{H}_{\alpha\alpha}^0)}\left(u_\alpha^{(m)}\right)^2|\psi_\alpha^{(m)}\rangle-i\delta\frac{1}{(\mathbf{1}_{\alpha\alpha}+i\delta\boldsymbol{H}_{\alpha\alpha}^0)}u_\alpha^{(m)}\boldsymbol{H}_{\alpha C}\left(|\psi_C^{(m+1)}\rangle+|\psi_C^{(m)}\rangle\right). \tag{3.19}$$

Plugging this identity into Eq. 3.18, we get

$$(\mathbf{1}_{CC}+i\delta\boldsymbol{H}_{\text{eff}}^{(m)})|\psi_C^{(m+1)}\rangle=(\mathbf{1}_{CC}-i\delta\boldsymbol{H}_{\text{eff}}^{(m)})|\psi_C^{(m)}\rangle-2i\delta\sum_{\alpha=L,R}u_\alpha^{(m)}\boldsymbol{H}_{C\alpha}\frac{1}{\mathbf{1}_{\alpha\alpha}+i\delta\boldsymbol{H}_{\alpha\alpha}^0}|\psi_\alpha^{(m)}\rangle. \tag{3.20}$$

Here, $\boldsymbol{H}_{\text{eff}}^{(m)}$ is the effective Hamiltonian of the central region:

$$\boldsymbol{H}_{\text{eff}}^{(m)}=\boldsymbol{H}_{CC}^{(m)}-i\delta\boldsymbol{H}_{CL}\frac{1}{\mathbf{1}_{LL}+i\delta\boldsymbol{H}_{LL}^0}\boldsymbol{H}_{LC}-i\delta\boldsymbol{H}_{CR}\frac{1}{\mathbf{1}_{RR}+i\delta\boldsymbol{H}_{RR}^0}\boldsymbol{H}_{RC} \tag{3.21}$$

with $\boldsymbol{H}_{CC}^{(m)}=\frac{1}{2}[\boldsymbol{H}_{CC}(t_{m+1})+\boldsymbol{H}_{CC}(t_m)]$. Equation 3.20 still depends on the wavefunction of the leads at each time step which require the propagation of the wavefunction in the leads. To avoid this we rewrite Eq. 3.19 recursively to end up with an equation that explicitly depends on the initial leads wavefunction only $|\psi_\alpha^0\rangle$. For $\psi_\alpha^{(m)}$ it reads

$$
\begin{aligned}
|\psi_\alpha^{(m)}\rangle =& \Lambda_\alpha^{(m-1,0)} \left(\boldsymbol{\eta}_\alpha\right)^m |\psi_\alpha^{(0)}\rangle \\
&- i\frac{\delta}{2} \sum_{k=0}^{m-1} \frac{\Lambda_\alpha^{(m-1,k)}}{u_\alpha^{(k)}} \left(\left(\boldsymbol{\eta}_\alpha\right)^{m-1-k} + \left(\boldsymbol{\eta}_\alpha\right)^{m-k} \right) \boldsymbol{H}_{\alpha C} \left(|\psi_C^{(k+1)}\rangle + |\psi_C^{(k)}\rangle \right)
\end{aligned} \tag{3.22}
$$

with

$$
\Lambda_\alpha^{(m,k)} = \prod_{j=k}^{m} \left(u_\alpha^{(j)}\right)^2 \quad \text{and} \quad \boldsymbol{\eta}_\alpha = \frac{\mathbf{1}_{\alpha\alpha} - i\delta \boldsymbol{H}_{\alpha\alpha}^0}{\mathbf{1}_{\alpha\alpha} + i\delta \boldsymbol{H}_{\alpha\alpha}^0}. \tag{3.23}
$$

Plugging Eq. 3.22 into Eq. 3.20 we arrive at the final equation for evolving the central wavefunction from time step m to time step $m+1$

$$
|\psi_C^{(m+1)}\rangle = \frac{\mathbf{1}_{CC} - i\delta \boldsymbol{H}_{\text{eff}}^{(m)}}{\mathbf{1}_{CC} + i\delta \boldsymbol{H}_{\text{eff}}^{(m)}} |\psi_C^{(m)}\rangle + |S^{(m)}\rangle + |M^{(m)}\rangle. \tag{3.24}
$$

where $|M^{(m)}\rangle$ is the memory term

$$
|M^{(m)}\rangle = -\frac{\delta^2}{\mathbf{1}_{CC} + i\delta \boldsymbol{H}_{\text{eff}}^{(m)}} \sum_{\alpha=L,R} \sum_{k=0}^{m-1} \frac{\Lambda_\alpha^{(m,k)}}{u_\alpha^{(m)} u_\alpha^{(k)}} [\boldsymbol{Q}_\alpha^{(m-k)} + \boldsymbol{Q}_\alpha^{(m-k-1)}] \left(|\psi_C^{(k+1)}\rangle + |\psi_C^{(k)}\rangle \right) \tag{3.25}
$$

with

$$
\boldsymbol{Q}_\alpha^{(m)} = \boldsymbol{H}_{C\alpha} \frac{[\boldsymbol{\eta}_\alpha]^m}{\mathbf{1}_{\alpha\alpha} + i\delta \boldsymbol{H}_{\alpha\alpha}^0} \boldsymbol{H}_{\alpha C}. \tag{3.26}
$$

The quantities $\boldsymbol{Q}_\alpha^{(m)}$ depend on the geometry of the system and are independent of the initial state $|\psi^{(0)}\rangle$ and of the applied bias. Therefore they need to be calculated only once for any given structure and can be used for different biases and initial states. The source term can be written as

$$
|S^{(m)}\rangle = -\frac{2i\delta}{\mathbf{1}_{CC} + i\delta \boldsymbol{H}_{\text{eff}}^{(m)}} \sum_{\alpha=L,R} \frac{\Lambda_\alpha^{(m,0)}}{u_\alpha^{(m)}} \boldsymbol{H}_{C\alpha} \frac{[\boldsymbol{\eta}_\alpha]^m}{\mathbf{1}_{\alpha\alpha} + i\delta \boldsymbol{H}_{\alpha\alpha}^0} |\psi_\alpha^{(0)}\rangle. \tag{3.27}
$$

For a wave packet initially localized in C the projection onto the left and right electrode $|\psi_\alpha^{(0)}\rangle$ vanishes and $|S^{(m)}\rangle = 0$ for any m, as expected.
The source term $|S^{(m)}\rangle$ describes the injection of density into the region C, while the memory term $|M^{(m)}\rangle$ is responsible for the hopping in and out of the region C.

3.1.2.1 Calculating the Memory Term

To calculate the memory term we need to calculate the memory coefficients $\boldsymbol{Q}_\alpha^{(m)}$. For leads with semiperiodic geometry along the longitudinal direction, as shown in Fig 3.2,

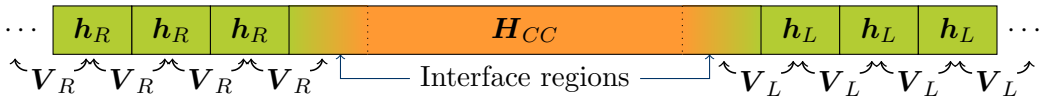

FIGURE 3.2: Sketch of an electrode-junction-electrode system with semiperiodic electrodes.

$\boldsymbol{H}^0_{\alpha\alpha}$ has a tridiagonal block form

$$\boldsymbol{H}^0_{RR} = \begin{bmatrix} \boldsymbol{h}_R & \boldsymbol{V}_R & \boldsymbol{0} & \cdots \\ \boldsymbol{V}_R & \boldsymbol{h}_R & \boldsymbol{V}_R & \cdots \\ \boldsymbol{0} & \boldsymbol{V}_R & \boldsymbol{h}_R & \cdots \\ \vdots & \vdots & \vdots & \ddots \end{bmatrix}, \qquad \boldsymbol{H}^0_{LL} = \begin{bmatrix} \ddots & \vdots & \vdots & \vdots \\ \boldsymbol{V}_L & \boldsymbol{h}_L & \boldsymbol{V}_L & \boldsymbol{0} \\ \boldsymbol{0} & \boldsymbol{V}_L & \boldsymbol{h}_L & \boldsymbol{V}_L \\ \boldsymbol{0} & \boldsymbol{0} & \boldsymbol{V}_L & \boldsymbol{h}_L \end{bmatrix} \tag{3.28}$$

where $\boldsymbol{h}_\alpha$ describes a convenient cell of lead α and $\boldsymbol{V}_\alpha$ is the hopping Hamiltonian between two nearest neighbor cells. Without loss of generality we assume that both $\boldsymbol{h}_\alpha$ and $\boldsymbol{V}_\alpha$ are square matrices of dimension $N_\alpha \times N_\alpha$ where N_α is the number of grid points of one cell. The memory coefficients are matrices of the form given in Eq. 3.26.

Since the coupling matrices $\boldsymbol{H}_{C\alpha} = \boldsymbol{H}^T_{\alpha C}$ are sparse

$$\boldsymbol{H}_{CR} = \boldsymbol{H}^T_{RC} = \begin{bmatrix} \boldsymbol{0} & \boldsymbol{0} & \boldsymbol{0} & \cdots \\ \vdots & \vdots & \vdots & \cdots \\ \boldsymbol{0} & \boldsymbol{0} & \boldsymbol{0} & \cdots \\ \boldsymbol{v}_R & \boldsymbol{0} & \boldsymbol{0} & \ddots \end{bmatrix}, \qquad \boldsymbol{H}_{CL} = \boldsymbol{H}^T_{LC} = \begin{bmatrix} \ddots & \boldsymbol{0} & \boldsymbol{0} & \boldsymbol{v}_L \\ \cdots & \boldsymbol{0} & \boldsymbol{0} & \boldsymbol{0} \\ \cdots & \vdots & \vdots & \vdots \\ \cdots & \boldsymbol{0} & \boldsymbol{0} & \boldsymbol{0} \end{bmatrix} \tag{3.29}$$

the memory coefficients $\boldsymbol{Q}^{(m)}_\alpha$ are sparse matrices with non vanishing entries only at the boundary

$$\boldsymbol{Q}^{(m)}_L = \begin{bmatrix} \boldsymbol{q}^{(m)}_L & \boldsymbol{0} & \boldsymbol{0} \\ \boldsymbol{0} & \boldsymbol{0} & \boldsymbol{0} \\ \boldsymbol{0} & \boldsymbol{0} & \boldsymbol{0} \end{bmatrix}, \qquad \boldsymbol{Q}^{(m)}_R = \begin{bmatrix} \boldsymbol{0} & \boldsymbol{0} & \boldsymbol{0} \\ \boldsymbol{0} & \boldsymbol{0} & \boldsymbol{0} \\ \boldsymbol{0} & \boldsymbol{0} & \boldsymbol{q}^{(m)}_R \end{bmatrix}. \tag{3.30}$$

Note that the hopping between two nearest neighbor cells in the lead α, denoted as $\boldsymbol{V}_\alpha$, in general can be different from hopping $\boldsymbol{v}_\alpha$ between lead α and central region. However, we assume that the central region contains the first few atomic layers of the leads and hence the $\boldsymbol{v}_\alpha = \boldsymbol{V}_\alpha$. In the next chapters when we use different hopping $\boldsymbol{v}_\alpha$ and $\boldsymbol{V}_\alpha$, to avoid recalculating the memory terms, practically we choose a central region large

enough such that the hopping at the interface of the enlarged central region to the lead is equal to the one inside the lead. The $\boldsymbol{q}_\alpha^{(m)}$'s are square matrices of dimension $N_\alpha \times N_\alpha$ and are given by

$$\boldsymbol{q}_\alpha^{(m)} = \boldsymbol{V}_\alpha \left[\frac{[\boldsymbol{\eta}_\alpha]^m}{\mathbf{1}_{\alpha\alpha} + i\delta \boldsymbol{H}_{\alpha\alpha}} \right]_{1,1} \boldsymbol{V}_\alpha, \tag{3.31}$$

where the subscript $(1,1)$ denotes the first diagonal block of the matrix in the square brackets. We introduce the generating matrix function

$$\boldsymbol{q}_\alpha(x,y) \equiv \boldsymbol{V}_\alpha \left[\frac{1}{x\mathbf{1}_{\alpha\alpha} + iy\delta \boldsymbol{H}_{\alpha\alpha}} \right]_{1,1} \boldsymbol{V}_\alpha, \tag{3.32}$$

It is easy to see that the $\boldsymbol{q}_\alpha^{(m)}$ can be obtained from

$$\boldsymbol{q}_\alpha^{(m)} = \frac{[D(x,y)]^m}{m!}\, \boldsymbol{q}_\alpha(x,y)|_{x=y=1} \tag{3.33}$$

with

$$D(x,y) = \left[-\frac{\partial}{\partial x} + \frac{\partial}{\partial y} \right]. \tag{3.34}$$

Now we need to calculate the first diagonal block of the inverse of the matrix $x\mathbf{1}_{\alpha\alpha} + iy\delta \boldsymbol{H}_{\alpha\alpha}$, which turns out to have a closed form due to the tridiagonal nature of $\boldsymbol{H}_{\alpha\alpha}$. Hence the generating matrix $\boldsymbol{q}_\alpha(x,y)$ can also be expressed in terms of continued matrix fractions

$$\begin{aligned} \boldsymbol{q}_\alpha(x,y) &= \boldsymbol{V}_\alpha \cfrac{1}{x + iy\delta \boldsymbol{h}_\alpha + y^2\delta^2 \boldsymbol{V}_\alpha \cfrac{1}{x + iy\delta \boldsymbol{h}_\alpha + y^2\delta^2 \boldsymbol{V}_\alpha \cfrac{1}{\ddots}\, \boldsymbol{V}_\alpha}\, \boldsymbol{V}_\alpha} \boldsymbol{V}_\alpha \\ &= \boldsymbol{V}_\alpha \frac{1}{x + iy\delta \boldsymbol{h}_\alpha + y^2\delta^2 \boldsymbol{q}_\alpha(x,y)} \boldsymbol{V}_\alpha. \end{aligned} \tag{3.35}$$

From Eq. 3.33 and Eq. 3.35 one can build up a recursive scheme. As $\boldsymbol{V}_\alpha$ are not invertible in general we define a new matrix where $\boldsymbol{q}_\alpha^{(m)} = \boldsymbol{V}_\alpha \boldsymbol{p}_\alpha^{(m)} \boldsymbol{V}_\alpha$ and

$$\boldsymbol{p}_\alpha^{-1}(x,y) = x + iy\delta \boldsymbol{h}_\alpha + y^2\delta^2 \boldsymbol{q}_\alpha(x,y) \tag{3.36}$$

Similar to Eq. 3.33 for $\boldsymbol{p}_\alpha^{(m)}$ we have

$$\boldsymbol{p}_\alpha^{(m)} = \frac{[D(x,y)]^m}{m!} \boldsymbol{p}_\alpha(x,y)|_{x=y=1} \tag{3.37}$$

Using the identity $\boldsymbol{p}_\alpha(x,y)\boldsymbol{p}_\alpha^{-1}(x,y) = \mathbf{1}$

$$\frac{[D(x,y)]^m}{m!} \boldsymbol{p}_\alpha(x,y)\boldsymbol{p}_\alpha^{-1}(x,y) = \mathbf{0} \tag{3.38}$$

and with the expression $D^m fg = \sum_{j=0}^{m} \binom{m}{j} D^{m-j} f D^j g$ one finds

$$(1 + i\delta \boldsymbol{h}_\alpha)\boldsymbol{p}_\alpha^{(m)} = (1 - i\delta \boldsymbol{h}_\alpha)\boldsymbol{p}_\alpha^{(m-1)} - \delta^2 \sum_{k=0}^{m} (\boldsymbol{q}_\alpha^{(k)} + 2\boldsymbol{q}_\alpha^{(k-1)} + \boldsymbol{q}_\alpha^{(k-2)})\boldsymbol{p}_\alpha^{(m-k)} \tag{3.39}$$

with $\boldsymbol{p}_\alpha^{(m)} = \boldsymbol{q}_\alpha^{(m)} = 0$ for $m < 0$.

Having this equation in hand, the memory coefficients can be calculated recursively: once $\boldsymbol{q}_\alpha^{(0)}$ has been obtained by solving Eq. 3.35 with $x = y = 1$, we can calculate $\boldsymbol{p}_\alpha^{(0)} = [1 + i\delta \boldsymbol{h}_\alpha + \delta^2 \boldsymbol{q}_\alpha^{(0)}]^{-1}$. Afterwards, we can use Eq. 3.39 with $\boldsymbol{q}_\alpha^{(1)} = \boldsymbol{V}_\alpha \boldsymbol{p}_\alpha^{(1)} \boldsymbol{V}_\alpha$ to calculate $\boldsymbol{p}_\alpha^{(1)}$ and hence $\boldsymbol{q}_\alpha^{(1)}$ and so on. An important feature of the memory coefficients is that they only depend on δ, $\boldsymbol{H}_{\alpha\alpha}^0$, $H_{C\alpha}$. Therefore, once they are calculated for a certain geometry of the lead and time step and $H_{C\alpha}$, they can be used for any time-dependent bias or central region.

3.1.2.2 Calculating the Source Term

The source term is given by

$$|S^{(m)}\rangle = -\frac{2i\delta}{\mathbf{1}_{CC} + i\delta \boldsymbol{H}_{\text{eff}}^{(m)}} \sum_{\alpha=L,R} \frac{\Lambda_\alpha^{(m,0)}}{u_\alpha^{(m)}} \boldsymbol{H}_{C\alpha} \frac{[\boldsymbol{\eta}_\alpha]^m}{\mathbf{1}_{\alpha\alpha} + i\delta \boldsymbol{H}_{\alpha\alpha}^0} |\psi_\alpha^{(0)}\rangle. \tag{3.40}$$

For simplification we define:

$$R_\alpha^{(m)} =: \boldsymbol{H}_{C\alpha} \frac{(\boldsymbol{\eta}_\alpha)^m}{\mathbf{1}_{\alpha\alpha} + i\delta \boldsymbol{H}_{\alpha\alpha}^0} |\psi_\alpha^{(0)}\rangle \tag{3.41}$$

Using the static Schrödinger equation:

$$\begin{pmatrix} \boldsymbol{H}_{LL}^0 & \boldsymbol{H}_{LC} & \mathbf{0} \\ \boldsymbol{H}_{CL} & \boldsymbol{H}_{CC}^0 & \boldsymbol{H}_{CR} \\ \mathbf{0} & \boldsymbol{H}_{RC} & \boldsymbol{H}_{RR}^0 \end{pmatrix} \begin{pmatrix} |\psi_L^{(0)}\rangle \\ |\psi_C^{(0)}\rangle \\ |\psi_R^{(0)}\rangle \end{pmatrix} = E \begin{pmatrix} |\psi_L^{(0)}\rangle \\ |\psi_C^{(0)}\rangle \\ |\psi_R^{(0)}\rangle \end{pmatrix} \tag{3.42}$$

one can immediately see that

$$\boldsymbol{H}_{\alpha\alpha}^0 |\psi_\alpha^{(0)}\rangle = E|\psi_\alpha^{(0)}\rangle - \boldsymbol{H}_{\alpha C}|\psi_C^{(0)}\rangle \tag{3.43}$$

with $\alpha = L, R$. Again we define a generating function

$$R_\alpha(x, y) = \boldsymbol{H}_{C\alpha} \frac{1}{x\mathbf{1}_{\alpha\alpha} + iy\delta \boldsymbol{H}_{\alpha\alpha}^0} |\psi_\alpha^{(0)}\rangle \tag{3.44}$$

which allows us to write the coefficient of Eq. (3.41) for the m^{th} time step as

$$R_\alpha^{(m)} = \frac{[D(x,y)]^m}{m!} R_\alpha(x,y)\Big|_{x=y=1}. \tag{3.45}$$

From Eq. (3.43) we calculate

$$(x\mathbf{1}_{\alpha\alpha} + iy\delta \boldsymbol{H}^0_{\alpha\alpha})|\psi_\alpha^{(0)}\rangle = (x + iy\delta E)|\psi_\alpha^{(0)}\rangle - iy\delta \boldsymbol{H}_{\alpha C}|\psi_C^{(0)}\rangle. \tag{3.46}$$

The prefactor on the right hand side acts on $|\psi_\alpha^{(0)}\rangle$ and gives a scalar, hence:

$$|\psi_\alpha^{(0)}\rangle = \frac{1}{x + iy\delta E}\left[(x\mathbf{1}_{\alpha\alpha} + iy\delta \boldsymbol{H}^0_{\alpha\alpha})|\psi_\alpha^{(0)}\rangle + iy\delta \boldsymbol{H}_{\alpha C}|\psi_C^{(0)}\rangle\right]. \tag{3.47}$$

Putting this back into Eq. (3.44) and using the definition of $\boldsymbol{Q}(x,y)$ we find

$$R_\alpha(x,y) = \frac{1}{x + iy\delta E}\left[\boldsymbol{H}_{C\alpha}|\psi_\alpha^{(0)}\rangle + iy\delta \boldsymbol{Q}_\alpha(x,y)|\psi_C^{(0)}\rangle\right]. \tag{3.48}$$

Therefore, with Eq. (3.45) for the m^{th} time step, we arrive at

$$R_\alpha^{(m)} = f^{(m)}\boldsymbol{H}_{C\alpha}|\psi_\alpha^{(0)}\rangle + i\delta\sum_{k=0}^{m}(f^{(m-k)} + f^{(m-k-1)})\boldsymbol{Q}_\alpha^{(k)}|\psi_C^{(0)}\rangle \tag{3.49}$$

with

$$f^{(n)} = \frac{(1 - i\delta E)^n}{(1 + i\delta E)^{n+1}}. \tag{3.50}$$

Decomposing the source term as:

$$|S^{(m)}\rangle = \frac{1}{\mathbf{1}_{CC} + i\delta \boldsymbol{H}_{\text{eff}}^{(m)}}\sum_{\alpha=L,R}|S_\alpha^{(m)}\rangle, \tag{3.51}$$

The left and right parts $|S_\alpha^{(m)}\rangle$ then read

$$|S_\alpha^{(m)}\rangle = -2i\delta\frac{\Lambda_\alpha^{(m,0)}}{u_\alpha^{(m)}}\left(f^{(m)}\boldsymbol{H}_{C\alpha}|\psi_\alpha^{(0)}\rangle + i\delta\sum_{k=0}^{m}(f^{(m-k)} + f^{(m-k-1)})\boldsymbol{Q}_\alpha^{(k)}|\psi_C^{(0)}\rangle\right). \tag{3.52}$$

Since the computational effort of the source term $S^{(m)}$ (Eq. (3.52)) is of order of $O(m^2)$ it is preferable in practice to use a recursive scheme.

The recursive relations of $\Lambda^{(n,0)}$ and $f^{(n)}$ are given by

$$\Lambda_\alpha^{(n,0)} = \left(u_\alpha^{(n)}\right)^2 \Lambda_\alpha^{(n-1,0)} \tag{3.53}$$

$$\Lambda_\alpha^{(0,0)} = (u_\alpha^{(0)})^2 \tag{3.54}$$

$$f^{(n)} = \frac{1-i\delta E}{1+i\delta E} f^{(n-1)} = g f^{(n-1)} \quad \text{with } g = \frac{1-i\delta E}{1+i\delta E} \tag{3.55}$$

$$f^{(0)} = \frac{1}{1+i\delta E} \tag{3.56}$$

$$f^{(n)} = 0 \quad if \quad n < 0 \tag{3.57}$$

Now we rewrite equation (3.52) using the recursive relations of (3.53) - (3.57), beginning with $f^{(n)}$ and extracting the last term of the sum:

$$\begin{aligned} |S_\alpha^{(m)}\rangle = &-2i\delta \frac{\Lambda_\alpha^{(m,0)}}{u_\alpha^{(m)}} g \left(f^{(m-1)} \boldsymbol{H}_{C\alpha} |\psi_\alpha^{(0)}\rangle + i\delta \sum_{k=0}^{m-1} (f^{(m-1-k)} + f^{(m-2-k)}) \boldsymbol{Q}_\alpha^{(k)} |\psi_C^{(0)}\rangle \right) \\ &+ 2 \frac{\Lambda_\alpha^{(m,0)}}{u_\alpha^{(m)}} \delta^2 f^{(0)} \left(\boldsymbol{Q}_\alpha^{(m)} + \boldsymbol{Q}_\alpha^{(m-1)} \right) |\psi_C^{(0)}\rangle \end{aligned} \tag{3.58}$$

In the next step we substitute $\Lambda_\alpha^{(m,0)}$

$$\begin{aligned} |S_\alpha^{(m)}\rangle = &2 \frac{\Lambda_\alpha^{(m,0)}}{u_\alpha^{(m)}} \delta^2 f^{(0)} \left(\boldsymbol{Q}_\alpha^{(m)} + \boldsymbol{Q}_\alpha^{(m-1)} \right) |\psi_C^{(0)}\rangle + g u_\alpha^{(m)} u_\alpha^{(m-1)} \times \\ &\underbrace{\left[-2i\delta \frac{\Lambda_\alpha^{(m-1,0)}}{u_\alpha^{(m-1)}} \left(f^{(m-1)} \boldsymbol{H}_{C\alpha} |\psi_\alpha^{(0)}\rangle + i\delta \sum_{k=0}^{(m-1)} (f^{(m-1-k)} + f^{(m-2-k)}) \boldsymbol{Q}_\alpha^{(k)} |\psi_C^{(0)}\rangle \right) \right]}_{|S_\alpha^{(m-1)}\rangle} \end{aligned} \tag{3.59}$$

to find the recursive relations

$$|S_\alpha^{(0)}\rangle = -\frac{2i\delta}{1+i\delta E} u_\alpha^{(0)} \left(\mathbf{H}_{C\alpha} |\psi^{(0)}\alpha\rangle + i\delta \boldsymbol{Q}_\alpha^{(0)} |\psi_C^{(0)}\rangle \right) \tag{3.60}$$

$$|S_\alpha^{(m)}\rangle = \frac{1}{1+i\delta E} \left[(1-i\delta E)\, u_\alpha^{(m)} u_\alpha^{(m-1)} |S_\alpha^{(m-1)}\rangle + 2\delta^2 \frac{\Lambda_\alpha^{(m,0)}}{u_\alpha^{(m)}} \left(\boldsymbol{Q}_\alpha^{(m)} + \boldsymbol{Q}_\alpha^{(m-1)} \right) |\psi_C^{(0)}\rangle \right]. \tag{3.61}$$

Therefore this part of the algorithm can be rewritten to scale like $O(m)$ with the time step m.

It is worth emphasizing again that the algorithm described above for the propagation of the time-dependent Schrödinger equation for extended systems can be used for the

propagation of a time-dependent Kohn-Sham equation. However, in this case a complication arises due to the fact that in order to compute $|\psi_C^{(m+1)}\rangle$ at time step $m+1$, the time-dependent KS potential at the same time step is needed which depends on the still unknown time-dependent density at time step $m+1$ via the Hartree and exchange-correlation potentials. The solution is to use a two-step predictor-corrector approach [33]:

In the predictor step we approximate $\boldsymbol{H}_{CC}^{(m)}$ by $\boldsymbol{H}_{CC}(t_m)$ and compute new orbitals $|\psi'^{(m+1)}_C\rangle$. Then the corresponding Hartree and exchange-correlation potentials are constructed, leading to the Hamiltonian $\boldsymbol{H}'_{CC}(t_m+1)$.

In the corrector step we use the average

$$\boldsymbol{H}_{CC}^{(m)} = \frac{\boldsymbol{H}'_{CC}(t_m+1) + \boldsymbol{H}_{CC}(t_m)}{2} \tag{3.62}$$

as an approximation to $\boldsymbol{H}_{CC}^{(m)}$. The numerical effort introduced by this predictor-corrector scheme is doubled compared to the ordinary propagation.

Chapter 4

The Role of Bound States in Time-Dependent Quantum Transport

As already mentioned in the previous chapters, the standard approach to describe quantum theory of transport is the Landauer-Büttiker formalism [34, 35], which expresses the conductance of a device in terms of the quantum-mechanical transmittance of *non-interacting* electrons at the Fermi energy. To account for interaction, the Landauer-Büttiker formalism has been combined with (static) DFT which allows to take into account the atomistic structure of both the molecule and the contacts [17–25]. (For a critical review of this methodology see Ref. [26].)

The Landauer-Büttiker-based approaches focus on the description of steady-state transport and assume that for a system driven out of equilibrium by a dc bias, the current will eventually reach a steady state. It means that in these approaches the dynamical formation of the steady state is not proved but rather taken for granted.
As an alternative approach in which many-body effects can be incorporated properly, NEGF approach provides a natural framework to study quantum transport properties of nanoscale devices coupled to leads. In model systems the leads are assumed to be non-interacting and the current is computed from the Meir-Wingreen formula [36] using approximate many-body self-energies Σ_{MB}. For weakly correlated models $\Sigma_{\mathrm{MB}} \sim 0$ and the Meir-Wingreen formula reduces to the Landauer-Büttiker formula [34, 35] (see next chapter), as it should.

If one wants to account for the full atomistic structure of the system, the NEGF formalism is usually combined with static DFT and the current is computed from a Landauer-type equation [17–25]. This approach enjoys increasing popularity, in particular for the description of transport experiments on single molecules [37]. From a fundamental point of view, however, the use of static DFT - which is an equilibrium theory - is not justified to describe non-equilibrium situations.

By construction, the NEGF+DFT approach inherits the steady-state assumption of the Landauer formalism. In other words also in this approach, the dynamical formation of a steady state does not follow from the formalism but rather constitutes an assumption. The question how the system dynamically reaches a steady state has been investigated both numerically [30, 38–40] and theoretically [29, 41]. Using NEGF techniques (for non-interacting electrons) it has been shown [29] that the total current (and density) approaches a steady value provided the local density of states is smooth in the device region. This steady value is 1) in agreement with the Landauer formula and 2) independent of the initial equilibrium configuration and the history of the applied bias.

The situation is different, however, if there exist two or more localized bound states in the device region, i.e., if the local density of states has sharp peaks at certain energies. The inclusion of bound states in time-dependent quantum transport has been studied in Ref. [42] and further been addressed in subsequent work [43]. There it is demonstrated that if the dc biased Hamiltonian supports two or more bound states, the long-time limit of the current(and its corresponding density) consists of two terms: a steady-state contribution given by the Landauer formula and an additional, dynamical contribution responsible for undamped current(density) oscillations. The frequencies of these oscillations are given by the differences between the bound-states energies and, interestingly, the amplitudes *depend on both the initial state and history of the time-dependent perturbation.*

In this chapter, the history as well as the initial-state dependence of the dynamical part of the current and density is investigated numerically in detail and the bound-state contribution to the *time-averaged* density is shown to be history-dependent as well which leads to a natural definition of the bound-state occupations out of equilibrium. As a tool for our numerical calculations the algorithm explained in Chapter 3 for the

time propagation of quantum transport systems according to the Schrödinger equation is used.

4.1 Proper Inclusion of Bound States in Time-dependent Quantum Transport

Let $\boldsymbol{H}^0$ be the one-particle Hamiltonian of the system in equilibrium. At positive times the system is perturbed with a bias. Let's assume that the one-particle Hamiltonian $\boldsymbol{H}(t)$ *globally* converges to a *time-independent* Hamiltonian $\boldsymbol{H}^\infty$ when $t \to \infty$ and supports at least two bound states. As explained in Chapter 3, we further assume that for any point $\boldsymbol{r}$ in electrode α the quantity $\langle \boldsymbol{r}|\boldsymbol{H}(t) - \boldsymbol{H}^0|\boldsymbol{r}\rangle = W_\alpha(t)$ is a spatially uniform time-dependent shift. To illustrate the bound states effect, let's look at the one-particle density matrix $\rho(\boldsymbol{r}, \boldsymbol{r}'; t)$ in the long-time limit

$$\rho(\boldsymbol{r}, \boldsymbol{r}'; t \to \infty) = \lim_{t\to\infty} \mathrm{Im}\langle \boldsymbol{r}|\mathbf{G}^<(t;t)|\boldsymbol{r}'\rangle, \tag{4.1}$$

The lesser Green function can be expressed [28, 29, 41, 44, 45] in terms of retarded and advanced Green functions as

$$\mathbf{G}^<(t;t') = \mathbf{G}^R(t;0)\mathbf{G}^<(0;0)\mathbf{G}^A(0;t') \tag{4.2}$$

with the initial condition $\mathbf{G}^<(0;0) = if(\boldsymbol{H}^0)$ where $f(\omega) = (e^{\beta(\omega-\mu)}+1)^{-1}$ is the Fermi distribution function. Writing the retarded and advanced Green function in terms of evolution operator

$$\mathbf{G}^R(t,t') = -i\theta(t-t')T[e^{-i\int_t^{t'} \mathrm{d}\tau\, \boldsymbol{H}(\tau)}] = [\mathbf{G}^A(t',t)]^\dagger, \tag{4.3}$$

with T being the time-ordering operator, the one-particle density matrix $\rho(\boldsymbol{r}, \boldsymbol{r}'; t)$ in the long-time limit can be written as

$$\rho(\boldsymbol{r}, \boldsymbol{r}'; t \to \infty) = \langle \boldsymbol{r}|e^{-i\boldsymbol{H}^\infty t}\boldsymbol{M}^\dagger f(\boldsymbol{H}^0)\boldsymbol{M}e^{i\boldsymbol{H}^\infty t}|\boldsymbol{r}'\rangle. \tag{4.4}$$

In Eq. (4.4), $\boldsymbol{M}^\dagger$ is a unitary operator defined as

$$\boldsymbol{M}^\dagger = \lim_{t\to\infty} e^{i\boldsymbol{H}^\infty t}\, T[e^{-i\int_0^t \mathrm{d}\tau\, \boldsymbol{H}(\tau)}], \tag{4.5}$$

that depends on the history of the time-dependent perturbation and we will call it "memory operator" from now on.

Let $|\psi_b^\infty\rangle$ be the bound eigenstates of $\boldsymbol{H}^\infty$ with eigenenergies ϵ_b^∞ and $|\psi_k^\infty\rangle$ the continuum eigenstates of $\boldsymbol{H}^\infty$ with eigenenergies ϵ_k^∞. Inserting twice the completeness relation $1 = \sum_b |\psi_b^\infty\rangle\langle\psi_b^\infty| + \sum_k |\psi_k^\infty\rangle\langle\psi_k^\infty|$ one can rewrite Eq. (4.4) as

$$\begin{aligned} \rho(\boldsymbol{r},\boldsymbol{r}';t\to\infty) &= \sum_{b,b'} \psi_b^\infty(\boldsymbol{r}) f_{b,b'} \psi^{*\infty}_{b'}(\boldsymbol{r}') e^{-i(\epsilon_b^\infty - \epsilon_{b'}^\infty)t} \\ &+ \sum_k \psi_k^\infty(\boldsymbol{r}) f_{k,k} \psi^{*\infty}_k(\boldsymbol{r}'), \end{aligned} \tag{4.6}$$

with

$$f_{b,b'} = \langle\psi_b^\infty|\boldsymbol{M}^\dagger f(\boldsymbol{H}^0)\boldsymbol{M}|\psi_{b'}^\infty\rangle \tag{4.7}$$

and $f_{k,k} = \langle\psi_k^\infty|\boldsymbol{M}^\dagger f(\boldsymbol{H}^0)\boldsymbol{M}|\psi_k^\infty\rangle$.

To cancel the bound-continuum contributions and the off-diagonal terms of the continuum-continuum contribution [43] in Eq. 4.6 , the Riemann-Lebesgue theorem has been used. The coefficients $f_{b,b'}$ are matrix elements of $f(\boldsymbol{H}^0)$ between history-dependent localized functions

$$f_{b,b'} = \langle\psi_b'|f(\boldsymbol{H}^0)|\psi_{b'}'\rangle \ , \tag{4.8}$$

which depend on the history of the applied perturbation as well as the initial condition. Clearly, the state $|\psi_b'\rangle$ is related to $|\psi_b^\infty\rangle$ by a unitary transformation $\boldsymbol{M}$

$$\begin{bmatrix} |\psi'_{bL}\rangle \\ |\psi'_{bC}\rangle \\ |\psi'_{bR}\rangle \end{bmatrix} = \begin{bmatrix} e^{i\Delta_L^\infty}\mathbf{1}_L & 0 & 0 \\ 0 & \boldsymbol{M}_C & 0 \\ 0 & 0 & e^{i\Delta_R^\infty}\mathbf{1}_R \end{bmatrix} \begin{bmatrix} |\psi^\infty_{bL}\rangle \\ |\psi^\infty_{bC}\rangle \\ |\psi^\infty_{bR}\rangle \end{bmatrix}, \tag{4.9}$$

with

$$\Delta_\alpha^\infty = \lim_{t\to\infty} \int_0^t \mathrm{d}t' (W_\alpha(t') - W_\alpha^\infty), \tag{4.10}$$

and $\boldsymbol{M}_C$ a unitary "memory matrix" with the same dimension as the number of degrees of freedom employed to describe region C and $\mathbf{1}_\alpha$ the identity matrix projected onto region $\alpha = L, R$. The memory matrix depends on the history of the time-dependent perturbation and is defined through the equation below

$$\lim_{t\to\infty} \mathbf{G}^A_{CC}(0;t) = \boldsymbol{M}_C \lim_{t\to\infty} \bar{\mathbf{G}}^A_{CC}(0;t), \tag{4.11}$$

where $\bar{\mathbf{G}}^A_{CC}(0;t)$ is the projection onto region C of the advanced Green function $\bar{\mathbf{G}}^A(0;t) = i\exp(i\boldsymbol{H}^\infty t)$.

From Eq. (4.6) it is clear that the density matrix in the long time limit has in principle two contribution: a steady contribution $\rho^{(S)}$ (the second term of Eq. (4.6)) and an additional dynamical contribution, $\rho^{(D)}$, responsible for persistent oscillations with a history dependent amplitude. Obviously, the dynamical contribution is only present if the final Hamiltonian posses at least two bound states. It is worth noting that the "memory operator", $\boldsymbol{M}$, appears in the dynamical as well as the steady contribution of the density matrix through the coefficients $f_{k,k}$ and $f_{b,b'}$. In the steady part, however, the history dependence cancels out [43] . The steady contribution to the density matrix in region C is shown to be:

$$\rho^{(S)}_C = 2\int \frac{d\omega}{2\pi} \sum_{\alpha=L,R} f(\omega - W^\infty_\alpha)\boldsymbol{G}^R_{CC}(\omega)\Gamma_\alpha(\omega)\boldsymbol{G}^A_{CC}(\omega). \tag{4.12}$$

As current and density are connected through the continuity equation, clearly bound-state oscillations not only appear in the density but also in the current. As a consequence, the current has a steady-state and a dynamical contribution

$$\lim_{t\to\infty} I_\alpha(t) = I^{(S)}_\alpha + I^{(D)}_\alpha(t)\ , \tag{4.13}$$

where the steady contribution $I^{(S)}_\alpha$ is given by a Landauer type formula [28]

$$I^{(S)}_\alpha = 2e\int \frac{d\omega}{2\pi}[f(\omega - W^\infty_L) - f(\omega - W^\infty_R)]T(\omega). \tag{4.14}$$

In the above equation $T(\omega)$ is the so called transmission probability

$$T(\omega) = \mathrm{Tr}[\mathbf{G}^R_{CC}(\omega)\mathbf{\Gamma}_L(\omega)\mathbf{G}^A_{CC}(\omega)\mathbf{\Gamma}_R(\omega)], \tag{4.15}$$

where $\mathbf{\Gamma}_\alpha(\omega) = -2\mathrm{Im}[\mathbf{\Sigma}^R_\alpha(\omega)]$ and $\mathbf{\Sigma}^R_\alpha(\omega) = \boldsymbol{H}_{C\alpha}\boldsymbol{g}^R_{\alpha\alpha}(\omega)\boldsymbol{H}_{\alpha C}$ is the embedding self-energy with the retarded Green function of lead α, $\boldsymbol{g}^R_{\alpha\alpha}(\omega) = \left(\omega - \boldsymbol{H}^0_{\alpha\alpha} - W^\infty_\alpha + i0^+\right)^{-1}$. In the absence of bound states, a steady current develops which does not depend on the initial Hamiltonian (i.e. the memory of different initial conditions is completely washed out) and does also not depend on the history of the applied bias (memory-loss theorem) [29].

In the presence of bound states, however, in addition to the steady-state contribution $I_\alpha^{(S)}$ given by Eq. (4.14), there exists an explicitly time-dependent contribution $I_\alpha^{(D)}$ which can be calculated from

$$\begin{aligned} I_\alpha^{(D)}(t) &= -e\frac{d}{dt}N_\alpha(t) \\ &= e\ \mathrm{Tr}_\alpha \sum_{b,b'}(\epsilon_b^\infty - \epsilon_{b'}^\infty)|\psi_{b\alpha}^\infty\rangle\langle\psi_{b'\alpha}^\infty| f_{b,b'}\sin[(\epsilon_b^\infty - \epsilon_{b'}^\infty)t] \\ &= 2e\ \sum_{b,b'}\Lambda_{b,b'}^\alpha f_{b,b'}\sin[(\epsilon_b^\infty - \epsilon_{b'}^\infty)t], \end{aligned} \tag{4.16}$$

where we have defined

$$\Lambda_{b,b'}^\alpha = \frac{(\epsilon_b^\infty - \epsilon_{b'}^\infty)}{2}\mathrm{Tr}_\alpha\left[|\psi_{b\alpha}^\infty\rangle\langle\psi_{b'\alpha}^\infty|\right]. \tag{4.17}$$

Using the relation $|\psi_{b\alpha}^\infty\rangle = \frac{1}{\epsilon_b^\infty \mathbf{1}_\alpha - \boldsymbol{H}_{\alpha\alpha}^\infty}\boldsymbol{H}_{\alpha C}|\psi_{bC}^\infty\rangle$ Eq. (4.17) can be rewritten as

$$\Lambda_{b,b'}^\alpha = \frac{1}{2}\mathrm{Tr}_C\left[|\psi_{bC}^\infty\rangle\langle\psi_{b'C}^\infty|(\boldsymbol{\Sigma}_\alpha^A(\epsilon_{b'}^\infty) - \boldsymbol{\Sigma}_\alpha^A(\epsilon_b^\infty)\right]. \tag{4.18}$$

A few remarks about the central result in Eq. (4.13) are in order:

i) It should be emphasized again that *no steady-state current* exists if the biased Hamiltonian $\boldsymbol{H}^\infty$ has bound eigenstates. The current and density oscillations given by Eq. (4.16) and the first term of Eq. (4.4) are persistent, i.e., they do not decay in time.

ii) The amplitude of the current oscillations may be very large compared to the steady component of the current.

iii) In contrast to the case without bound states, the asymptotic current depends both on the initial equilibrium configuration and the history of the applied bias and gate voltage through the coefficients $f_{b,b'}$ of Eq. (4.8). The memory dependence of the current oscillations will be explicitly demonstrated.

iv) For *sudden switching* of the bias and (simultaneously applying) the gate voltage $\Delta_\alpha^\infty = 0$ and $\boldsymbol{M}_C = \mathbf{1}_C$ ($\mathbf{1}_C$ being the identity matrix projected onto region C) and the matrix in Eq. (4.9) reduces to the identity matrix, while other switching processes yield different memory matrices and hence different amplitudes of the current and density oscillations, see Section (4.2) for a detailed study of the history dependence.

v) Our time-dependent approach provides a natural way to properly define the occupation numbers of bound states with energies in the bias window. It should be remembered that within the standard NEGF+DFT approach, the question of how to take bound

states into account in the calculation of the density [22, 46] has, so far, remained an unsolved problem. Here we show how the bound-state occupations naturally *result from the time evolution* of the system.

In the static approaches to transport, bound states are usually treated in an ad-hoc way, namely they are considered entirely populated below the bias window, while bound states within the bias window are populated in a somewhat artificial way by hand with some plausible choice for the occupation numbers [47]. The importance of properly treating the bound-states has been also pointed out by Dhar and Sen [42], where they reported that in the presence of bound states the density and current oscillate persistently *even for the unbiased* system. This feature originates from the basic assumption of the contacting approach where the central part of the system is not connected to the leads $V_{\alpha c} = 0$ initially (for $t < 0$) , $\boldsymbol{H}_0$ is a block-diagonal matrix and so is $f(\boldsymbol{H}_0)$. The contact between the isolated parts is turned on as a time-dependent perturbation. Through out the whole thesis we use the later approach. In this case, the initial equilibrium is unambiguous and for the unbiased system, the equilibrium Hamiltonian and the one at the long time limit are identical and therefore $f_{b,b'} = \delta_{b,b'} f(\epsilon_b)$. As a result the dynamical contribution to the total current vanishes, while the dynamical contribution to the density reduces to the equilibrium contribution of the bound states.

vi) We demonstrate the intuitively expected result that the bound-state occupations are history-dependent, i.e., they depend on the initial condition and on how the potential is switched on.

vii) As expected the number of particles in the whole system is conserved. Using Eq. (4.17) and Eq. (4.16) and employing the orthonormality relation

$$\sum_{\alpha=L,C,R} \mathrm{Tr}_\alpha \left[|\psi^\infty_{b\alpha}\rangle\langle\psi^\infty_{b'\alpha}| \right] = \delta_{b,b'}. \tag{4.19}$$

It can be shown easily that

$$e\frac{d}{dt}N_C(t) = (I_L(t) + I_R(t)). \tag{4.20}$$

In next the section, we provide numerical evidence that bound states give rise to persistent, non-decaying current oscillations in the junction. We also show that the amplitude of these oscillations can exhibit a strong dependence on the history of the applied potential as well as on the initial equilibrium configuration. Our simulations allow for a quantitative investigation of several transient features. We also discuss the existence of

different time-scales and address their microscopic origin.

4.2 Numerical Results

In this Section we present the results of numerical simulations for simple one-dimensional model systems whose Hamiltonian supports two bound states in the long-time limit. Of particular interest will be the dynamical part of the current and the dependence of the amplitude of the bound-state oscillations on the history of the time-dependent potential and on the initial state. We also identify single-particle transitions other than between the bound states which are relevant to understand the shape of the transient current.

The time-dependent, one-dimensional Hamiltonian is given by

$$H(x,t) = -\frac{1}{2}\frac{\mathrm{d}^2}{\mathrm{d}x^2} + U_0(x) + U(x,t) =: H^0(x) + U(x,t)\ . \tag{4.21}$$

For times $t \leq 0$ the Hamiltonian is $H^0(x)$ and the system is in its groundstate. At $t = 0$ the system is driven out of equilibrium by the time-dependent potential $U(x,t)$. We choose the time-dependent perturbation in such a way that for $t \to \infty$ the Hamiltonian globally converges to an asymptotic Hamiltonian, which we denote with $H^\infty(x)$.

The time-dependent perturbation $U(x,t)$ can be written as a piece-wise function of the space variable x. Let $W_\alpha(t)$ be the applied bias in region $\alpha = L, R$ and $V_g(x,t)$ the gate voltage applied to region C. The latter may depend on both position x and time t. Then

$$U(x,t) = \begin{cases} W_L(t) & -\infty < x < x_L \\ V_g(x,t) & x_L < x < x_R \\ W_R(t) & x_R < x < \infty \end{cases}\ , \tag{4.22}$$

with x_L and x_R being the positions of the left and right interfaces respectively. In our numerical implementation we discretize H on a equidistant grid and use a simple three-point discretization for the kinetic energy. In all systems studied below, the simulations have been performed by considering a propagation window which extends from $x_L = -1.2$ a.u. to $x_R = 1.2$ a.u. and a lattice spacing $\Delta x = 0.012$ a.u.. The occupied part of the continuous spectrum ranges from $k = 0$ to $k_\mathrm{F} = \sqrt{2\varepsilon_\mathrm{F}}$ and it is discretized with 200 k-points. All occupied states are propagated from $t = 0$ to $t = 1400$ a.u. using a time step $2\delta = 0.05$ a.u.. In the numerical examples studied below where the final

Hamiltonian supports two bound states the resulting current in the long-time limit is

$$I(t) = I^{(S)} + I_{\rm osc}(x)\sin(\omega_0 t), \tag{4.23}$$

i.e. on top of the steady current $I^{(S)}$, there is an oscillating part with only one frequency ω_0 given by the eigenenergy difference of the two bound states. It is also worth mentioning that the amplitude $I_{\rm osc}$ of this current oscillation depends on the position (see Eq. 4.17) while the steady-state current is position-independent.

4.2.1 Bound-state Oscillations and Transients

As a first example, we study a system with an initial potential $U_0(x) = 0$. Initially, the system is in the groundstate with Fermi energy $\varepsilon_{\rm F} = 0.1$ a.u.. All wavefunctions of the groundstate Slater determinant are extended one-particle states with energy between 0 and $\varepsilon_{\rm F}$. At $t = 0$, the system is suddenly driven out of equilibrium by switching on a potential $U(x,t)$ of the form (4.22) which consists of a constant bias in the left lead, $W_L = 0.1$ a.u., and a constant gate voltage in the central region, $V_g = -1.4$ a.u.. The biased Hamiltonian has two bound eigenstates with energies $\varepsilon^{\infty}_{b,1} = -1.032$ a.u. and $\varepsilon^{\infty}_{b,2} = -0.133$ a.u.. From the discussion of the previous Section we expect that a steady state cannot develop and that the time-dependent current exhibits an oscillatory behavior with frequency $\omega_0 = \varepsilon^{\infty}_{b,2} - \varepsilon^{\infty}_{b,1}$. This is indeed confirmed by our numerical simulations, as one can see in Fig. (4.1) where we plot the modulus of the discrete Fourier transform of the time-dependent current. The latter quantity is defined according to

$$I(\omega_k) = \frac{2\delta}{\pi\sqrt{2N_0}} \sum_{n=n_p}^{n_p+N_0} I(2n\delta)e^{-i\omega_k n\delta}, \quad \omega_k = \frac{2\pi k}{N_0\delta}. \tag{4.24}$$

We have computed $I(\omega_k)$ for different values of $n_p = (4+2p)\cdot 10^3$, $p = 0,1,2,3,4$, and $N_0 = 16\cdot 10^3$. Different values of p correspond to different time intervals $t \in (t_p, t_p + T_0)$ with $t_p = (2+p)\times 100$ a.u. but with the *same* duration $T_0 = 800$ a.u.. The coefficient in Eq. (4.24) is defined such that the height of the peak $I(\omega)$ at ω is equal to the amplitude of the oscillations with frequency ω. Besides the zero-frequency peak (not shown) due to the non vanishing dc current, $I(\omega)$ shows a dominant peak at the frequency $\omega_0 = \varepsilon^{\infty}_{b,2} - \varepsilon^{\infty}_{b,1}$ of the transition between the two bound states. As expected, the height of this peak remains unchanged as p varies from 0 to 4, i.e., the current oscillation associated with

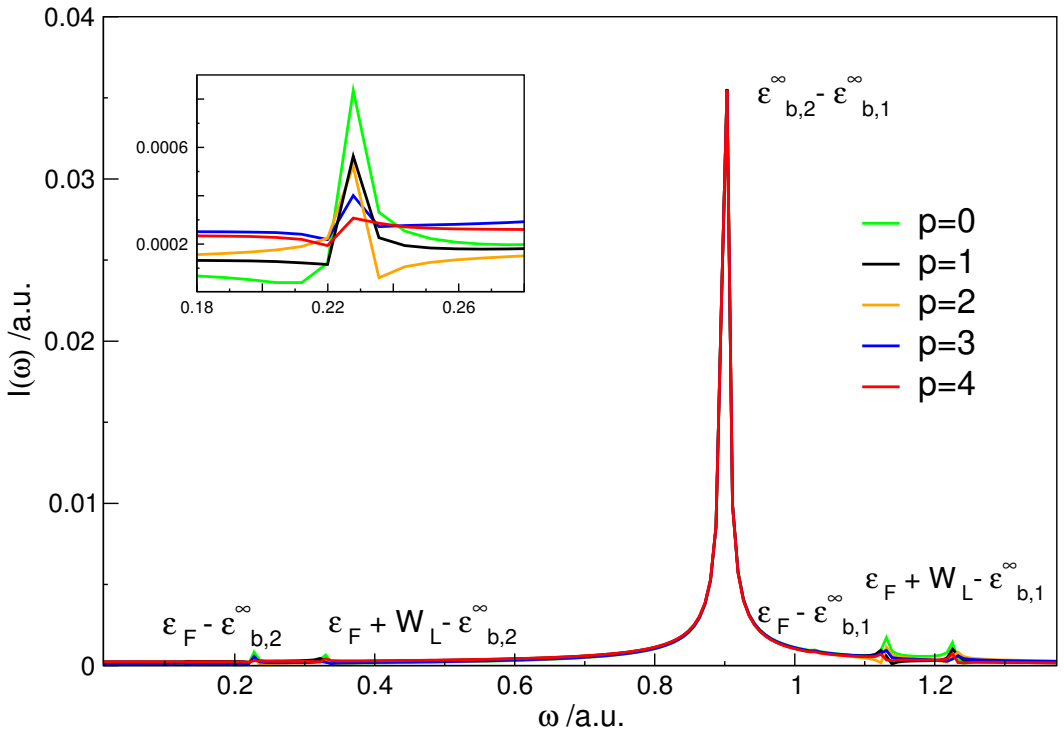

FIGURE 4.1: Modulus of the discrete Fourier transform of the current for $V_g = -1.4$ a.u. and a constant bias in the left lead $W_L = 0.1$ a.u.. The inset shows a magnification of the region with bound-continuum transitions from the bound state with higher energy to the Fermi energy. Different curves correspond to different time intervals.

this transition remains undamped. We emphasize that they are an intrinsic property of the biased system.

Closer examination of Fig. (4.1) reveals four extra peaks which are related to different internal transitions. The first and the last pairs of peaks occur at frequencies which correspond to transitions between the bound states and the lower edge of the unoccupied part of the continuous spectrum in the left and right lead of the biased system, $\varepsilon^{\infty}_{b,i} \to \varepsilon_{\mathrm{F}}$, and $\varepsilon^{\infty}_{b,i} \to \varepsilon_{\mathrm{F}} + W_L$, with $i = 1, 2$. These sharp structures (mathematically stemming from the discontinuity of the zero-temperature Fermi distribution function) give rise to long-lived oscillations of the total current and density. These oscillatory transients die off very slowly, the height of the peaks decreases with increasing t_p empirically as $1/t_p$. In Fig. (4.1), as well as in all following examples, we report results for the current calculated in the center of the device region. However it is important to note that the amplitude of the current oscillations decays exponentially in the leads as $e^{-(k^{\alpha}_{b,1}+k^{\alpha}_{b,2})|x-x_{\alpha}|}$ where $k^{\alpha}_{b,i} = \sqrt{2(|\varepsilon^{\infty}_{b,i}| + W_{\alpha})}$ with $i = 1, 2$, $\alpha = L, R$ and x is a point in lead α. The exponential decay of the density or current inside the leads can be easily understood by inserting the relation $\psi_{b,i}(x) = \psi_{b,i}(x_{\alpha})e^{-k^{\alpha}_{b,i}|x-x_{\alpha}|}$ into Eq. (4.17) for the current (or Eq. 4.28

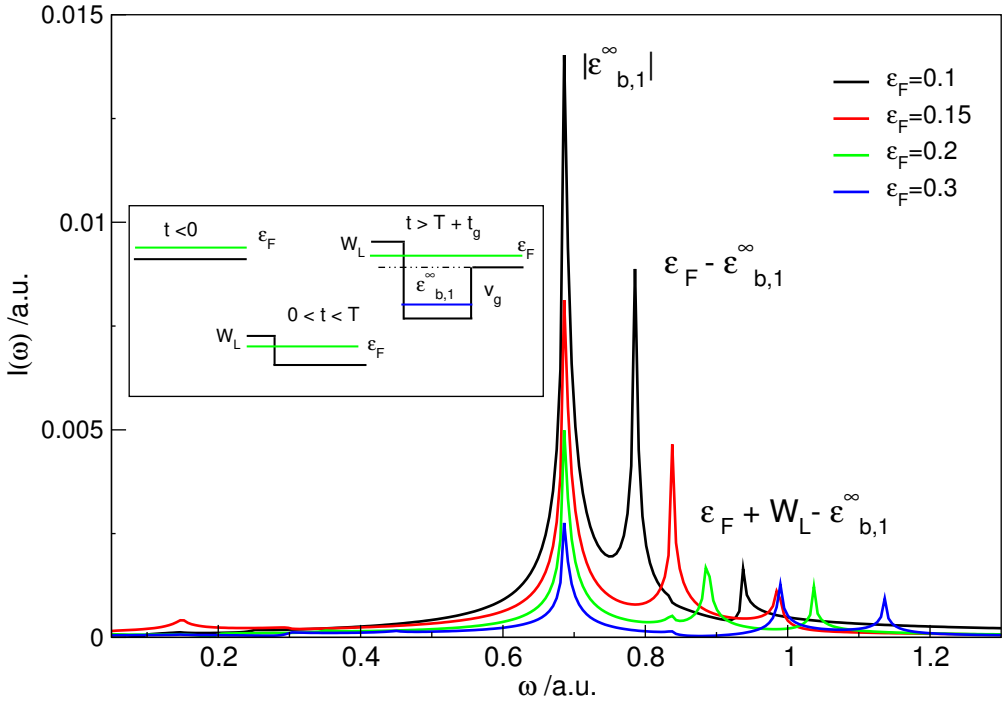

FIGURE 4.2: Modulus of the discrete Fourier transform of the current of a translationally invariant initial Hamiltonian which is perturbed at $t = 0$ by a sudden bias in the left lead $W_L = 0.15$ a.u. and the system evolves toward a steady state. Then, at $T = 150$ a.u. a gate voltage $V_g(x) = v_g = -1.02$ a.u. is suddenly turned on. (The inset shows a sketch of the time evolution of the applied bias and gate potentials.) The first peak appears at $\omega = 0.686$ a.u. which is the modulus of the energy of the bound eigenstate of the final Hamiltonian ($H(x, t > T)$ has one bound eigenstate). Different curves correspond to different Fermi energies.

for the density). Consequently, the dynamical part of the current vanishes deep inside the leads (away from where the bound states are localized). In the second example, we consider a system described initially by the translationally invariant Hamiltonian $H(x, t < 0) = -\frac{1}{2}\frac{\mathrm{d}^2}{\mathrm{d}x^2}$. At $t = 0$ we suddenly switch on a constant bias in the left lead $W_L = 0.15$ a.u. and propagate until $T = 150$ a.u. when a steady state is already reached. At $t = T$ a gate voltage $V_g(x) = v_g = -1.02$ a.u. is suddenly turned on and the Hamiltonian $H(x, t > T)$ has one bound eigenstate at energy $\varepsilon_b^\infty = -0.686$ a.u. . The depth v_g is chosen in such a way that if one slightly increases v_g a second bound eigenstate appears. Since the system has only one bound state, the oscillations die out slowly as $1/(t - T)$ and eventually another steady state is reached. In order to understand the transient oscillations we have studied the Fourier transform of the current as shown in Fig. (4.2). There the first peak appears at the frequency of $\omega = |\varepsilon_{b,1}^\infty|$ which is a transition between the bound level and the bottom of the continuum. As such, the position of this peak remains unchanged for different Fermi energies. Besides this transition one observes other peaks whose positions shift as the Fermi energy is changed. They correspond to

transitions from the bound level to the top of the left and right continua and, as for the first transition, they decay as $1/(t-T)$.

4.2.2 Dependence on Initial Conditions

The dynamical part of the current depends on the initial Hamiltonian $H^0(x)$ through the amplitudes $f_{b,b'}$ of Eq. (4.8). In the first example of the previous Section the Hamiltonian at negative times, $H^0(x)$, had no bound eigenstates. At positive times a gate voltage and a bias in the left lead were suddenly switched on and the Hamiltonian at positive times is equal to $H^\infty(x)$ and has two bound eigenstates. We now consider a system with two bound eigenstates for $t \leq 0$ which is exposed to a dc bias for $t > 0$. Specifically, we start with a static potential describing a quantum well of depth $U_0(x) = -1.4$ a.u. for $|x| < 1.2$ a.u.. The groundstate of the system is the Slater determinant of all the extended eigenstates with energy up to $\varepsilon_\mathrm{F} = 0.1$ a.u. and of the two bound eigenstates at energies $\varepsilon^0_{b,1} = -1.035$ a.u. and $\varepsilon^0_{b,2} = -0.156$ a.u.. At $t = 0$ a dc bias $W_R = 0.1$ a.u. is suddenly switched on in the left lead and the Hamiltonian $H(x, t > 0) = H^\infty(x)$ is equal to the final Hamiltonian studied in the previous Section. The resulting time-dependent current for these two systems are shown in Fig. (4.3).

As a consequence of the fact that $H^\infty(x)$ is the same in both systems the time-dependent currents should oscillate with the same frequency, a result which is confirmed by our numerical calculation. The amplitude of this oscillation, however, depends on the initial equilibrium configuration as well as on how $H(x,t)$ approaches the asymptotic Hamiltonian $H^\infty(x)$. As one can see from Fig. (4.3), the amplitude is much larger in the system with no initial bound states. This difference can be explained qualitatively by looking at Eq. (4.8). In both systems the time-dependent perturbation is switched on suddenly. Therefore, the memory matrix of Eq. (4.9) becomes the unit matrix and Eq. (4.8) reduces to

$$f_{b,b'} = \langle \psi^\infty_b | f(\boldsymbol{H}^0) | \psi^\infty_{b'} \rangle. \tag{4.25}$$

When the perturbation is small like in the case of the system with two initial bound states ($\boldsymbol{H}^0 \approx \boldsymbol{H}^\infty$), the eigenfunctions $|\psi^\infty_b\rangle$ of $\boldsymbol{H}^\infty$ are approximate eigenfunctions of $\boldsymbol{H}^0$ as well. Therefore $f(\boldsymbol{H}^0)|\psi^\infty_b\rangle \approx f(\varepsilon_b)|\psi^\infty_b\rangle$ and $f_{b,b'} \approx f(\varepsilon_b)\delta_{b,b'}$ which leads to a vanishing dynamical part of the current since there only the off-diagonal elements contribute. By

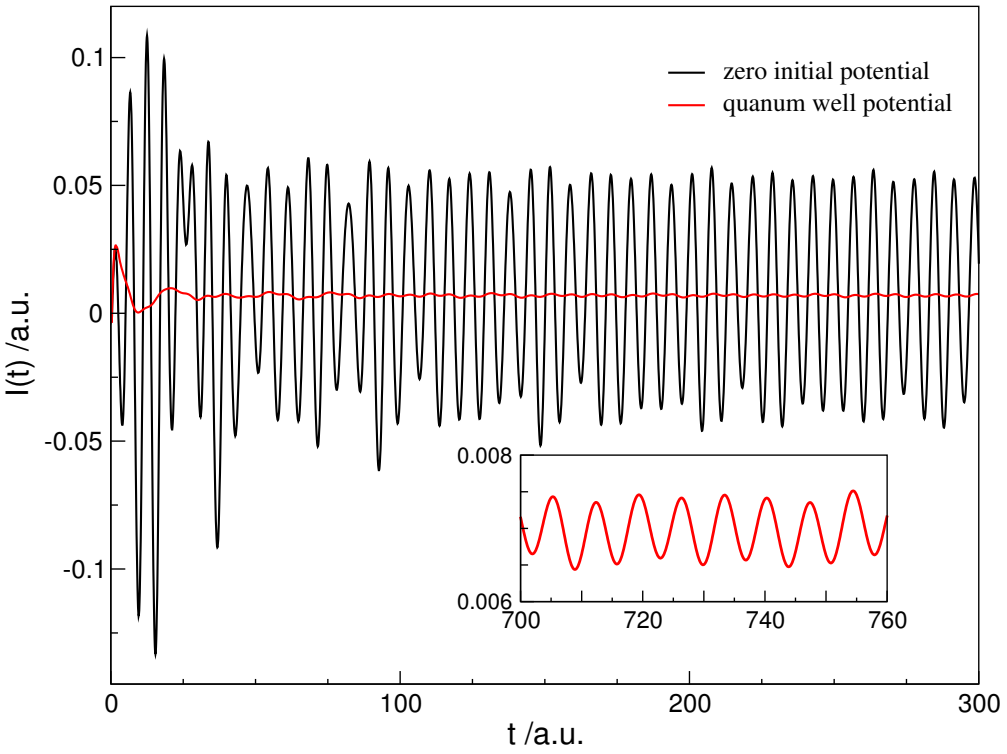

FIGURE 4.3: Comparison of the time-dependent current for systems with and without bound states at negative times. The inset shows a magnification of the time-dependent current of the system with two initial bound states. Since both systems have the same final Hamiltonian, the frequencies of the current oscillations are the same while the amplitude of the oscillations for the quantum well (with two bound states initially) is smaller by almost two orders of magnitude than for the system without initial bound states.

contrast, if the applied potential $U(x,t)$ is large, the overlap $\langle\psi_b^\infty|f(\boldsymbol{H}^0)|\psi_{b'}^\infty\rangle$ can be quite substantial and the resulting amplitude of the current oscillation is large.

4.2.3 History Dependence

4.2.3.1 Dependence of the Current Oscillations on the History of the Bias

The amplitude of the bound-state oscillations depends, through the memory matrix in Eq. (4.9), on the history of the time-dependent potential which perturbs the initial state. In this Section we investigate how the amplitude depends on the switching process (history-dependence effects).

We take the flat potential $U_0(x) = 0$ as initial potential and the Fermi energy $\epsilon_F = 0.2$ a.u.. At $t = 0$ a gate voltage $V_g(x) = -1.3$ a.u. abruptly lowers the potential in the center. In addition, a time-dependent bias is applied to the left lead as $W_L(t) = W_L \sin^2(\omega_b t)$ for $t \leq t_b = \frac{\pi}{2\omega_b}$ and $W_L(t) = W_L$ for $t > \frac{\pi}{2\omega_b}$, where $W_L = 0.1$ a.u..

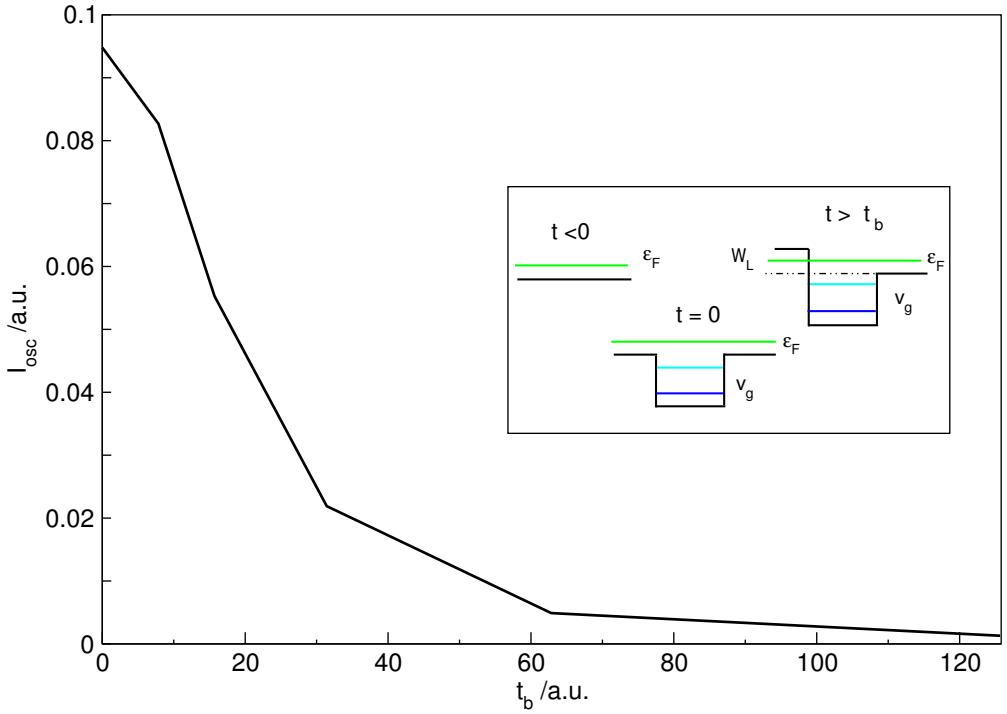

FIGURE 4.4: The amplitude of the current oscillation as function of the switching time of the bias. The bias in the left lead is switched according to $W_L(t) = W_L \sin^2(\omega_b t)$ for $t \leq t_b = \frac{\pi}{2\omega_b}$ and $W_L(t) = W_L = 0.1$ a.u. for later times. The frequency of the current oscillation $\omega_0 = \epsilon^\infty_{b,2} - \epsilon^\infty_{b,1}$ is given by the difference of bound state energies in the final system which have the values $\epsilon^\infty_{b,1} = -0.933$ a.u. and $\epsilon^\infty_{b,2} = -0.063$ a.u., respectively. The Fermi energy is $\epsilon_F = 0.2$ a.u. and the gate potential is $V_g = -1.3$ a.u.. Inset: potential landscape (external potential plus bias plus gate potential) for $t < 0$, $t = 0$, and $t > t_b$.

The final biased Hamiltonian has two bound states with energies $\epsilon^\infty_{b,1} = -0.933$ a.u. and $\epsilon^\infty_{b,2} = -0.063$ a.u. which again leads to undamped oscillations in the current.

Choosing t_b in such a way that Δ^∞_L (from Eq. (4.10)) equals 2π, 4π,... the upper block of the unitary matrix in Eq. (4.9) become the identity matrix in region L. This suggests that the amplitude of the current oscillations might exhibit a non-monotonic behavior as a function of the switching time. Our numerical results demonstrate that this is not the case. Fig. (4.4) shows that the amplitude decreases monotonically as a function of t_b, a trend which is expected in the region of long switching times (adiabatic switching). Such behavior, however, does not contradict the analytic results of Section (4.1). In fact, it is important to point out that the memory matrix in the central region $\boldsymbol{M}_C$ does not only depend on the history of the applied perturbation in the central region, but also on the way the bias is switched on through the time-dependent embedding self-energy needed to calculate $\boldsymbol{G}^A_{CC}(0;t)$, see Eq. (4.11). Hence, $\boldsymbol{M}_C \neq \mathbf{1}_C$ when $\Delta^\infty_L = 2\pi,\ 4\pi, \ldots$

4.2.3.2 Dependence of the Current Oscillations on the History of the Gate Voltage

To illustrate the dependence of the current oscillations on the switching process of the gate voltage, we first consider a system whose initial state is a Slater determinant of plane waves with energies less than $\epsilon_F = 0.1$ a.u. (a flat potential). At $t = 0$ we suddenly switch on a bias $W_L = 0.15$ a.u. in the left lead and as a result a current flows which after some transient time reaches a steady value of about 0.027 a.u.. After the steady state is attained, at time $T = 100$ a.u., we switch on a gate potential

$$V_g(x,t) = \frac{(t-T)}{t_g} v_g \tag{4.26}$$

for $T < t < T + t_g$ with a switching time $t_g = 20$ a.u. and the final depth of the potential well $v_g = -1.3$ a.u.. For times $t \geq T + t_g$ this gate potential remains unchanged at $V_g(x,t) = v_g$ and the final Hamiltonian supports two bound states at $\epsilon^{\infty}_{b,1} = -0.933$ a.u. and $\epsilon^{\infty}_{b,2} = -0.063$ a.u.. The resulting TD current in the center of the device region is shown in the upper panel of Fig. (4.5). The development of a steady-state current for $T < 100$ a.u. can clearly be recognized. After the bound states are created ($t > T + t_g$) the current starts to oscillate as expected. The amplitude of the current oscillation is of the order of 0.35 a.u., i.e., *more than an order magnitude larger than the steady-state current.*

The history dependence of the current oscillations can be seen by comparing the current in the upper and lower panels of Fig. (4.5). Both currents were computed by starting from the same initial state and applying the same bias at $t = 0$. In the lower panel we create the same, final potential as in the upper panel, but in two steps. At $T = 100$ a.u. we suddenly switch on a first gate potential with depth $v_g = -0.2$ a.u. which creates only one bound state. Waiting for the slow decay of the resulting bound-continuum transition we then apply an additional gate potential of depth $v_g = -1.1$ a.u. (hence the total depth is again 1.3 a.u.) with a switching time $t_g = 20$ a.u.. Again we recognize the persistent current oscillations due to the bound-bound transitions. Although the amplitude (about 0.07 a.u.) is still large compared to the steady-state current, it is about a factor of four smaller than the amplitude in the previous case.

To gain more insight into the dependence of the amplitude of the current (density) oscillations on the history of the gate voltage, in Fig. (4.7) the amplitude of the oscillation versus the switching time t_g is shown for a final depth of the gate $v_g = -1.3$ a.u. (the

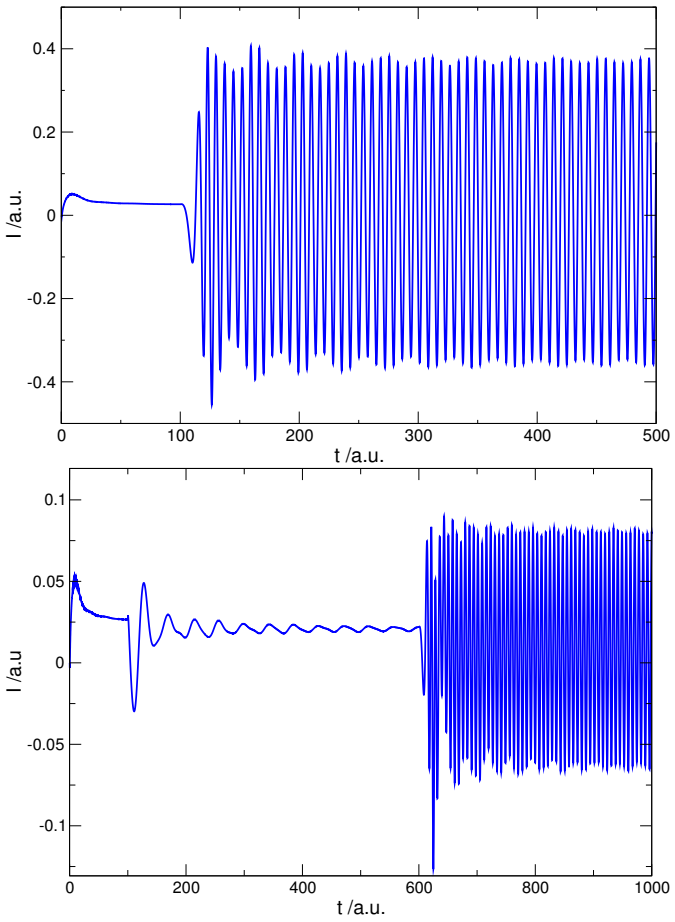

FIGURE 4.5: Time evolution of the current at $x = 0$. At $t = 0$ a.u., a bias $W_L = 0.15$ a.u. is suddenly switched on and the system evolves to a steady state. Upper panel: at $T = 100$ a.u., a gate potential is turned on ($v_g = -1.3$ a.u. and $t_g = 20$ a.u.) which creates two bound states and results in large amplitude oscillations of the current. Lower panel: at $T = 100$ a.u., a first gate potential ($v_g = -0.2$ a.u. and $t_g = 0$) is turned on which creates a single bound state. Waiting for the transients to decay, a second gate voltage ($v_g = -1.1$ a.u. and $t_g = 20$ a.u.) is then applied which leads to the formation of a second bound state and therefore to persistent current oscillations. Although $\boldsymbol{H}^{\infty}$ is identical in both cases, the amplitude of the current oscillation is significantly smaller in the second case, illustrating its dependence on the history of the system.

gate voltage is applied linearly as Eq. (4.26) at $T = 100$ a.u.). A sketch of the system in and out of equilibrium is shown in Fig. (4.6) which is similar to the system described in the upper panel of Fig. (4.5).

In the upper panel Fig. (4.7), the bias in the left lead is fixed to $W_L = 0.15$ a.u. and the Fermi energy is varied from $\varepsilon_{\mathrm{F}} = 0.1$ a.u. to 0.3 a.u.. We first note that in the limit of adiabatic switching ($t_g \to \infty$) the oscillation amplitude tends to zero. Furthermore we see that the amplitude reaches a maximum value for a certain switching time. It is also worth noting that the amplitudes are generally smaller for larger Fermi energies,

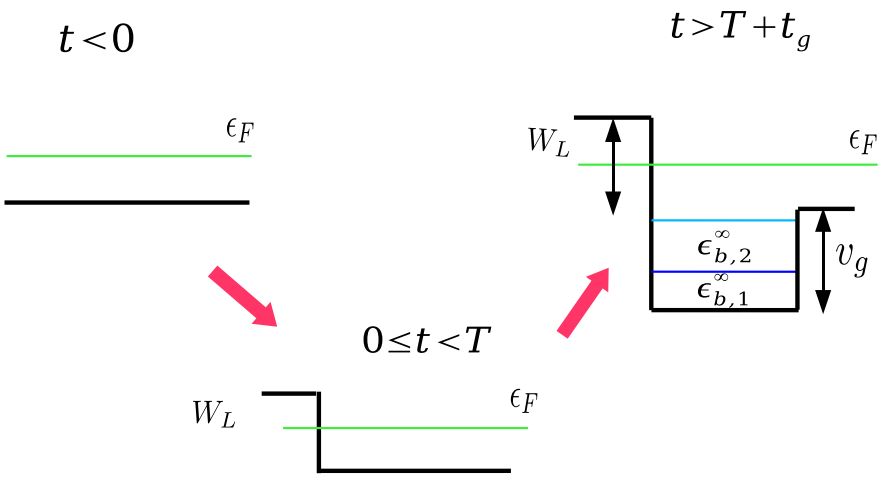

FIGURE 4.6: Sketch of the time evolution of the Hamiltonian. Starting from an initially constant potential (left), at $t = 0$ a bias is suddenly applied to the left lead and the system evolves toward a steady state (center). Then, between times T and $T + t_g$, a time-dependent gate voltage $V_g(x,t) = \frac{v_g}{t_g}(t-T)$ is switched on in region C. For times $t > T + t_g$ (right) the Hamiltonian remains constant in time.

a behavior which can be explained as follows: let $|\phi_n\rangle$ be an eigenstate of $\boldsymbol{H}^0$ with eigenenergy ε_n. Then

$$f_{b,b'} = \sum_{\varepsilon_n < \varepsilon_F} \langle \psi'_b | \phi_n \rangle \langle \phi_n | \psi'_{b'} \rangle. \tag{4.27}$$

As the Fermi energy increase the sum over ε_n approaches the sum over a complete set of eigenstates and hence $f_{b,b'}$ approaches the value $\langle \psi'_b | \psi'_{b'} \rangle$. This latter quantity vanishes since the states $|\psi'_b\rangle$ are related to the orthogonal states $|\psi^\infty_b\rangle$ by a unitary transformation and hence remain orthogonal. The lower panel of Fig. (4.7) shows the amplitude versus the switching time of the gate voltage for a fixed Fermi energy $\varepsilon_F = 0.2$ a.u. and for different values of the applied bias. The striking feature of this plot is that the position of the maximum remains almost unchanged as function of the bias W_L.

Interestingly, for the situation in which the gate voltage is applied in two steps (similar to lower panel of Fig. (4.5)) in such a way that the *first* bound state is created at $T = 100$ to the biased system and then after associated bound-continuum transitions have decayed another bound state is created by decreasing further down the gate voltage with a switching time t_g, the maximum amplitude of oscillations occur at a t_g close to zero. Similarly, in the case where the system initially has one bound state, the amplitude has a maximum for sudden switching of the gate, i.e., $t_g = 0$ a.u., while in the case with no initial bound states the maximum appears at a finite value of t_g.

To gain an intuitive understanding of the size of the oscillations as a function of the switching time of the gate t_g, we show in the next section how it is related to the

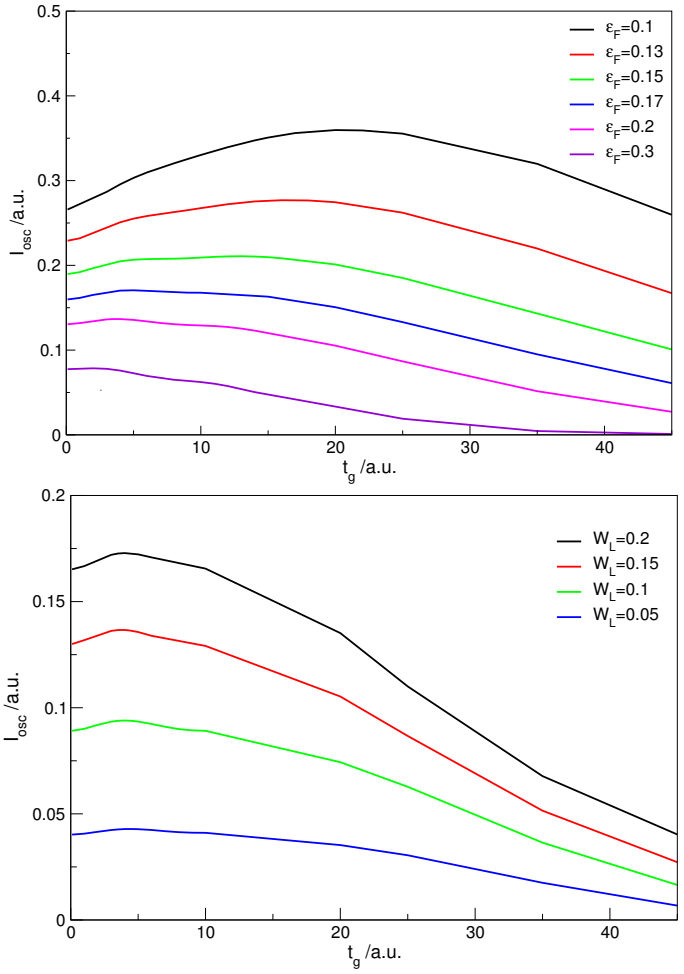

FIGURE 4.7: The amplitude of the current oscillations as function of the switching time t_g for $v_g = 1.3$ a.u.. Upper panel: for fixed bias $W_L = 0.15$ a.u. and different Fermi energies. Lower panel: for fixed Fermi energy $\varepsilon_{\rm F} = 0.2$ a.u. and different values of the bias. All curves reach a maximum whose position remains almost unchanged.

transition probability between the partially occupied bound states. In the last case(s) we mentioned the largest amplitude for the current oscillations is found for switching time t_g (close to) zero which is related to the fact that the first bound state is *almost* fully occupied. Therefore, the transition probability is maximum when the occupation of the second bound state reaches its lowest value. This happens for switching time t_g (close to) zero, leading to the largest oscillation amplitude. This is also supported by the following observation (see Fig. (4.7)): the switching time t_g for which the current oscillations are largest depends on the Fermi energy (for fixed bias) since the occupation of the bound states depend on $\varepsilon_{\rm F}$. At the same time, the position of this maximum is almost independent of the bias (for fixed Fermi energy) since the bias only leads to a slight energy shift for the bound states.

4.2.4 History-dependent Occupation of the Bound States

As discussed in Section. (4.1) the bound-state oscillations not only appear in the current but also in the density, and memory effects in the amplitude of the density oscillations are seen as well. The dynamical contribution to the density is given by

$$n^{(D)}(\boldsymbol{r},t)=\sum_{b,b'}f_{b,b'}\cos[(\epsilon_b^\infty-\epsilon_{b'}^\infty)t]\psi^{*\infty}_{b'}(\boldsymbol{r})\psi_b^\infty(\boldsymbol{r}). \tag{4.28}$$

where the amplitudes $f_{b,b'}$ are again given by Eq. (4.8). We observe that while the diagonal term, $b=b'$, does not contribute to the current of Eq. (4.16), it does contribute to the density of Eq. (4.28) with a history-dependent coefficient $f_{b,b}$. This means that even if we average out the density oscillations, history-dependent effects will show up in the density at the device region. The *time-independent* part arising from the diagonal ($b=b'$) contributions to the double sum in Eq. (4.28) reads

$$n^{(D)}(\boldsymbol{r})=\sum_b f_{b,b}|\psi_b^\infty(\boldsymbol{r})|^2. \tag{4.29}$$

The coefficients $f_{b,b}$ can be interpreted as occupation numbers of the bound states in the long-time limit. We further notice that also the bound-state occupations $f_{b,b}$ depend on the initial condition and on the history of the time-dependent perturbation through the memory operator $\boldsymbol{M}$. In fact, *the TD description provides a natural solution to the problem of how to populate bound states in transport calculations* a problem which is not treated properly in the static approaches to transport, e.g., L+DFT or NEGF+DFT. In these approaches, bound states below the bias window are entirely populated, (i.e. $f_{b,b}=1$), while bound states within the bias window are populated in a somewhat artificial way by hand with some ad-hoc choice for the occupation numbers [47]. Of course, due to its self-consistent nature, the solution of the NEGF+DFT approach is affected by this somewhat arbitrary choice of bound-state occupations. Here we show that the assumption that bound states are entirely populated below the bias window is *only* valid in the case of adiabatic switching of the time-dependent perturbation.

To illustrate the existence of memory effects in the *time-independent* part of the density we have computed $n_{\rm av}(x)$, the time-dependent density averaged over an oscillation period for a system with two bound states in the final Hamiltonian. The system is the one which leads to the current shown in the the upper panel of Fig. (4.5) except that the gate

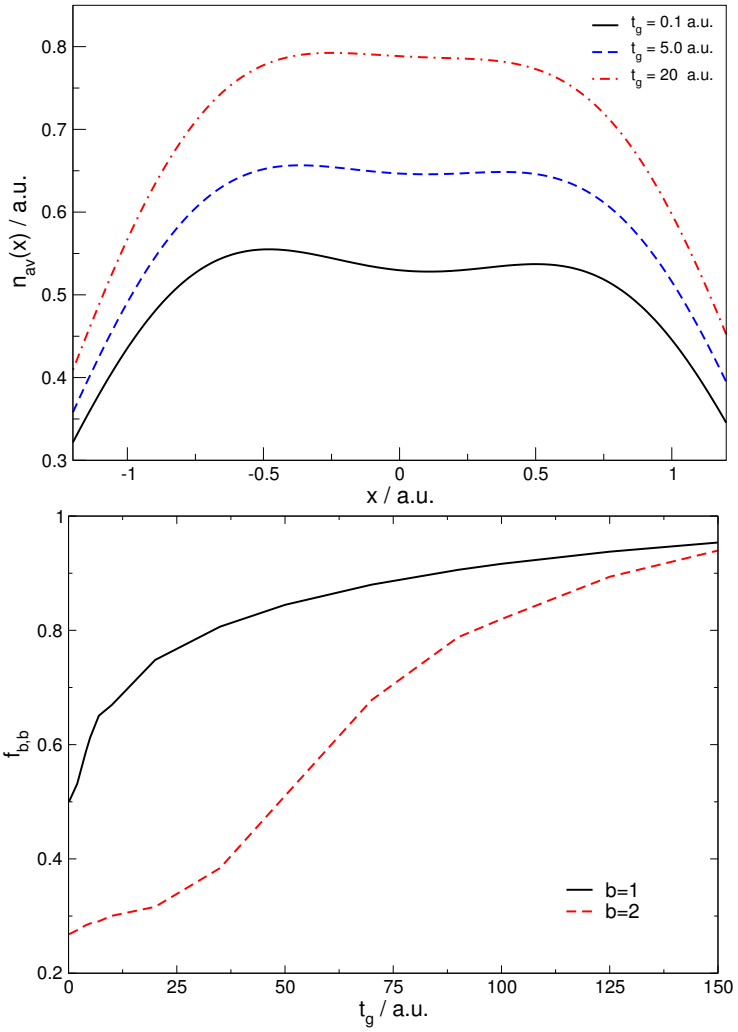

FIGURE 4.8: Upper panel shows memory effects for the static part of the density in the long-time limit in the presence of bound states. The densities shown here correspond to systems which are identical to the one studied in the upper panel of Fig. (4.5) except that they are computed for three different switching times of the gate potential of Eq. (4.26): $t_g = 0.1$ a.u. (solid, black), $t_g = 5.0$ a.u. (dashed, blue), and $t_g = 20$ a.u. (dash-dotted, red). The lower panel shows the occupation numbers $f_{b,b}$ (Eq. (4.8)) of the two bound states as function of switching time. The state with lower energy eigenvalue ($b = 1$) has higher occupation than the one with higher energy. For short switching times the occupation is significantly smaller than one, while for adiabatic (slow) switching both occupation numbers approach one.

potential is turned on with different switching times t_g. In the upper panel of Fig. (4.8) we show $n_{\rm av}(x)$ for three different t_g and, as one can see, the corresponding $n_{\rm av}(x)$ *differ quite substantially*. This difference has to be attributed to bound states since for the contribution of the scattering states all memory is washed out [29]. Of course, the relative importance of the bound-state contribution to $n_{\rm av}(x)$ will decrease when $\epsilon_{\rm F}$ (and therefore the contribution of the continuum states) increases. By subtracting the continuum contribution from $n_{\rm av}$ and fitting the explicit function $n^{(D)}$ with the

numerical curve (where the only fitting parameters are the coefficients $f_{b,b}$ for $b = 1, 2$) the bound-state occupations $f_{b,b}$ can be calculated. Those are shown in the lower panel of Fig. (4.8) as a function of t_g. Remarkably we find that $f_{b,b}$ *exhibits rather large deviations from unity*, especially for small switching times. In other words, choosing full occupation ($f_{b,b} = 1$) for the bound states below the bias window is *justified only for the case of adiabatic switching.* As one would intuitively expect, the occupation of the state with lower energy ($b = 1$) is larger than for the state with higher energy. In the adiabatic limit of very slow switching ($t_g \to \infty$), both occupation numbers approach unity which is expected since both states are energetically below ϵ_{F}.

Moreover, the occupation numbers offer an intuitive qualitative picture of the size of the current and density oscillations: for relatively short switching times ($t_g \leq 50$ a.u.) the occupation numbers deviate substantially from one. Therefore the transition probability between the bound states is relatively large and so are the oscillations in current and density. Remarkably, for the switching time t_g with the largest oscillations amplitude (see black curve in the upper panel of Fig. (4.7) where the largest oscillations occur for $t_g = 20$ a.u.), the difference between the occupation of the first and second bound state attains its highest value (see lower panel of Fig. (4.8)). On the other hand, for large switching times both bound states are almost "fully" occupied and the probability of a transition between them is small, leading to small amplitudes in the dynamical density.

4.3 Conclusions

In the theory of electron transport one usually assumes that the application of a dc bias to an electronic system attached to two macroscopic electrodes always leads to the formation of a steady-state current. However, the presence of bound states leads to qualitatively new features (current oscillations and memory effects) in the dynamics of electron transport in the long-time limit [43]. These as well as transient features are investigated in detail by numerical simulations in this Chapter. In the Fourier transform of the calculated time-dependent current one not only finds the predicted transitions between the bound states in the long-time limit, but also transitions in the transient regime between the bound states and the continuum of the leads. In summary we have demonstrated that 1) the persistent current oscillations in the presence of bound states can be much larger than the steady-state current 2) the amplitude of the current

oscillations can have a strong dependence on the history of the system 3) a similar history dependence is found for the contribution of the bound states to the density and 4) the occupation of bound states below and *within* the bias window is well defined in a TD description of quantum transport. These results are of great importance for all transport calculations: the first three points challenge one of the fundamental assumptions of the Landauer formalism (the assumption that a unique steady state always develops) while the fourth point solves the problem of properly defining the bound-state occupations. Hence the TD approach to transport provides a natural, unified framework to describe current oscillations, memory effects and bound-state occupations.

Our results indicate that in transport calculations special care has to be taken if bound states are present in the biased system.
In fact, it should be pointed out that the existence of bound states in biased transport systems may not be an exotic feature in an experimental situation. For single molecules attached to metallic leads it is quite conceivable that some of the molecular orbitals energetically fall into an energy window which corresponds to an energy gap of the leads and those orbitals therefore cannot hybridize with any lead states and remain fully localized. In the case of transport experiments on quantum dots one could artificially create bound states by applying an attractive gate potential.
In this chapter, electron-electron and electron-phonon interactions have not been included. In real systems, of course, electron-phonon scattering leads to a level broadening and hence damping of the oscillations with a typical time scale of picoseconds. The question if these oscillations in principle can be seen experimentally then becomes a matter of time scales. We emphasize that since ultimately one wants to exploit the ability of molecular electronics devices to switch on the electronic time scale (femtoseconds), phononic damping , which is governed by the nuclear time scale (hundreds of femtoseconds or picoseconds), is less important. Hence the bound-state oscillations become extremely relevant on this time scale.
To assess the role of the electron-electron interaction, we point out that the entire formalism remains valid for any effective single-particle theory such as, e.g. TDDFT which can treat interactions in principle exactly.

In the presence of bound-states, essentially two situations are conceivable: in the first scenario the effective single-particle potential converges to a time-independent potential supporting bound states for which Eq. (4.13) applies leading to oscillating currents in

the long time limit $t \to \infty$. This may well be consistent with a time-independent Kohn-Sham potential for $t \to \infty$ because the exact Hartree plus exchange-correlation potential may well become time-independent even if the density is oscillatory.

In the second scenario, the effective single-particle potentials are time-dependent with the bound states eigenenergy differences as prominent frequencies. In that case the density will again be time-dependent for $t \to \infty$ by virtue of Floquet's theorem. This situation can even be captured by simple exchange-correlation functionals which are local in time such as, e.g., Adiabatic Local Density Approximation (ALDA) or generalized gradient approximations. This is shown for an ALDA calculation presented in Fig 7.12.

Although this argument is clearly not mathematically rigorous, the in principle exact single-particle nature of the TDKS equations suggests that even in the presence of electron-electron interactions oscillations will appear on the femtosecond time scale.

This opens up the possibility of having oscillatory solutions for constant biases and may change substantially the standard steady-state picture already at the level of exchange-correlation functionals which are local or semi-local in time. On the other hand, the asymptotic ($t \to \infty$) density depends on the occupation coefficients $f_{b,b}$ which in turn depend on the history of the TDDFT potential. Thus, history-dependent effects might be found even at the level of the ALDA.

Finally, we wish to point out that probes with high spatial resolution would be needed to observe bound-state oscillations experimentally as they are localized in the device region.

Chapter 5

Time-dependent Quantum Transport through Model Devices with On-site Interaction: Different Approaches

5.1 The Model

In the next three chapters we consider an interacting nanoscale device contacted to two non-interacting leads. The whole system is initially in equilibrium at a given temperature and chemical potential. At time t_0, we switch on a bias between the leads and follow the time evolution of the perturbed system.

The Hamiltonian of the system can be split into three different parts as

$$\hat{H}(t) = \hat{H}_C(t) + \sum_{\alpha=L,R} \hat{H}_\alpha(t) + \hat{H}_T \; . \tag{5.1}$$

Here, $H_C(t)$ describes the device, $\hat{H}_\alpha(t)$ is the Hamiltonian for lead α, and $\hat{H}_T$ is the coupling Hamiltonian between the device and the leads. To be specific, we consider devices which consist of a tight-binding chain with nearest neighbor hopping and a

short range electron-electron interaction of the Hubbard form

$$\begin{aligned}\hat{H}_C(t) &= \sum_{\substack{i=1\\\sigma}}^{N_C} \varepsilon_i^C(t)\hat{d}_{i\sigma}^\dagger \hat{d}_{i\sigma} - \sum_{\substack{i=1\\\sigma}}^{N_C-1} (V_C \hat{d}_{i\sigma}^\dagger \hat{d}_{i+1\sigma} + H.c.) \\ &\quad + \frac{1}{2}\sum_{\substack{i=1\\\sigma\sigma'}}^{N_C} U \hat{d}_{i\sigma}^\dagger \hat{d}_{i\sigma'}^\dagger \hat{d}_{i\sigma'} \hat{d}_{i\sigma} \end{aligned} \tag{5.2}$$

where i labels the N_C sites of the interacting chain, σ and σ' are spin indices, and $\hat{d}_{i\sigma}^\dagger$ and $\hat{d}_{i\sigma}$ denote creation and annihilation operators for electrons with spin σ at site i. The $\varepsilon_i^C(t)$ are on-site energies which may contain an arbitrary, explicit time dependence, V_C is the nearest-neighbor hopping in the chain and U is the on-site Hubbard interaction.

The non-interacting left (L) and right (R) leads $\alpha = L, R$ are described by one-dimensional semi-infinite chains with Hamiltonian

$$\begin{aligned}\hat{H}_\alpha(t) &= \sum_{\substack{i=1\\\sigma}}^{\infty} \left(\varepsilon_\alpha + W_\alpha(t)\right) \hat{c}_{i\sigma\alpha}^\dagger \hat{c}_{i\sigma\alpha} \\ &\quad - \sum_{\substack{i=1\\\sigma}}^{\infty} \left(V_\alpha \hat{c}_{i\sigma\alpha}^\dagger \hat{c}_{i+1\sigma\alpha} + H.c. \right) \end{aligned} \tag{5.3}$$

with creation (annihilation) operators $\hat{c}_{i\sigma\alpha}^\dagger$ ($\hat{c}_{i\sigma\alpha}$) for electrons with spin σ at site i in lead α. The on-site energies ε_α and the hopping matrix elements V_α are independent of time and site index while $W_\alpha(t)$ describes a time-dependent, site-independent bias applied to lead α.

Finally, the tunneling Hamiltonian which couples the leads to the device is given by

$$\hat{H}_T = -\sum_\sigma \left(V_{\text{link}} \hat{d}_{1\sigma}^\dagger \hat{c}_{1\sigma L} + V_{\text{link}} \hat{d}_{N_C\sigma}^\dagger \hat{c}_{1\sigma R} + H.c. \right), \tag{5.4}$$

where we have adopted the convention that the site in lead α connecting to the device is labelled by the site index 1.

5.2 Time-dependent Approach to Transport

In the next chapters we study the time-dependent quantum transport for the model introduced in the previous Section using two different approaches: MBPT and TDDFT.

The time-dependent MBPT formulation of transport [48, 49] is based on the time evolution of the Green function via the Kadanoff-Baym (KB) equations [50–52]. The central quantity entering the MBPT approach is the many-body self-energy Σ_{MB} which can be approximated by selecting the class of Feynman diagrams relevant for the description of the main scattering processes. The computational cost to propagate the Kadanoff-Baym equations is rather high such that applications have to be restricted to small systems and short propagation time.

On the other hand, TDDFT [53] offers an alternative, in principle exact, framework to account for correlation effects both in the leads and the central region [28, 29]. Moreover, since TDDFT only involves the propagation of effective single-particle equations, it is a computationally efficient way to describe time-dependent transport [30]. The downside of TDDFT is that the construction of accurate approximations for the exchange-correlation potential is highly non-trivial. The most popular approximation, ALDA, depends only on the local and instantaneous density, i.e., it does not include memory effects.

5.2.1 Time-dependent Density Functional Theory

In TDDFT, the problem of interacting electrons is mapped, in principle exactly, on the much simpler problem of non-interacting electrons moving in an effective, local potential [53]. This effective potential, the KS potential, is itself an unknown functional of the time-dependent density and the difficulty lies in constructing accurate approximations to this functional. Below we will discuss in detail which functional we choose for our investigation.

In the context of TDDFT applied to quantum transport, the complexity of describing an infinite non-periodic system, or equivalently, a finite open system attached to semi-infinite leads, can be reduced to an equation of motion for the central region only. In the one-particle Hilbert space, the KS Hamiltonian is a matrix which can be partitioned as

$$\begin{pmatrix} \mathbf{H}_{LL}^{KS}(t) & \mathbf{H}_{LC} & 0 \\ \mathbf{H}_{CL} & \mathbf{H}_{CC}^{KS}(t) & \mathbf{H}_{CR} \\ 0 & \mathbf{H}_{RC} & \mathbf{H}_{RR}^{KS}(t) \end{pmatrix}, \tag{5.5}$$

where $\mathbf{H}_{CC}^{KS}(t)$ is the Hamiltonian of the isolated device and $\mathbf{H}_{\alpha\alpha}^{KS}(t) = \mathbf{H}_{\alpha\alpha}^{KS} + \boldsymbol{W}_{\alpha}^{KS}(t)$ are the Hamiltonians of the isolated leads $\alpha = L, R$.

As discussed in Chapter 3, we assume instantaneous screening in the metallic leads, $\boldsymbol{W}_{\alpha}^{KS}(t) = W_{\alpha}(t)\mathbf{1}_{\alpha}$ with $\mathbf{1}_{\alpha}$ the identity matrix projected onto lead $\alpha = L, R$. Finally, $\mathbf{H}_{\alpha C}$ describes the coupling between lead α and the device. Here and in the following we will use boldface to indicate matrices in one-electron labels.

The equation of motion for the k-th KS single-particle orbital $\psi_{k,C}(t)$ projected onto the central region reads

$$\left[i\partial_t - \mathbf{H}_{CC}^{KS}(t)\right]|\psi_{k,C}(t)\rangle = \int_0^t \mathrm{d}\bar{t}\; \boldsymbol{\Sigma}_{\mathrm{em}}^{R}(t,\bar{t})|\psi_{k,C}(\bar{t})\rangle + \sum_{\alpha} \mathbf{H}_{C\alpha}\mathbf{g}_{\alpha\alpha}^{R}(t,0)|\psi_{k,\alpha}(0)\rangle. \tag{5.6}$$

The coupling of the central region to the leads is accounted for in an exact way by the retarded embedding self-energy

$$\boldsymbol{\Sigma}_{\mathrm{em}}^{R}(t,t') = \sum_{\alpha=L,R} \mathbf{H}_{C\alpha}\mathbf{g}_{\alpha\alpha}^{R}(t,t')\mathbf{H}_{\alpha C}, \tag{5.7}$$

which describes virtual processes where an electron in the device hops onto the leads at time t' and then hops back onto the device at time t. As discussed in Chapter 3, the quantity $\mathbf{g}_{\alpha\alpha}^{R}(t,t')$ is the retarded Green function of the isolated semi-infinite lead α and satisfies the equation of motion

$$\left[i\partial_t - \mathbf{H}_{\alpha\alpha}^{KS}(t)\right]\mathbf{g}_{\alpha\alpha}^{R}(t,t') = \delta(t,t'), \tag{5.8}$$

with boundary conditions $\mathbf{g}_{\alpha\alpha}^{R}(t,t^{+}) = -i\mathbb{1}_{\alpha}$ and $\mathbf{g}_{\alpha\alpha}^{R}(t,t^{-}) = 0$. In our model the KS Hamiltonian matrix $\mathbf{H}_{CC}^{KS}(t)$ has a tridiagonal form where the only non-vanishing entries are the off-diagonal matrix elements $[\mathbf{H}_{CC}^{KS}(t)]_{j,j+1} = [\mathbf{H}_{CC}^{KS}(t)]_{j+1,j} = -V_C$ with $j = 1, \cdots, N_C - 1$, and the diagonal matrix elements

$$\begin{aligned}[\mathbf{H}_{CC}^{KS}(t)]_{jj} &= v_{\mathrm{KS}}(j,t) \\ &= \varepsilon_j^{C}(t) + v_H(n_j(t)) + v_{\mathrm{xc}}[n](j,t),\end{aligned} \tag{5.9}$$

with $j = 1, \cdots, N_C$.

The time-dependent density at site j in general is given by

$$n_j(t) = -2i[\mathbf{G}_{CC}^{<}(t,t^{+})]_{jj}, \tag{5.10}$$

where t^{+} approaches t from an infinitesimally later time $t^{+} = t + \delta$. Within TDDFT $\mathbf{G}_{CC}$ in Eq. 5.10 is replaced by $\mathbf{G}_{CC}^{KS}$. Due to the non-interacting nature of $\mathbf{G}_{CC}^{KS}$, Eq. 5.10

simplifies and in particular at zero temperature, it reduces to

$$n_j(t) = 2\sum_{k}^{\text{occ}} |\psi_{k,C}(j,t)|^2, \tag{5.11}$$

where the sum runs over the occupied KS orbitals and the pre-factor is due to spin degeneracy. The second term on the r.h.s of Eq. 5.9 is the Hartree potential and the third term is the exchange-correlation potential of TDDFT. The XC potential $v_{\text{xc}}[n](j,t)$ depends on the time-dependent density at *all times* earlier than t and in *all sites* of the system (including the leads). Of course, the exact form of $v_{\text{xc}}[n]$ is unknown and in practice one has to resort to approximations. It is worth to point out that, independent of the particular form used for v_{xc}, already at this point we make the approximation that the XC part of the KS potential vanishes identically inside the leads. We discuss this issue further in Chapter 8. Although in our model Hamiltonian (Eq. 5.1) the interaction is restricted to the device region only, the exact KS potential for this system will have XC contributions in the lead regions adjacent to the central device and will rigorously vanish only deep inside the leads. Setting v_{xc} equal to zero in the leads is not a principal limitation of the TDDFT approach but rather a simplifying approximation: We could have incorporated a finite portion of the leads in our explicitly treated region, thereby accounting for the aforementioned effect.

In the next section, we will introduce the approximation for the XC potential we use which is based on the local density approximation (LDA) derived from the exact Bethe-ansatz solution of the static, uniform one-dimensional Hubbard model.

5.2.1.1 Exchange-correlation Potential of the Hubbard Model

From the exact Bethe-ansatz solution to the homogeneous 1D Hubbard model (1DHM) [54] , one can extract analytical expressions for the total groundstate energy in several important limiting cases.

For infinitely strong interactions ($U \to \infty$) and less than half-filled band ($n < 1$) the per volume energy e reads

$$e(n, V, U \to \infty) = -\frac{2V}{\pi}\sin(\pi n). \tag{5.12}$$

In addition, in the absence of interaction ($U = 0$) and $n < 1$ it is easy to show that

$$e(n, V, U = 0) = -\frac{4V}{\pi} \sin(\frac{\pi}{2} n). \tag{5.13}$$

Finally, for an exactly half-filled band ($n = 1$) and any interaction U

$$e(n = 1, V, U) = -4V \int_0^\infty \mathrm{d}x \, \frac{J_0(x) J_1(x)}{x[1 + \exp(Ux/(2V))]} \tag{5.14}$$

where J_0 and J_1 are the zeroth and first order Bessel functions respectively.
By interpolating these limiting cases, the Bethe Ansatz LDA (BALDA) groundstate energy is obtain for intermediate values of the density and interaction. Motivated by the similarity of the limiting expressions for $U = 0$ and $U \to \infty$ the following functional form is adopted [55]

$$e(n, V, U) = -\frac{2V\xi(U/V)}{\pi} \sin(\frac{\pi}{\xi(U/V)} n) \tag{5.15}$$

where ξ is a function of the ratio U/V. To guarantee the correct result for half filling, Eq. 5.15 at $n = 1$ and Eq. 5.14 must give the same value, and therefore

$$\frac{\xi(U/V)}{\pi} \sin(\frac{\pi}{\xi(U/V)}) = 2 \int_0^\infty \mathrm{d}x \, \frac{J_0(x) J_1(x)}{x[1 + \exp(Ux/(2V))]}. \tag{5.16}$$

This equation determines ξ for all values of U, including the limiting cases. In the limit of infinite (zero) interaction strength, U, the integral of Eq. 5.16 has an analytical solution which indeed recovers $\xi = 1$ ($\xi = 2$). For intermediate values of U, ξ is a number between one and two calculated only once outside the self-consistency cycle of DFT.

For a more than half-filled band, a particle-hole transformation can be used to express the energy in terms of the energy of a less than half-filled band:

$$e(n > 1, V, U) = e(2 - n, V, U) + (n - 1)U \ . \tag{5.17}$$

This completes the interpolation of the groundstate energy of the 1DHM.
Note that this procedure slightly deviates from the usual LDA because it is based on the three exact limiting cases. Hence it is exact only in the limiting cases introduced above. However, the groundstate energy calculated from BALDA is in excellent agreement with the one obtained from numerically solving the Lieb-Wu integral equations following from the Bethe Ansatz [54].

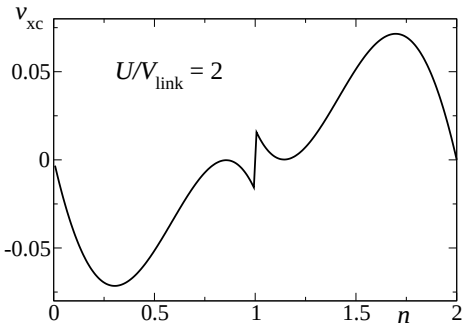

FIGURE 5.1: The BALDA XC potential as a function of the density for $U = 1$ and $V_{\text{link}} = 0.5$.

Having the per-volume energy $e(n, V, U)$ the total energy of the 1DHM is :

$$E^{\text{BALDA}}[n_1, n_2, n_3, \dots] = \sum_i e(n, V, U)\Big|_{n \to n_i}. \tag{5.18}$$

To extract the exchange-correlation energy, the non-interacting kinetic energy and the Hartree energy are subtracted from the total energy

$$\begin{aligned} e_{\text{xc}}(n, V, U) &= e(n, V, U) - t_s - e_H(n, U) \\ &= e(n, V, U) - e(n, V, 0) - e_H(n, U). \end{aligned} \tag{5.19}$$

For a homogeneous system the Hartree energy is defined as $e_H(n, U) = Un^2/4$ and the non-interacting kinetic energy is simply given by $e(n, V, 0)$, since for $U = 0$ the Hamiltonian of the 1DHM contains only the kinetic energy term. The XC potential is obtained by taking the derivative of e_{xc} (Eq. 5.19) with respect to density n. This yields

$$v_{\text{xc}}[n] = \theta(1-n)v_{\text{xc}}^{<}[n] - \theta(n-1)v_{\text{xc}}^{<}[2-n], \tag{5.20}$$

$$v_{\text{xc}}^{<}[n] = -\frac{1}{2}Un - 2V\left[\cos\left(\frac{\pi n}{2}\right) - \cos\left(\frac{\pi n}{\xi}\right)\right]. \tag{5.21}$$

Note that the original BALDA functional [55] is devised for the uniform 1D Hubbard model with Hubbard interaction U on all sites and hopping V between the sites, such that U/V is the relevant parameter in v_{xc}.

In the next Chapters, however, we are interested in studying time-dependent transport through an interacting device weakly connected to effectively non-interacting leads. Since the system is highly inhomogeneous in this case, we use a modified version of this

functional where $U/V_{\rm link}$ becomes the relevant parameter. For the case of a single interacting impurity site ($N_C = 1$) the modified BALDA, reads explicitly

$$v_{\rm xc}^{<}(n) = -\frac{1}{2}Un - 2V_{\rm link}\left[\cos\left(\frac{\pi n}{2}\right) - \cos\left(\frac{\pi n}{\xi}\right)\right] . \tag{5.22}$$

Here, ξ is a parameter determined by the equation

$$\frac{2\xi}{\pi}\sin(\pi/\xi) = 4\int_0^\infty {\rm d}x\, \frac{J_0(x)J_1(x)}{x[1+\exp(Ux/(2V_{\rm link}))]} \tag{5.23}$$

In this thesis we use the same functional also for more than one site in the chain ($N_C > 1$) with the additional restriction that in this case we only consider models for which the hopping V_C in $\mathbf{H}_{CC}$ is equal to the hopping $V_{\rm link}$ from the chain to the leads.

A particularly interesting property of the BALDA is its discontinuity at half filling [55]: $v_{\rm xc}(1^+) - v_{\rm xc}(1^-) = U - 4V_{\rm link}\cos(\frac{\pi}{\xi})$. Note that due to the deficiency of the BALDA functional, this term can be negative for small $U/V_{\rm link}$. This point is explained in more detail in the next chapter.

In Fig 5.1 we display the typical behavior of the BALDA potential as a function of the density. For our later analysis it is important to observe that $v_{\rm xc}$ is very small when the density is close to 0, 1 or 2.

5.2.2 Many-body Technique: Kadanoff-Baym Equations

The MBPT approach to study systems out of equilibrium consists in propagating the Green function in time according to the Kadanoff-Baym equations [50]. For times $t < t_0$ the whole system (central device plus left and right leads) is in thermal equilibrium at chemical potential μ and inverse temperature β. At $t = t_0$ an external bias is switched on, thereby driving the system out of equilibrium.

The nonequilibrium (Keldysh) Green function is defined as the thermal average of the contour ordered product [45]

$$G(1,2) = -i\frac{{\rm Tr}\{\hat{U}(t_0 - i\beta, t_0)\mathcal{T}_{\mathcal{C}}[\hat{\psi}_H(1)\hat{\psi}_H^\dagger(2)]\}}{{\rm Tr}\{\hat{U}(t_0 - i\beta, t_0)\}} \tag{5.24}$$

where $\mathcal{T}_{\mathcal{C}}$ is the contour-time ordering operator along the Keldysh contour [56] $\mathcal{C}$ of Fig 5.2, $\hat{U}$ is the contour evolution operator and $\hat{\psi}_H$ are the fermionic operators $\hat{d}$ (for

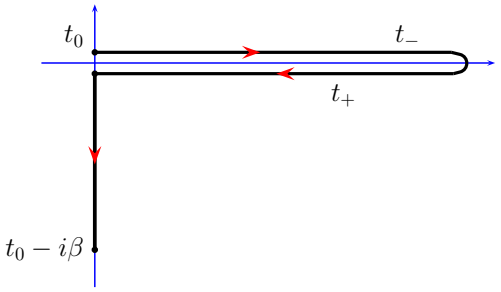

FIGURE 5.2: Keldysh contour $\mathcal{C}$. Times on the upper/lower branch are specified with the subscript $\mp$.

the device) or $\hat{c}$ (for the leads) in the Heisenberg representation

$$\hat{\psi}_H(1) = \hat{U}(t_0, z_1)\hat{\psi}_{i_1\sigma_1}\hat{U}(z_1, t_0). \tag{5.25}$$

We here use the compact notation with collective indices $1 = (i_1, \sigma_1, z_1)$ and $2 = (i_2, \sigma_2, z_2)$ for the site, spin and contour variable (z_1 and z_2 specify the position on the contour) respectively. The Green function of Eq. 5.24 is anti-periodic along the contour since

$$G(1,2)|_{z_1=t_0} = -G(1,2)|_{z_1=t_0-i\beta} \tag{5.26}$$

and similarly for variable 2. These exact relations provide the boundary conditions to solve the equation of motion along the contour

$$\begin{aligned} i\partial_{z_1}G(1,2) - \int_{\mathcal{C}} \mathrm{d}z_3 \, [h(1,3) + \Sigma_{\mathrm{MB}}(1,3)]\, G(3,2) \\ = \delta(1,2), \end{aligned} \tag{5.27}$$

where

$$\begin{aligned} h(1,3) &= \delta(z_1, z_3)h_{i_1\sigma_1, i_3\sigma_3}(z_1) \\ &= \delta(z_1, z_3)\langle 0|\hat{\psi}_{i_1\sigma_1}\hat{H}(z_1)\hat{\psi}^\dagger_{i_3\sigma_3}|0\rangle \end{aligned} \tag{5.28}$$

is the one-body part of the full Hamiltonian whereas Σ_{MB} is the many-body self-energy. In practice, of course, the self-energy Σ_{MB} has to be approximated. We consider only approximations that preserve basic conservation laws like the continuity equation or the conservation of the total energy. In this case $\Sigma_{\mathrm{MB}} = \Sigma_{\mathrm{MB}}[G]$ is a functional of the Green function and can be written as the functional derivative of the Baym functional $\Phi[G]$

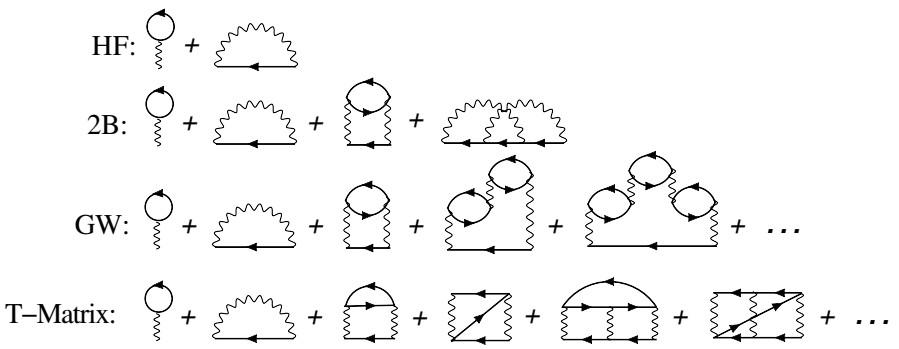

FIGURE 5.3: Diagrammatic representation of the conserving many-body approximations to the self-energy. Wiggly lines denote the many-body interaction. All Green function lines (directed solid lines) are are fully dressed.

[57], i.e.,

$$\Sigma_{\mathrm{MB}}[G](1,2) = \frac{\delta\Phi[G]}{\delta G(2,1)} \,. \tag{5.29}$$

Any functional $\Phi[G]$ that is an arbitrary linear combination of vacuum diagrams with fermionic lines G yields a conserving approximation to the at the level of the Hartree-Fock (HF), second Born (2B), GW and T-matrix; their diagrammatic representations are illustrated in Fig 5.3. Note that the equation of motion of the Keldysh Green function is solved fully self-consistently. The self-consistent HF approximation is time-local and includes the Hartree and the exchange potential. The self-consistent 2B approximation consists of the two diagrams to second order in the interaction [58]. It describes dynamical screening of the electron-electron interaction via a simple bubble diagram and includes a vertex contribution via the second order exchange diagram. The fully self-consistent GW approximation [59] incorporates the dynamical screening effects via the infinite summation of bubble diagrams [60]. In this approximation, the Coulomb interaction is replaced by the screened potential W. The last approximation we use is the fully self-consistent T-matrix approximation [45, 50]. It contains the 2B diagrams and an infinite summation of the ladder diagrams. The GW and T-matrix approximations are complementary since the GW approximation accounts for dynamical screening in infinite systems with long-range Coulombic interactions whereas the T-matrix approximation is known to be important in describing infinite systems with a short range hard-core interaction [50, 61].

As in the TDDFT case, discussed in the previous section, also in the context of MBPT applied to transport we deal with the problem of a finite open system attached to semi-infinite leads. Again, this can be achieved by using an embedding self-energy. Since

in our model the interaction is restricted to the central device only, the many-body self-energy depends only on the central block of the Green function $\mathbf{G}_{CC}$ and is itself a matrix with the following block structure

$$\mathbf{\Sigma}_{\rm MB}[\mathbf{G}] = \begin{pmatrix} 0 & 0 & 0 \\ 0 & \mathbf{\Sigma}_{\rm MB}[\mathbf{G}_{CC}] & 0 \\ 0 & 0 & 0 \end{pmatrix}. \tag{5.30}$$

The equation of motion (5.27) can be transformed into an equation in the device region only by embedding the leads

$$\begin{aligned}[i\partial_z - \mathbf{H}_{CC}(z)]\,\mathbf{G}_{CC}(z,z') &= \delta(z,z') \\ &+ \int_{\mathcal{C}} \mathrm{d}\bar{z}\ [\mathbf{\Sigma}_{\rm em}(z,\bar{z}) + \mathbf{\Sigma}_{\rm MB}(z,\bar{z})]\,\mathbf{G}_{CC}(\bar{z},z')\,. \end{aligned} \tag{5.31}$$

The presence of the leads is described in an exact way by the embedding self-energy

$$\mathbf{\Sigma}_{\rm em}(z,z') = \sum_{\alpha=L,R} \mathbf{H}_{C\alpha}\mathbf{g}_{\alpha\alpha}(z,z')\mathbf{H}_{\alpha C}, \tag{5.32}$$

which accounts for virtual processes where an electron in the device hops onto the leads at time z' and then hops back onto the device at time z. The quantity $\mathbf{g}_{\alpha\alpha}(z,z')$ is therefore the Green function of the isolated semi-infinite lead α and satisfies the equation of motion

$$[i\partial_z - \mathbf{H}_{\alpha\alpha}(z)]\,\mathbf{g}_{\alpha\alpha}(z,z') = \delta(z,z'). \tag{5.33}$$

The technique to propagate the equation of motion (5.31) is described in detail in Ref. [52].

For the time-dependent observable calculated on the real axis we denote the contour parameter z by the real time t. The time-dependent density is given by Eq. 5.10.
The current through the lead $\alpha = L, R$ can be expressed in terms of the so-called Keldysh Green functions as [48, 49]

$$\begin{aligned} I_\alpha(t) &= 2\mathrm{Re}\Big\{ \int_{t_0}^{t} d\bar{t}[\mathbf{G}^{<}_{CC}(t,\bar{t})\Sigma^{\rm A}_{{\rm em},\alpha}(\bar{t},t) \\ &+ \int_{t_0}^{t} d\bar{t}\mathbf{G}^{\rm R}_{CC}(t,\bar{t})\Sigma^{<}_{{\rm em},\alpha}(\bar{t},t)] \\ &-i \int_{0}^{\beta} d\bar{\tau}\mathbf{G}^{\rceil}_{CC}(t,\bar{\tau})\Sigma^{\lceil}_{{\rm em},\alpha}(\bar{\tau},t)\Big\}, \end{aligned} \tag{5.34}$$

where we integrated on the Keldysh contour and where the superscripts A, R and $<$ refer to the advanced, retarded, and lesser components of the Green function and the self-energy. Further, $\rceil$ and $\lceil$ are the mixed components having one time argument on the imaginary axis and another on the real axis [49, 52]. The initial many-body correlations and embedding effects are taken into account by the last term in Eq. 5.34 which is an integral over the vertical track of the Keldysh contour [62]. If we assume that in the $t \to \infty$ limit the terms with components on the imaginary track vanish and that the Green function and the self-energy depend only on $t - t'$ then we can Fourier transform Eq. 5.34 and we obtain the Meir-Wingreen formula for the steady-state current [36]

$$I_\alpha^\infty = -i \int_{-\infty}^{\infty} \frac{d\omega}{\pi} \Gamma_\alpha(\omega) \Big[\mathbf{G}^<_{CC}(\omega) - 2i\pi f_\alpha(\omega) A(\omega) \Big] \tag{5.35}$$

where $\Gamma_\alpha(\omega)$ is the imaginary part of the embedding self-energy, $f_\alpha(\omega)$ is the Fermi function and $A(\omega)$ is the steady-state spectral function [36]. Hence, Eq. 5.34 is a generalization of the Meir-Wingreen formula [49].

We further define the nonequilibrium spectral function

$$A(T, \omega) = -\mathrm{Im}\,\mathrm{Tr}_C \int \frac{\mathrm{d}\tau}{\pi} e^{i\omega\tau} \big[\mathbf{G}^> - \mathbf{G}^< \big] (T + \frac{\tau}{2}, T - \frac{\tau}{2}), \tag{5.36}$$

where $\tau = t - t'$ is a relative time and $T = (t + t')/2$ is an average time-coordinate [63]. In equilibrium, this function is independent of T and has peaks below the Fermi level at the electron removal energies of the system, while above the Fermi level it has peaks at the electron addition energies. If the system reaches a steady state after some switching time, then also the spectral function becomes independent of T after some transient period and has peaks at the addition and removal energies of the biased system [64]. The Kadanoff-Baym equations have recently been implemented for closed systems such as atoms [51] or finite Hubbard clusters [65] while the extension to the transport problem has been given in Refs. [48, 49]. In Ref. [65] it has been noted that in *finite* systems the Kadanoff-Baym dynamics suffer from an artificial damping due to the specific selection of the diagrams in $\mathbf{\Sigma}_{\mathrm{MB}}$. In open systems, however, this artificial damping is hopefully negligible with respect to the physical damping induced by the coupling of the discrete energy levels of the device with the energy continua of the leads. However, one expects that for weakly coupled devices this unphysical effect will be more consequential .

5.3 Steady state Condition for the Density

Following the time evolution of the system as it is driven out of equilibrium by applying a bias in the leads, will tell us if and how the system eventually reaches a steady state. If, instead, we *assume* that the system eventually approaches a steady state in the limit $t \to \infty$, then an equation determining the steady-state density $n_j^\infty := \lim_{t\to\infty} n_j(t)$ can be obtained from Eq. 5.11, using the fact that in the steady state the Green function depends only on the relative time coordinate $t - t'$. Fourier transformation with respect to this variable leads to

$$n_j^\infty = \int \frac{\mathrm{d}\omega}{\pi i} \left[\mathbf{G}^<_{CC}(\omega)\right]_{jj} \tag{5.37}$$

where $\mathbf{G}^<_{CC}(\omega)$ can be obtained from[29]

$$\mathbf{G}^<_{CC}(\omega) = \mathbf{G}^R_{CC}(\omega)\mathbf{\Sigma}^<_{\mathrm{tot}}(\omega)\mathbf{G}^A_{CC}(\omega) \tag{5.38}$$

and

$$\mathbf{\Sigma}^<_{\mathrm{tot}}(\omega) = \mathbf{\Sigma}^<_{\mathrm{em}}(\omega) + \mathbf{\Sigma}^<_{\mathrm{MB}}(\omega) \tag{5.39}$$

is the total self-energy which consists of the embedding and the many-body contribution. The advanced and retarded Green functions are related via $\mathbf{G}^A_{CC} = [\mathbf{G}^R_{CC}]^\dagger$ and the latter is given by

$$\mathbf{G}^R_{CC}(\omega) = \left(\omega \mathbb{1}_{CC} - \mathbf{H}^\infty_{CC} - \mathbf{\Sigma}^R_{\mathrm{tot}}(\omega)\right)^{-1} \tag{5.40}$$

where $\mathbb{1}_{CC}$ is the unit matrix in the device region and

$$\mathbf{H}^\infty_{CC} := \lim_{t\to\infty} \mathbf{H}_{CC}(t). \tag{5.41}$$

For the 1D tight-binding leads the retarded embedding self-energy is given by

$$[\mathbf{\Sigma}^R_{\mathrm{em}}(\omega)]_{ij} = \Sigma^R_{\mathrm{em},L}(\omega)\delta_{i,1}\delta_{j,1} + \Sigma^R_{\mathrm{em},R}(\omega)\delta_{i,N_c}\delta_{j,N_c} \tag{5.42}$$

where

$$\begin{aligned}\Sigma^R_{\mathrm{em},\alpha}(\omega) &= \Lambda_\alpha(\omega) - \frac{i}{2}\Gamma_\alpha(\omega) \\ &= \frac{V^2_{\mathrm{link}}}{2V^2_\alpha}\begin{cases} \omega_\alpha - \sqrt{\omega^2_\alpha - 4V^2_\alpha} & \omega_\alpha > 2V_\alpha \\ \omega_\alpha + \sqrt{\omega^2_\alpha - 4V^2_\alpha} & \omega_\alpha < -2V_\alpha \\ \omega_\alpha - i\sqrt{4V^2_\alpha - \omega^2_\alpha} & |\omega_\alpha| \leq 2V_\alpha \end{cases} .\end{aligned} \tag{5.43}$$

Here, $\omega_\alpha = \omega - \varepsilon^\alpha - W^\infty_\alpha$ where $W^\infty_\alpha = \lim_{t\to\infty} W_\alpha(t)$ is the long-time limit of the applied bias. The lesser component of the embedding self-energy is

$$[\mathbf{\Sigma}^<_{\mathrm{em}}(\omega)]_{ij} = \Sigma^<_{\mathrm{em},L}(\omega)\delta_{i,1}\delta_{j,1} + \Sigma^<_{\mathrm{em},R}(\omega)\delta_{i,N_c}\delta_{j,N_c} \tag{5.44}$$

where

$$\Sigma^<_{\mathrm{em},\alpha}(\omega) = if(\omega)\Gamma_\alpha(\omega) , \tag{5.45}$$

$f(\omega) = (1 + \exp(\beta(\omega - \mu)))^{-1}$ is the Fermi distribution function and Γ_α is defined by Eq. 5.43.

When using TDDFT, where all many-body interaction effects appear in v_{xc}, the self-consistency condition for the density n^∞_j, simplifies as we will see in the following. In the adiabatic approximation, the retarded KS Green function is given by

$$\mathbf{G}^{\mathrm{KS},R}_{CC}(\omega) = \left(\omega\mathbb{1} - \mathbf{H}^{\mathrm{KS},\infty}_{CC}[n^\infty] - \mathbf{\Sigma}^R_{\mathrm{em}}(\omega)\right)^{-1} \tag{5.46}$$

where

$$\mathbf{H}^{\mathrm{KS},\infty}_{CC}[n^\infty] := \lim_{t\to\infty} \mathbf{H}^{\mathrm{KS}}_{CC}(t) \tag{5.47}$$

is the asymptotic value of the KS Hamiltonian and we have emphasized in the notation that the latter depends on the steady-state density n^∞. The KS lesser Green function then is

$$\mathbf{G}^{\mathrm{KS},<}_{CC}(\omega) = \mathbf{G}^{\mathrm{KS},R}_{CC}(\omega)\mathbf{\Sigma}^<_{\mathrm{em}}(\omega)\mathbf{G}^{\mathrm{KS},A}_{CC}(\omega) \tag{5.48}$$

and the self-consistency condition for the steady-state density becomes

$$\begin{aligned} n^\infty_j &= \int \frac{\mathrm{d}\omega}{\pi}\Big(f_L(\omega)\Gamma_L(\omega)|[\mathbf{G}^{\mathrm{KS},R}_{CC}(\omega)]_{1,j}|^2 \\ &\quad + f_R(\omega)\Gamma_R(\omega)|[\mathbf{G}^{\mathrm{KS},R}_{CC}(\omega)]_{N_c,j}|^2\Big) , \end{aligned} \tag{5.49}$$

with the shifted Fermi function $f_\alpha(\omega) = f(\omega - W^\infty_\alpha)$. Since the KS Green function $\mathbf{G}^{\mathrm{KS},R}_{CC}$ (Eq. 5.46) depends on n^∞ (through $\mathbf{H}^{\mathrm{KS},\infty}_{CC}[n^\infty]$), Eq. 5.49 becomes a set of N_c

coupled, non-linear equations for the steady state density n_j^∞, $j = 1, \ldots, N_c$ at the N_c sites of the interacting device region. These equations are non-linear and it is therefore possible that they have more than one solution.

It is important to note that a closed set of equations for n_j^∞ is obtained only for adiabatic approximations of the time-dependent XC potential. For approximations with memory, $\mathbf{H}_{CC}^{\mathrm{KS},\infty}$ (and hence $\mathbf{G}_{CC}^{\mathrm{KS},R}$) depends on the whole time evolution, n(t), of the density. Consequently, the right-hand side of Eq. 5.49 is not simply a function of n^∞ for non-adiabatic XC functionals. This is similar to the case of MBPT, where the steady state self-consistency condition for the density requires knowledge of the central block of the Green function $\mathbf{G}_{CC}(\omega)$ (to compute the many-body self-energy $\mathbf{\Sigma}_{\mathrm{MB}}[\mathbf{G}_{CC}]$) and thus the equations are not closed. One can, however, deduce a steady-state equation for the whole Green function $\mathbf{G}_{CC}(\omega)$ which can be solved by an interative procedure, like in Ref. [66]. In this case, due to the non-linear nature of the steady-state equation for $\mathbf{G}_{CC}(\omega)$, different initial guesses for the Green function may lead to the convergence to more than one self-consistent solution.

Chapter 6

Dynamical Coulomb Blockade and the Derivative Discontinuity of Time-Dependent Density Functional Theory

In this chapter we investigate the role of the discontinuity of the exchange-correlation potential of density functional theory for the problem of electron transport and show it is intimately related to the Coulomb blockade phenomenon. Coulomb blockade [67] is one of the true hallmarks of electron-electron interactions in molecular transport. In essence, Coulomb blockade is due to an electrostatic barrier induced by the electrons in the device which, for a range of bias values, prevents further electrons from tunneling in [68], until the bias is sufficiently increased to supply the necessary charging energy of the device.

In the conventional static picture of Coulomb blockade it is particularly important to ensure the *charge quantization* of the device. In general, this is valid in the limit of very week coupling to the leads. To guarantee this in a DFT calculation, the exchange-correlation potential must exhibit the so-called derivative discontinuity, i.e., the XC potential jumps by a constant when the number of electrons on the quantum dot passes through an integer.

Progress in the theoretical description and experimental manipulation of the Coulomb blockade effect is expected to foster advances in nanoelectronics and quantum information technologies [69, 70]. Thus, a great deal of experiments are currently devoted to

accurate fabrication of lead-molecule setups and inherent transport measurements in the Coulomb blockade regime. Here, considerable progress has been made [71, 72]. On the theoretical side the situation is less satisfactory. The so-called constant interaction model [73] explains the Coulomb blockade phenomenon in a rather simplistic way by associating a capacitance C to the central region, consisting of the device (e.g. a quantum dot) and the tunneling barriers. Hence, the electrostatic energy of a charge $q = eN$ sitting on the dot is given by $\frac{q^2}{C}$. To bring in an extra electron to the quantum dot the bias voltage W has to increase by $\frac{q}{C}$ (plus the N and $N+1$ energy level difference), to overcome the Coulomb repulsion due to the charge already present in the dot [74]. For all bias voltages below this limit, no current flows and the access to the dot is blocked due to the Coulomb repulsion caused by the filled N-electron level, until the bias increases enough such that the value of the chemical potential of one of the lead and the empty $N+1$ level line up and another electron can tunnel in.
Although many aspects of Coulomb blockade can be understood by the constant interaction model, it is clear that, to achieve quantitative accuracy in real systems, an *ab initio* description is required, something which has not been accomplished so far. In fact, as mentioned in the previous chapters, most current *ab initio* treatments of transport are limited to the steady-state regime and based on the Landauer formalism combined with DFT [17, 20, 23, 24]. Within this prescription (L+DFT), the agreement with experiment is often poor, particularly for devices weakly coupled to leads. As a possible reason for its failure, the shortcomings of typical exchange-correlation functionals of static DFT [75] have been identified, such as, the lack of a derivative discontinuity in popular Local Density Approximations and Generalized Gradient Approximations [76, 77].

As transport is an intrinsically non-equilibrium phenomenon, the scientific community has progressively shifted to time-dependent approaches in recent years (see, e.g., Refs. [48, 49, 78–84]). This shift also recognizes the fact that significant novel physics occurs in the time domain.

It is then quite natural, at this stage, to address the phenomenon of Coulomb blockade with TDDFT. This immediately raises the following questions: i) what is the connection between a TDDFT description of Coulomb blockade in real time and the one of standard steady-state approaches? ii) which features an approximate XC functional needs to have to be able to describe Coulomb blockade ?

In this Chapter these basic questions are addressed. We present here a TDDFT study of Coulomb blockade in the time domain for a correlated single-level quantum dot weakly coupled to leads. We use the XC functional [85], introduced in Chapter 5, exhibiting the proper derivative discontinuity and find that *the assumption that the system evolves towards a steady state is not justified* in this case. The discontinuity of the potential leads to self-sustained oscillations induced by electron correlations, with history-dependent frequencies and amplitudes. Our results thus reveal dynamical aspects of Coulomb blockade which are not accessible by traditional steady-state approaches. In the following section we discuss the origin and importance of the derivative discontinuity in the DFT approach.

6.1 Derivative Discontinuity of DFT

To gain some insight into the origin of the derivative discontinuity in DFT let us first define a few basic terms and concepts:
The particle-removal energy of an N particle quantum system

$$E_r := E(N-1) - E(N) = I(N), \tag{6.1}$$

and the particle-addition energy of an N particle quantum system

$$E_a := E(N) - E(N+1) = A(N). \tag{6.2}$$

Here, $E(N)$ denotes the many-body groundstate energy of the N particle system (the external potential is kept fixed). In the context of finite systems, E_r and E_a are the ionization energy $I(N)$ and electron affinity $A(N)$, respectively. Note that $A(N)$ can be viewed as the ionization energy of the $N+1$ particle system, i.e., $A(N) = I(N+1)$.

The difference between the particle-removal and addition energy is called fundamental gap

$$\begin{aligned} \Delta &:= E_r - E_a \\ &= E(N+1) - 2E(N) + E(N-1). \end{aligned} \tag{6.3}$$

For the case of truly non-interacting system, for instance, the difference $E_r - E_a$ is

$$\begin{aligned}\Delta_{\text{nonint}} &:= E_r - E_a \\ &= (E^{\text{nonint}}(N-1) - E^{\text{nonint}}(N)) - (E^{\text{nonint}}(N) - E^{\text{nonint}}(N+1)) \\ &= \epsilon^{\text{nonint}}_{N+1}(N) - \epsilon^{\text{nonint}}_{N}(N),\end{aligned} \tag{6.4}$$

where $\epsilon^{\text{nonint}}_{M}(N)$ denotes the M^{th} single-particle energy level of the N particle system. Returning to the interacting case, it is well known within DFT that the KS energy eigenvalues have no physical meaning, except for the the highest occupied eigenvalue, whose negative is the ionization energy of the interacting system:

$$I(N) = -\epsilon^{\text{KS}}_{N}(N) = -\epsilon^{\text{KS}}_{HO}(N). \tag{6.5}$$

Given the fact that $A(N) = I(N+1)$ we conclude that

$$A(N) = I(N+1) = -\epsilon^{\text{KS}}_{N+1}(N+1) = -\epsilon^{\text{KS}}_{HO}(N+1) \tag{6.6}$$

where $\epsilon^{\text{KS}}_{N+1}(N+1)$ is the highest occupied energy of a KS system with $N+1$ particles exposed to a KS potential that reproduce the density of the interacting $N+1$ particles system.

From Eq. 6.5 and Eq. 6.6 it can readily be seen that:

$$\begin{aligned}\Delta &= I(N) - A(N) \\ &= \epsilon^{\text{KS}}_{N+1}(N+1) - \epsilon^{\text{KS}}_{N}(N).\end{aligned} \tag{6.7}$$

Thus, the fundamental gap in DFT is the difference between the HO energy of an $N+1$ particles KS system and the HO energy of an N particles KS system. It is important to note that, conceptually there is a difference between the fundamental gap (given in Eq. 6.7) and the so-called Kohn-Sham gap, Δ_{KS}, which is defined analougous to Δ_{nonint} as

$$\Delta_{\text{KS}} = \epsilon^{\text{KS}}_{N+1}(N) - \epsilon^{\text{KS}}_{N}(N). \tag{6.8}$$

The Kohn-Sham gap is the difference between the lowest unoccupied (LU) energy of a KS system with N particles and the HO energy of the same KS system (with N particles). The difference between the fundamental gap and the Kohn-Sham gap is called derivative discontinuity and is given by $\Delta_{\text{XC}} = \Delta - \Delta_{\text{KS}} = \epsilon^{\text{KS}}_{N+1}(N+1) - \epsilon^{\text{KS}}_{N+1}(N)$. In the following, we show that this consept can also be expressed in terms of the energy functionals.

In standard DFT, the number of electrons N is a fixed and integer value and the density

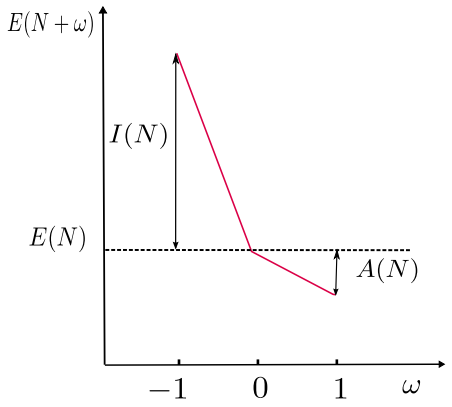

FIGURE 6.1: Groundstate energy of an ensemble of $M = N + \omega$ electrons

functionals are defined in the domain of densities that integrate to N. By extending DFT to ensemble DFT, whose number of electrons is a fractional number, the fundamental gap can be rewritten in terms of derivative discontinuities of the total energy functional. To develop a density functional theory for fractional particle number, wavefunctions with different electron numbers are included in the same ensemble. The ensemble expectation value of an operator $\hat{O}$ (of a system with a fractional particle number $M = N + \omega$) is defined as

$$\langle \hat{O} \rangle := \mathrm{Tr}\left\{\hat{D}\hat{O}\right\}, \tag{6.9}$$

with $\hat{D}$ being

$$\hat{D} = (1-\omega)|\Psi_N\rangle\langle\Psi_N| + \omega|\Psi_{N+1}\rangle\langle\Psi_{N+1}|. \tag{6.10}$$

Hence, the ensemble density $n(\boldsymbol{r})$ is given by

$$n(\boldsymbol{r}) = \mathrm{Tr}\left\{\hat{D}\hat{n}\right\} = (1-\omega)\langle\Psi_N|\hat{n}(\boldsymbol{r})|\Psi_N\rangle + \omega\langle\Psi_{N+1}|\hat{n}(\boldsymbol{r})|\Psi_{N+1}\rangle, \tag{6.11}$$

which integrates over all space to $M = N+\omega$ with $(0 \leq \omega \leq 1)$. In addition the ensemble groundstate energy is

$$\begin{aligned} E_M = \mathrm{Tr}\left\{\hat{D}\hat{H}\right\} &= (1-\omega)E(N) + \omega E(N+1) \\ &= \omega(E(N+1) - E(N)) + E(N) \end{aligned} \tag{6.12}$$

From Eq. 6.12, it is clear that the groundstate energy E_M as a function of the particle number M consists of straight line segments with possible derivative discontinuities at integer N (see Fig 6.1). Therefore, the chemical potential $\mu(M) = \frac{\partial E_M}{\partial M}$ changes

discontinuously at N

$$\mu(M) = \frac{\partial E_M}{\partial M} = \begin{cases} E(N) - E(N-1) & N-1 < M < N \\ E(N+1) - E(N) & N < M < N+1 \end{cases}$$
$$= \begin{cases} -I(N) & N-1 < M < N \\ -A(N) & N < M < N+1. \end{cases} \tag{6.13}$$

As a consequence, the fundamental gap can be rewritten as

$$\Delta = -\lim_{\omega \to 0} \mu(N-\omega) + \lim_{\omega \to 0} \mu(N+\omega). \tag{6.14}$$

Using ensemble Hohenberg-Kohn variational principle

$$\left.\frac{\delta E[n]}{\delta n}\right|_{n_M} = \mu(M), \tag{6.15}$$

the fundamental gap is rigorously given by

$$\begin{aligned} \Delta &= \lim_{\omega \to 0} \left\{ \left.\frac{\delta E[n]}{\delta n}\right|_{N+\omega} - \left.\frac{\delta E[n]}{\delta n}\right|_{N-\omega} \right\} \\ &= \lim_{\omega \to 0} \left\{ \left.\frac{\delta T_s[n]}{\delta n}\right|_{N+\omega} - \left.\frac{\delta T_s[n]}{\delta n}\right|_{N-\omega} \right\} \\ &+ \lim_{\omega \to 0} \left\{ \left.\frac{\delta E_{\mathrm{xc}}[n]}{\delta n}\right|_{N+\omega} - \left.\frac{\delta E_{\mathrm{xc}}[n]}{\delta n}\right|_{N-\omega} \right\} \\ &= \Delta_{\mathrm{KS}} + \Delta_{\mathrm{xc}}. \end{aligned} \tag{6.16}$$

In Eq. 6.16, we have used the fact that the Hartree and the external potential energy are explicit and continuous functionals of the density, and as a consequence the derivative discontinuity must come from the kinetic and the exchange-correlation part of the total energy. The derivative discontinuity of the kinetic energy is the discontinuity of a non-interacting system of N particles exposed to some external potential (which is the Kohn-Sham potential, if the derivatives are calculated at the density of the N particle interacting system) and therefore $\Delta_{\mathrm{KS}} = \epsilon^{\mathrm{KS}}_{N+1}(N) - \epsilon^{\mathrm{KS}}_{N}(N)$.
The exchange-correlation discontinuity $\Delta_{\mathrm{xc}} = v^{>}_{\mathrm{xc}} - v^{<}_{\mathrm{xc}}$ where $v^{\gtrless}_{\mathrm{xc}} = \left.\frac{\delta E_{\mathrm{xc}}[n]}{\delta n}\right|_{N\pm\omega}$, known as derivative discontinuity in DFT, has to be added to the KS single-particle gap. The discontinuity of the XC potential is essential to capture the Coulomb blockade phenomenon in quantum dots within the framework of DFT [77]. In quantum dots, the energy gap is traditionally also decomposed into two contributions:
1) The single-particle contribution , $\Delta\epsilon$, describing the effects of quantized energy levels

due to geometry and confinement.

2) The charging energy raising the energy gap discontinuously upon addition of one more electron due to many-body effects.

The later contribution is typically described phenomenologically, by a classical capacitance C and thus the charging energy is given by $\frac{q^2}{C}$. Both decompositions of the full gap must add up to the same value, so that $\Delta_{\mathrm{KS}} + \Delta_{\mathrm{xc}} = \Delta\epsilon + \frac{q^2}{C}$. In the phenomenological approach, no general microscopic expressions for $\Delta\epsilon$ and $\frac{q^2}{C}$ are given. If $\Delta\epsilon$ is calculated from eigenvalues of noninteracting particles, subject to the confining potentials only, then $\frac{q^2}{C}$ accounts for all many-body effects. Therefore DFT suggests an alternative identification of $\Delta\epsilon$ with the Kohn-Sham gap, and $\frac{q^2}{C}$ with the derivative discontinuity.

6.2 The System and its Time Evolution

To investigate the role of the derivative discontinuity of the exchange-correlation potential in Coulomb blockade, we study a single-level quantum dot coupled weakly to two semi-infinite, non-interacting 1D leads. The Hamiltonian of this system is similar to the one given in Eq. 5.1 and schematically shown in Fig 6.2.

The Hamiltonian of the central region for the single quantum dot (QD) reads

$$\hat{H}_C = \hat{H}_{\mathrm{QD}} = v_{\mathrm{g}} \sum_{\sigma} \hat{n}_{0\sigma} + U \hat{n}_{0\uparrow} \hat{n}_{0\downarrow} \tag{6.17}$$

with $\hat{n}_{0\sigma} = \hat{c}^{\dagger}_{0\sigma} \hat{c}_{0\sigma}$ the density for electrons with spin σ. The dot is characterized by two parameters: the on-site Coulomb repulsion U and a gate voltage v_{g}. For times $t \leq 0$, the system is in equilibrium; at $t > 0$, a bias $W_{\alpha}(t)$ is applied.

Within TDDFT, the KS dynamics produces the exact TD density, provided we know the exact KS potential *whose density dependence* is non-local in space and time. In practice, one has to resort to approximations. However, as shown below, we can already gain significant insight via an approximate, adiabatic KS potential. Here we use the modified BALDA functional, based on an LDA functional for the uniform 1D Hubbard model BALDA [85], which was explained in detail in Chapter 5.

In the context of TDDFT, an adiabatic version of BALDA, which we call ABALDA, had already been used to investigate the dynamics of Hubbard clusters [86].

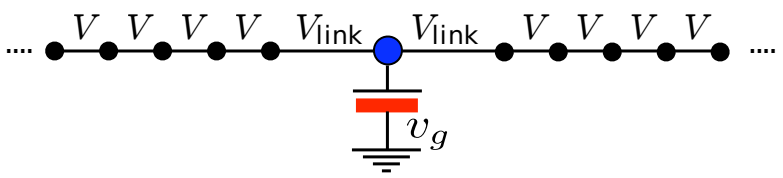

FIGURE 6.2: Schematic picture of the system

Within the ABALDA, the KS Hamiltonian reads $\hat{H}_{\rm KS}(t) = \hat{H}_{\rm QD,KS}(t) + \sum_{\alpha=L,R} \hat{H}_\alpha(t) + \hat{H}_T$, with

$$\hat{H}_{\rm QD,KS}(t) = \sum_\sigma v_{\rm KS}(n_0(t))\hat{n}_{0\sigma}, \tag{6.18}$$

and the KS potential is a function of the instantaneous density $n_0(t) = \sum_\sigma n_{0\sigma}(t)$ on the quantum dot. Explicitly,

$$\begin{aligned} v_{\rm KS}(n_0(t)) &= v_{\rm ext} + v_H(n_0(t)) + v_{\rm xc}(n_0(t)) \\ &= v_{\rm g} + \frac{1}{2}Un_0(t) + v_{\rm xc}(n_0(t)). \end{aligned} \tag{6.19}$$

In the Coulomb blockade regime, the electrons need to be largely localized in the device. For our model system, this corresponds to i) taking a dot-lead hopping $V_{\rm link}$ significantly smaller than the hopping V in the leads and ii) using $U/V_{\rm link}$ as relevant parameter in the BALDA functional. Thus, as discussed in Chapter 5, the following functional form is used:

$$v_{\rm xc}(n) = \theta(1-n)v_{\rm xc}^{(<)}(n) - \theta(n-1)v_{\rm xc}^{(<)}(2-n), \tag{6.20}$$

$$v_{\rm xc}^{(<)}(n) = -\frac{1}{2}Un - 2V_{\rm link}\left[\cos\left(\frac{\pi n}{2}\right) - \cos\left(\frac{\pi n}{\xi}\right)\right], \tag{6.21}$$

where the parameter ξ is determined by the condition

$$\frac{2\xi}{\pi}\sin(\pi/\xi) = 4\int_0^\infty {\rm d}x\, \frac{J_0(x)J_1(x)}{x[1+\exp(Ux/(2V_{\rm link}))]} \tag{6.22}$$

with $J_{i=0,1}(x)$ Bessel functions.

In the limit of very weak coupling

$$\lim_{V_{\rm link}\to 0} v_{\rm xc}(n) = -\theta(1-n)Un/2 + \theta(n-1)U(2-n)/2, \tag{6.23}$$

which correctly reproduces the exact XC potential of an isolated single level quantum dot. Therefore this is the limit where the BALDA becomes exact.

For finite coupling the discontinuity of $v_{\rm xc}(n)$ at half-filling is :

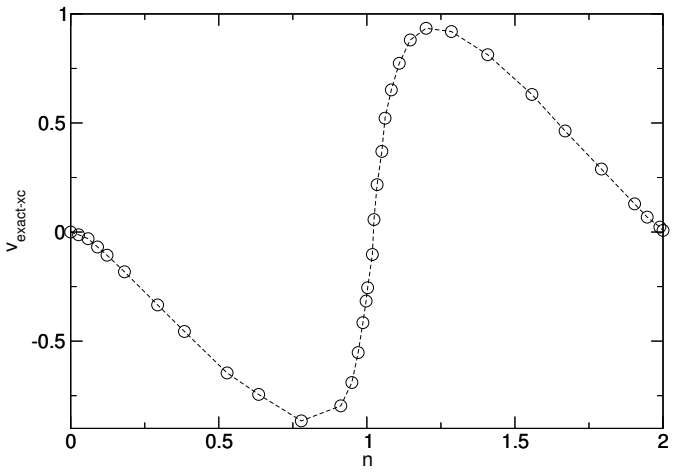

FIGURE 6.3: The exact exchange-correlation functional for a correlated quantum dot in small a cluster with five sites on its left and six sites on its right. The hopping between the impurity and its neighboring site V_{link} is 0.3 and elsewhere $V = 1$, the charging energy of the impurity $U = 2$ and $\epsilon_F = 1.5$.

$$\Delta_{\text{xc}} = v_{\text{xc}}[1^+] - v_{\text{xc}}[1^-] = U - 4V_{\text{link}}\cos(\frac{\pi}{\xi}), \tag{6.24}$$

It is worth noting that the discontinuity at half filling in the limit of very week coupling ($V_{\text{link}} \to 0$) reduces to U which is the charging energy required to move a second electron on an isolated quantum single level dot already charged by one electron.

In addition, as the discontinuity of the XC potential for our model (and also for the uniform one-dimensional Hubbard model) matches the fundamental gap, it must be always positive. However, for the modified (original) BALDA the fundamental gap becomes negative when $U/V_{\text{link}}(U/V)$ is less than 1.735. This unphysical behavior is due to the deficiency of the BALDA functional stemming from the fact that the original BALDA functional is exact for the uniform one-dimensional Hubbard model *only* in certain limits.

The exact XC potential is certainly discontinuous for the homogeneous Hubbard model and the isolated QD. However, for the quantum dot connected to non-interacting leads, the coupling to the leads introduces some broadening in the quantum dot levels. Hence it is reasonable to expect a small smoothening of the discontinuity. This is supported by preliminary calculations of the exact v_{xc} for a system similar to the one shown in Fig 6.2, but with the left lead having five and the right lead having six non-interacting sites away from the impurity. The exact groundstate density is calculated as a function of v_{g} by exact diagonalization of the system from which the exact v_{xc} at the impurity site is obtained using reverse engineering [86] . The result as shown in Fig 6.3 suggests that the discontinuity of the XC potential is smoothened.

We therefore modified the discontinuous of $v_{\rm xc}(n)$ of Eq. 6.20 at $n = 1$, with a softened, continuous version

$$\tilde{v}_{\rm xc}(n) = f(n)v_{\rm xc}^{(<)}(n) - (1 - f(n))v_{\rm xc}^{(<)}[2 - n] \tag{6.25}$$

where

$$f(n) = \frac{1}{\exp((n-1)/a) + 1} \tag{6.26}$$

with a smoothening parameter a. The smoothening of the KS potential also has the advantage of alleviating the numerical difficulties caused by the sudden changes of $v_{\rm xc}$ during time propagation.

To propagate the lead-dot-lead KS system in time, we use an adapted version of the TD algorithm explained in Chapter 3 for an open system of effectively noninteracting electrons, as required in TDKS. In all simulations below, energies are measured in units of V, times in units of V^{-1} and currents in units of $|e|\,V$ where e is the charge of the carriers. The sharp slope near $n = 1$ in $v_{\rm xc}$ has a profound impact on the time evolution of the density on the quantum dot as well as on the current through it.

6.3 Time-dependent Transport in the Coulomb Blockade Regime

In this section we demonstrate the dynamical behavior of a system in the Coulomb blockade regime.

We consider the system in its groundstate for $t < 0$ and calculate the groundstate density self-consistently with the $v_{\rm KS}$ of Eq. 6.20 and a smoothening parameter $a = 10^{-4}$ but within static DFT where $v_{\rm KS}$ is a functional of the groundstate density. We choose $V_{\rm link} = 0.3$, $v_{\rm g} = 2$, $U = 2$, and Fermi energy $\varepsilon_{\rm F} = 1.5$. This choice of the parameters corresponds to the Coulomb blockade regime within a certain range of bias values, as we will see below. At $t = 0$, a dc bias W_L is suddenly switched on in the left lead. In Fig 6.5, we show the time evolution of the density for three different bias values $W_L = 1.3, 1.6, 1.9$. Remarkably, for this set of parameters and within a certain range of biases, *the system does not evolve towards a steady state*; instead, after a transient period, we see self-sustained density oscillations around unity (Fig 6.5). By following the time-dependent density on the quantum dot, one sees upon applying the bias, the charge density is constantly accumulating on the dot until it reaches an integer value

(n=1), at which the Kohn-Sham potential jumps up. Due to the potential increase on the quantum dot, the transition probability drops down dramatically in the Coulomb blockade regime, and as a result some charge flows back into the leads after some time. As the charge density on the dot decreases, it hits the integer value again, therefore the potential jumps back down, and the process repeats. This process is shown schematically in Fig 6.4.

The amplitude of the density oscillations is fairly small, of the order of 5×10^{-3} as

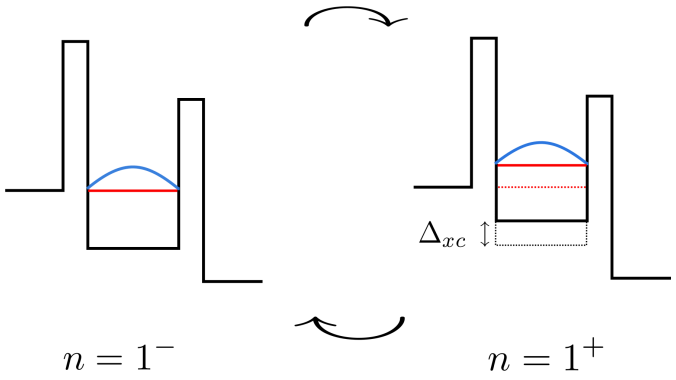

FIGURE 6.4: Schematic picture of Coulomb blockade in the time domain. If the bias voltage allows tunneling, charge accumulates continuously. But as soon as the first level is fully occupied $n_0 = 1$, and infinitesimal extra charge is injected to the system, the KS potential jumps up . This jump prevents more electrons from tunneling in and causes some of the charge to flow back into the leads after some time. As the charge density of the dot decreases, it hits the integer value again, therefore the potential jumps back down, and the process repeats.

shown in the inset of Fig 6.5. For the lower bias, $W_L = 1.3$, the density remains below unity for most of the period, for $W_L = 1.6$ the density roughly oscillates around 1, and for $W_L = 1.9$ the density exceeds unity for most of the period.

The oscillations are also present in the current (Fig 6.6) as expected, but this time with a much larger amplitude relative to its average value. The saw-tooth structure of the current oscillations is consistent with the continuity equation. The current is related to the first time-derivative of the density which, from Fig 6.6, is roughly piece-wise parabolic. Note that away from the quantum dot, the oscillations in the current (and in the density) disappear (bottom panel). Oscillations are clearly visible also in v_{KS} (Fig 6.6). Due to the fairly large jump in v_{xc} and the small amplitude of the oscillations of the density at the dot, the KS potential is a train of almost rectangular pulses. For larger biases the density remains above unity for longer times, and the width of the pulses in v_{KS} extends in time.

The rapid variation of the KS potential and the piece-wise parabolicity of the time

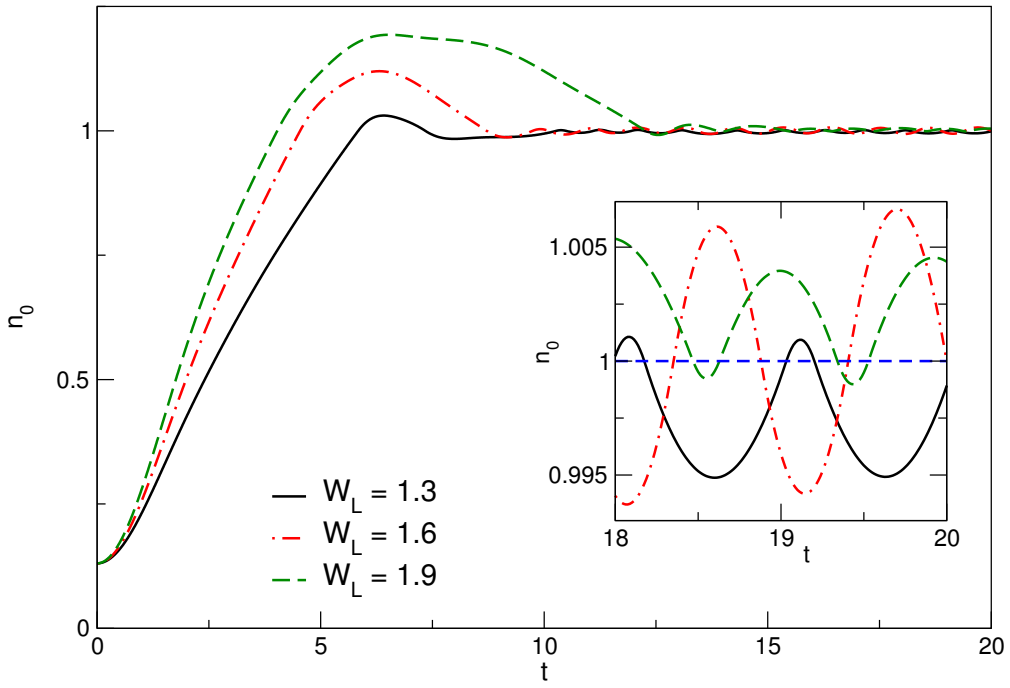

FIGURE 6.5: Time evolution of the density for three different biases. Solid, chain and dashed line refer to $W_L = 1.3$, 1.6, 1.9, respectively. The inset shows the density at the end of the propagation period.

dependent density in the long time limit suggest a simple way to understand the oscillations and the absence of a steady state. Let us denote t_1 the instant when the TD density crosses the critical value of unity from below, while t_2 ($t_2 > t_1$) is the time at which the TD density hits unity from above. After t_2 the KS potential is lowered, the electrons will be attracted to the dot and eventually the TD density crosses unity again at t_3. After a period $T = t_3 - t_1$ this process repeats. Denoting the density in the interval between t_2 and t_1 as n_+ and between t_3 and t_2 as n_- we have

$$\begin{aligned} n_+(t) &= -\frac{\alpha}{2}(t - t_1 - \sqrt{\beta/\alpha})^2 + \beta/2 + 1 \qquad t_1 \le t < t_2 \\ n_-(t) &= +\frac{\tilde{\alpha}}{2}(t - t_2 - \sqrt{\tilde{\beta}/\tilde{\alpha}})^2 - \tilde{\beta}/2 + 1 \qquad t_2 \le t < t_3 \end{aligned} \tag{6.27}$$

here $\alpha, \beta, \tilde{\alpha}, \tilde{\beta}$ are real and positive and are chosen in such a way to satisfy $n_+(t_1) = n_-(t_2) = 1$. In addition, $n_+(t_2) = n_-(t_3) = 1$ and hence we obtain $t_2 = t_1 + 2\sqrt{\beta/\alpha}$ and $t_3 = t_2 + 2\sqrt{\tilde{\beta}/\tilde{\alpha}}$ and therefore

$$T = 2\sqrt{\beta/\alpha} + 2\sqrt{\tilde{\beta}/\tilde{\alpha}} \tag{6.28}$$

Furthermore, from the derivative of density at t_2 we have, $n'_+(t_2) = n'_-(t_2)$ which lead to $\alpha\beta = \tilde{\alpha}\tilde{\beta}$. This relation together with $n'_+(t_1) = \sqrt{\beta\alpha}$, $n''_+ = -\alpha$ and $n''_- = \tilde{\alpha}$ and

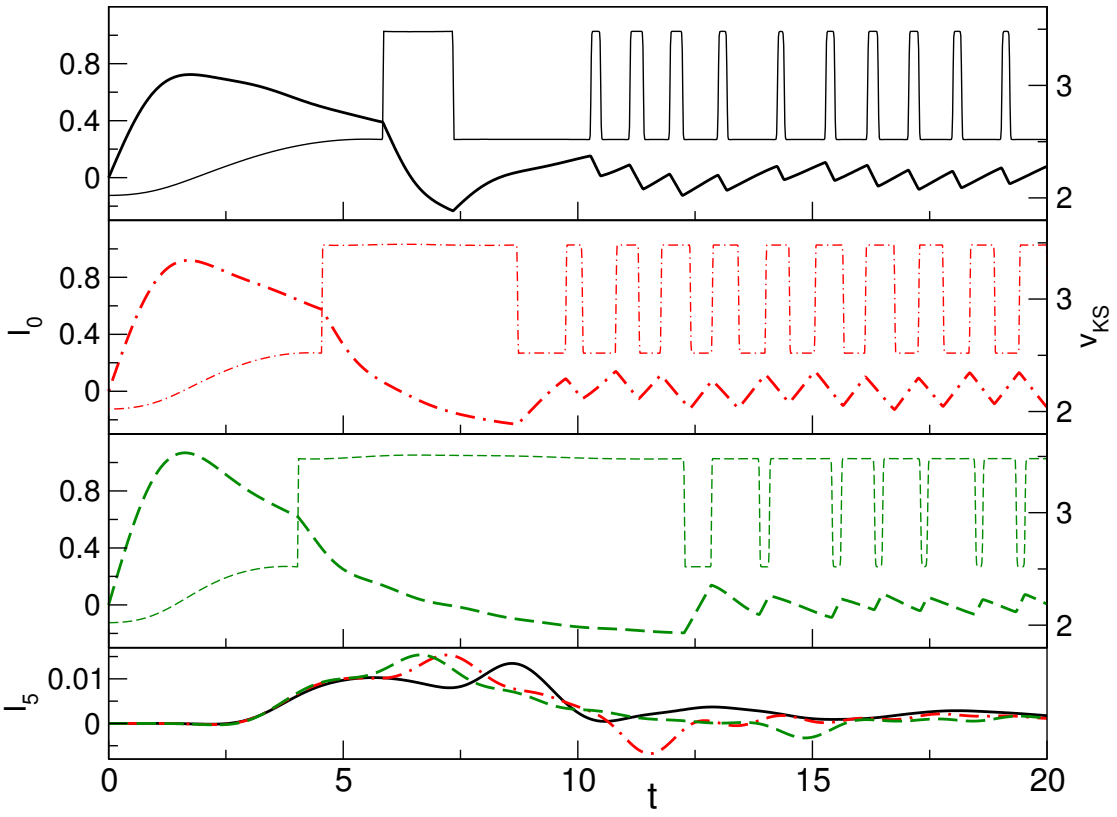

FIGURE 6.6: Time evolution of the current and KS potential for three different biases. In all panels, solid, chain and dashed line refer to $W_L = 1.3, 1.6, 1.9$, respectively. Thick lines show the current through the quantum dot while the thin ones are the KS potential. Bottom panel: current five sites away from the quantum dot.

Eq. 6.28 , give a relation for the period of oscillations in terms first and second derivative of the density

$$T = T_+ + T_- = 2n'_+(t_1)(\frac{1}{n''_-} + \frac{1}{|n''_+|}) \tag{6.29}$$

Here T_+ (T_-) is the fraction of time that the time-dependent density spend above (below) unity in one period. It is clear from Eq. 6.29 , if $|n''_+| < n''_-$, the time-dependent density is for most of the period above unity, i.e., $T_+ > T_-$ and vise versa. It should be pointed out that the time-dependent density is not *perfectly* piece-wise parabolicity, therefore Eq. 6.28 in only an approximation. To verify the quality of this approximation we derive an equation of motion for the density of the interacting site $n_0(t)$ which can be expressed in terms of the density matrix $\rho_{i,j}(t)$. Using the equation of motion for the density matrix we arrive at the following equations for the interacting site, i.e., $i = 0$

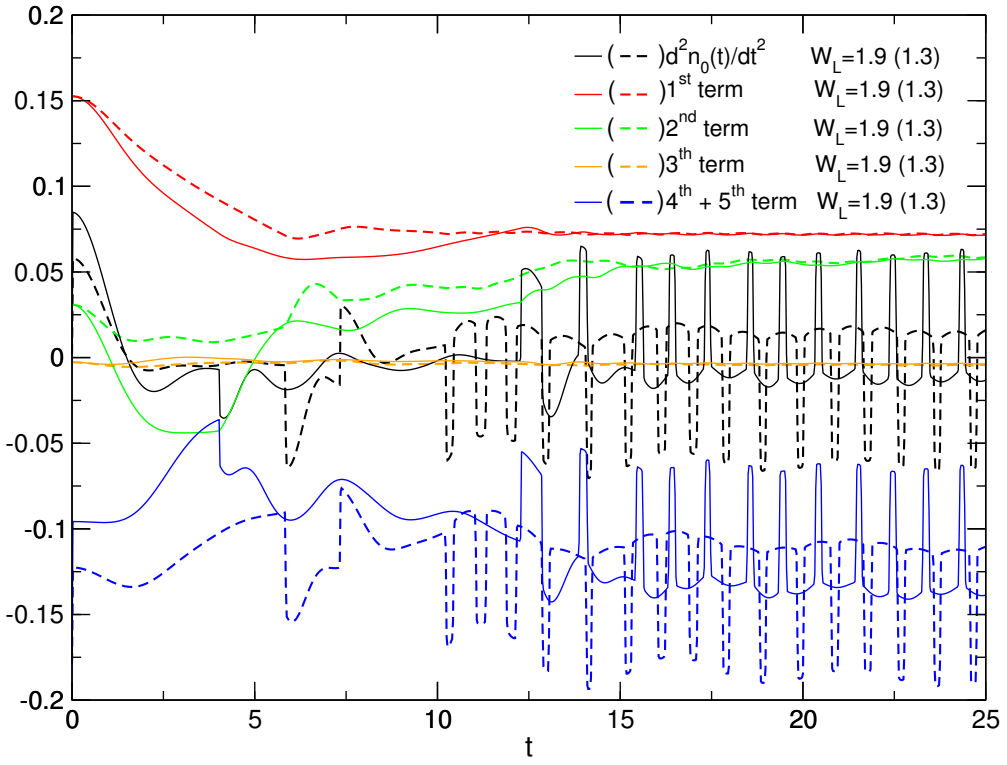

FIGURE 6.7: Time evolution of the second derivative of the density for two different biases and different terms of Eq. 6.30. Thin lines correspond to $W_L = 1.9$ while the thin dashed ones are for $W_L = 1.3$.

$$\begin{aligned}
\frac{d^2}{dt^2}n_0(t) &= 2V_{\rm link}^2(n_1 + n_{-1} - 2n_0) \\
&- VV_{\rm link}Re[\rho_{0,2} + \rho_{0,-2}] \\
&+ 4V_{\rm link}^2 Re[\rho_{1,-1}] \\
&+ 2(v_{\rm KS}(t) + v_{\rm g}(t) - W_L(t) + \epsilon_0 - \epsilon_L)V_{\rm link}{\rm Re}[\rho_{0,-1}(t)] \\
&+ 2(v_{\rm KS}(t) + v_{\rm g}(t) - W_R(t) + \epsilon_0 - \epsilon_R)V_{\rm link}{\rm Re}[\rho_{0,1}(t)], \qquad (6.30)
\end{aligned}$$

and the first derivative of the density is given by

$$\frac{d}{dt}n_0(t) = 2V_{\rm link}{\rm Im}\,[\rho_{0,1} + \rho_{0,-1}]. \qquad (6.31)$$

In Fig 6.7, we show the second derivative of the density for bias values $W_L = 1.3$ (thin line) and $W_L = 1.9$ (thick dashed line). In the same figure, we plotted the contribution of different terms of Eq. 6.30 and see after the transient regime the first term on right hand side of Eq. 6.30 corresponding to bias values $W_L = 1.3$ and $W_L = 1.9$ are very close to each other and eventually approach almost a constant value in the long time

limit. The same is true for the second and third term of right hand side of Eq. 6.30. On the other hand, the last two terms (blue curves) are very distinguishable for different bias values and have the leading role in the long-time behavior of the second derivative of $n_0(t)$. The relatively large oscillations in the last two term are expected due to the discontinuous (or rapidly varying) nature of the KS potential which appears in these two terms. It is noteworthy to see that in the case of larger(smaller) bias, the term $|n''_+|$ is smaller(larger) than n''_- and as a result T_+ is larger (smaller) than T_-, i.e., the time dependent density for most of a period stays above (below) unity. The relation between T_+ and T_- can be also realized from to the last two terms of Eq. 6.30 and considering that $\mathrm{Re}[\rho_{0,-1}(t)]$ and $\mathrm{Re}[\rho_{0,1}(t)]$ are negative. If the bias increases further (larger than $W_L = 1.9$) , $|n''_+|$ approaches zero which makes T_+ very large. Hence, after a critical bias, due to the positive rate of the change of the density, only a very small amount of density flows back into the leads right after the time-dependent density hits unity and it keeps increasing until it approaches a steady state. In the same way if the bias is smaller than a critical value, the steady state is achieved eventually.

This means that for bias values outside the Coulomb blockade regime the KS potential reaches a time-independent value in the long-time limit and therefore the system reaches a steady state with a non-zero current. This is shown in Fig 6.8, where the time-dependent density of the impurity site for bias $W_L = 0.5$ and $W_L = 2.5$ approaches a value far from unity after some transient and the KS potential goes to a constant value at $t \to \infty$. Interestingly, the KS potential for bias $W_L = 2.5$ jumps up around $t \approx 4$ when the density passes unity, but in this case the curvature of the density at $t \approx 4$ is very close to zero $|n''_+| \approx 0$ and due to the positive rate of the change of density, it does not fall below unity. In the same figure the time dependent density and KS potential at the HF level is presented for bias value $W_L = 1.6$ (all other parameters are identical with the one in Fig 6.5). In this case although the density of the impurity site is almost one, the oscillation in the density as opposed to BALDA are absent because the Hartree potential changes continuously as the number of electrons on the dot goes through an integer and as a result the time propagation naturally evolves to a steady-state in the longtime limit going, of course, through a transient period with decaying current (density) oscillations. We emphasize again that a continuous exchange-correlation potential such as the Hartree approximation cannot capture the Coulomb blockade phenomenon.

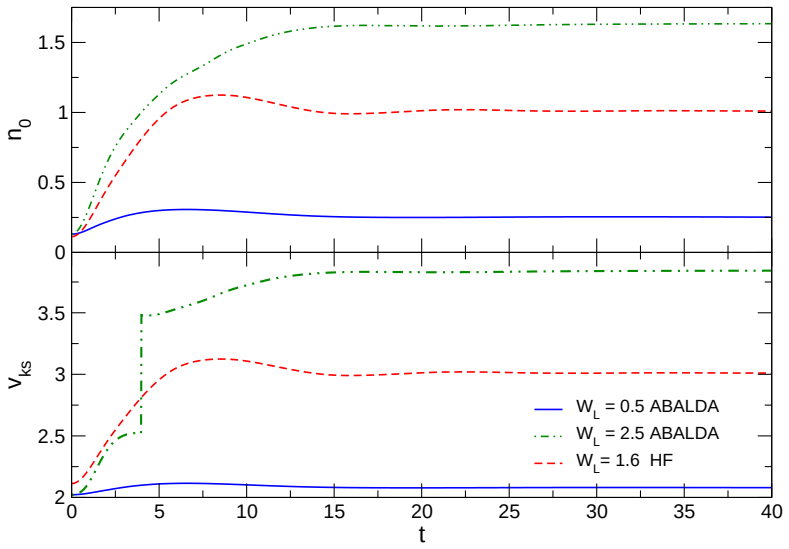

FIGURE 6.8: Time evolution of the density and KS potential for $W_L = 0.5$, 2.5 within BALDA and $W_L = 1.6$ within HF approximation (red curve) .

6.4 History Dependence, Oscillations and Smoothening

To shed some light on the history dependence of oscillations, we have calculated the time-evolution of the system as obtained by switching the bias as $W_L(t) = W_L \sin^2(\frac{\pi t}{2T_{\text{switch}}})$ for $t < T_{\text{switch}}$ and $W_L(t) = W_L = \text{const}$ otherwise.

The Fourier analysis of the density oscillations reveals peaks whose position and height depend on T_{switch}, i.e., on the history of the applied bias. However, it turned out that the main frequency of oscillation, ω, does not show a strong dependence on the history of the applied bias for small T_{switch} namely the frequencies remain almost constant for $T_{\text{switch}} < 30$. For fast switching times, the main frequency ω is given in Table 7.1 for different bias values, which shows that the larger the applied bias, the larger the (main) frequency of oscillations gets.

It is noteworthy to point out that the main frequency (with the largest amplitude) obtained from the Fourier analysis of the density oscillations for different values of final bias W_L agrees very well with the frequency calculated from the approximate Eq. 6.29 with time average value of $n''_{\pm}$ as input.

In addition to the main frequency, other peaks are also present in the Fourier transformation of the density whose frequencies are either integer multiples of the main frequency or equal the applied bias, and their amplitudes are few orders of magnitude smaller than the main one.

W_L	1.2	1.4	1.6	1.8
ω	5.11	5.50	5.85	6.13

TABLE 6.1: The main frequency ω for different values of bias applied suddenly.

Furthermore, we found that for any small but finite a, the amplitude of the oscillations approaches zero as $T_{\text{switch}} \to \infty$. This can be understood from Eq. 6.28, where the amplitude of oscillations is approximately given by $\frac{\beta+\tilde{\beta}}{4} = \frac{n'(t_1)^2}{4}[\frac{1}{n''_-} + \frac{1}{|n''_+|}]$. In the case of adiabatic switching, $T_{\text{switch}} \to \infty$, the rate of the change in the density and as a result the amplitude of oscillations approach zero. We therefore conclude that in this case the L+DFT approach gives the same solution as TDDFT for sufficiently slow switching [87]. For $a = 0$, instead, the system never reaches a steady state.

6.5 Coulomb Blockade Regime from the Steady-state Approach

The oscillations just described are distinct from those occurring in the presence of single particle bound states (see Chapter 4): They are induced by electron correlations. An especially revealing feature is that at long times the system is in a *dynamical state of oscillating density and current*, whose time-average is fairly constant for a large range of biases. For further insight, we now use the L+DFT approach which yields the same solution as TDDFT for smoothening parameters $a \neq 0$ and for adiabatic switching.

The steady-state density at the quantum dot is obtained from the self-consistency condition. Here we rewrite Eq. 5.49 for a single interacting quantum dot

$$n_s = n_0^\infty = 2 \sum_{\alpha=L,R} \int_{-\infty}^{\varepsilon_F+U_\alpha} \frac{\mathrm{d}\omega}{2\pi} \Gamma(\omega - U_\alpha) |G_{CC}^{\mathrm{KS},R}(\omega)|^2 \,. \tag{6.32}$$

Here $G_{CC}^{\mathrm{KS},R}(\omega) = \left(\omega - v_{\mathrm{KS}}(n_0^\infty) - \sum_\alpha \Sigma_{\mathrm{em}}^R(\omega - U_\alpha)\right)^{-1}$ is the retarded Green function at the quantum dot site, which depends on n_0^∞ through v_{KS}. Here we use the notation n_s for steady-state density.

We first consider a discontinuous v_{xc} (i.e. $a = 0$). In Fig 6.9, we display the left hand side and the right hand side of Eq. 6.32 as function of n_s for the parameters $V = 1$, $V_{\mathrm{link}} = 0.3$, $U = 2$, $v_{\mathrm{ext}} = 2$, $\varepsilon_F = 1.5$ and for different values of the dc bias W_L. These are the parameters used in our TD simulations of Fig 6.9. Interestingly, there is a range of applied bias voltages for which Eq. 6.32 *does not have a solution.* Since Eq. 6.32 is

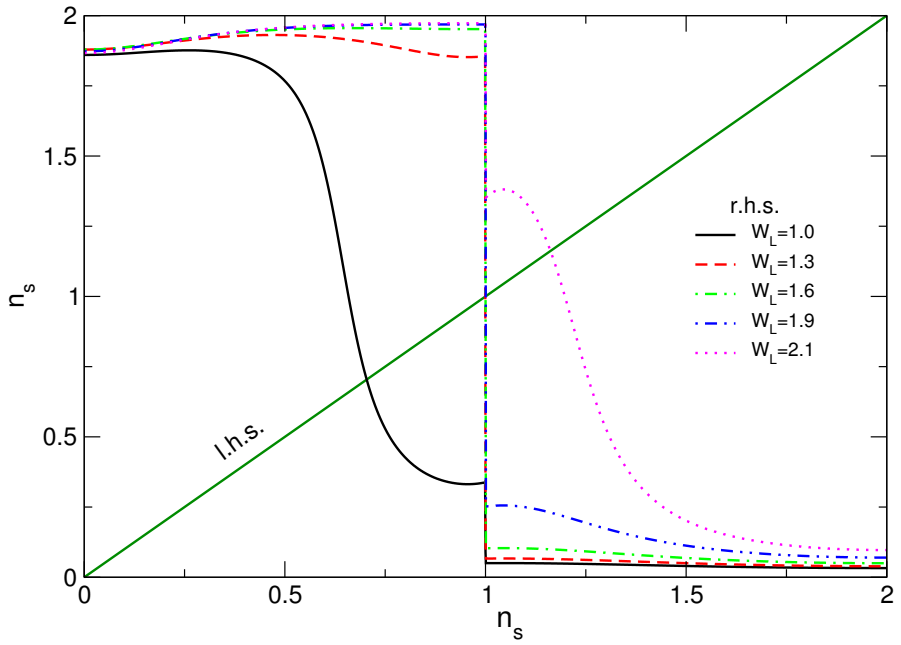

FIGURE 6.9: Graphical solution of Eq. 6.32 for few values of the applied bias W_L.

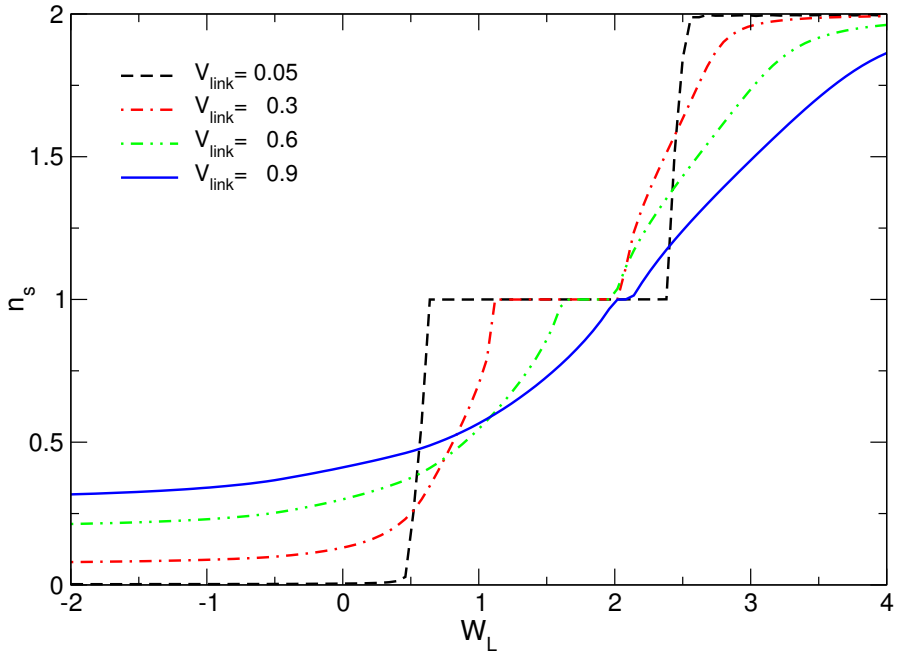

FIGURE 6.10: Steady-state density as function of W_L for a smoothened $v_{\rm KS}$ with $a = 10^{-4}$ for a few values of the dot-lead hopping parameter $V_{\rm link}$.

a condition for the quantum dot density at the steady-state, it follows that, as a direct consequence of the discontinuity in $v_{\rm xc}$, for some values of W_α, *no steady state exists*. On the other hand, for smoothening parameter $a = 10^{-4}$, as in our TD simulations, Eq. 6.32 admits steady state solutions; however, from Fig 6.5, we know that, in general, the system time-evolves towards an oscillating regime and that the solution of the L+DFT scheme is a solution in TDDFT for adiabatic switching. To show that in fact

we *are* in the Coulomb blockade regime, in Fig 6.10 we display the steady state density n^{∞}, as a function of W_L. As before, $v_{\mathrm{g}} = 2$, $\varepsilon_{\mathrm{F}} = 1.5$, $U = 2.0$ and $a = 10^{-4}$. We clearly see a plateau in the density at unity developing for a range of bias values W_L (for $V_{\mathrm{link}} = -0.3$, the W_L's of our TD simulations correspond to the beginning, middle, and end of the plateau). Interestingly, the plateau becomes wider and more step-like as V_{link} decreases, and in the limit of very small V_{link} its length becomes equal to the charging energy U. This corresponds to the usual Coulomb blockade picture: if the site is occupied by one electron, a second electron can only jump in if its energy exceeds the charging energy of the quantum dot.

As emphasized in the previous section the discontinuity of the exchange-correlation potential is a crucial property to be able to describe Coulomb blockade and in particular to get the step-like feature in the steady-state density as function of bias (or gate), i.e., within a continuous approximation to the KS potential the step is completely absent. The steady-state density calculated using the Hartree approximation, for instance, rises almost linearly within a certain bias range for small V_{link}.

When leaving the Coulomb blockade regime, i.e. for larger values of V_{link}, within BALDA the step is either very small or absent and n_s as function of bias calculated within the Hartree approximation behaves qualitatively similar to BALDA.

At the end of this section, we demonstrate how the groundstate density within the BALDA approximation compares to the exact Quantum Monte Carlo (QMC) calculations presented by Wang et al. in Ref. [88]. The QMC results were performed for a single interacting quantum dot with various values for the interaction strength $U = 0.105, 0.21, 0.42, 0.84$. For the hopping between leads and impurity we take a weak $V_{\mathrm{link}} = 0.1803$. In order to achieve a meaningful comparison to the QMC data, the value of our V_{link} is a factor of $1/\sqrt{2}$ smaller than the one used in Ref. [88] since Wang et al. considered an impurity coupled to a single lead only. For the smoothening parameter we choose the value $a = 10^{-3}$. Fig 6.11 shows the groundstate density as function of gate voltage v_g. We observe that the QMC and BALDA results agree surprisingly well, especially for weak interactions limit. For strong interactions the BALDA develops a clear Coulomb blockade step, i.e., the density hardly changes over a significant range of on-site energies. Although the step in BALDA extends over a smaller range of on-site energies than in QMC, the agreement is still quite reasonable. Certainly, the feature which gives rise to the Coulomb blockade step is the derivative discontinuity built into the BALDA functional.

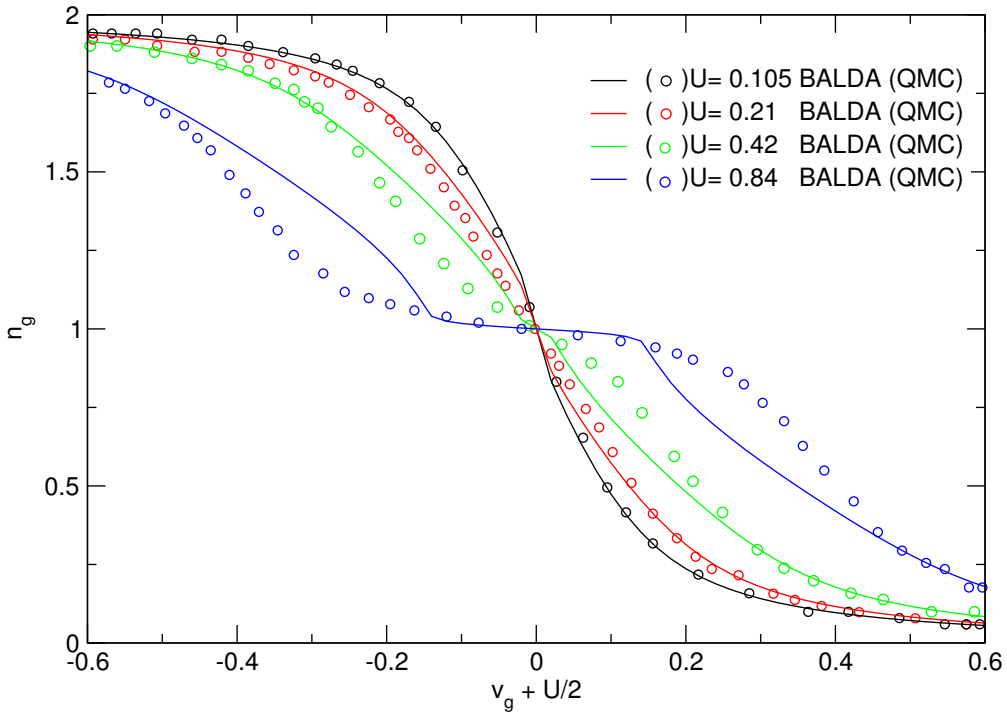

FIGURE 6.11: Comparison of BALDA and QMC groundstate densities at the impurity as function of on-site energy $v_g + U/2$ for different values of the interaction.

6.6 Some Considerations on the Exchange-correlation Potential

Here we wish to comment on the ABALDA which it is based on two approximations: the locality in space and in time (adiabatic approximation). Dropping only the assumption of locality in space for $v_{\rm xc}$, the latter will depend (instantaneously) on the densities at few, say M, sites around the quantum dot. We will have a steady state condition given in Eq. 5.49, in the form of a set of equations for the densities at the M sites. For a discontinuous $v_{\rm xc}$ at one (or more) of the M sites, these equations may not have a solution. It is much more difficult to assess the role of non-locality in time, where $v_{\rm xc}$ depends on the density at all earlier times. This would require to develop XC functionals with memory, for example via non-equilibrium Many-Body Perturbation Theory [48, 49, 65] or through fluid dynamical considerations [89, 90].

We can now provide an answer to the two questions posed at the beginning of this chapter. A discontinuous or rapidly varying $v_{\rm xc}$ is central to the description of the Coulomb blockade within L+DFT and TDDFT. For KS potentials with a true discontinuity, the

steady-state self-consistency condition in L+DFT cannot always be satisfied. Considering a smoothened discontinuity (which, as said earlier, is physically more realistic) the L+DFT approach yields a clear-cut Coulomb blockade scenario. However, if the very same XC potential is used as adiabatic approximation in a TDDFT framework it leads to a dynamical state with history-dependent, self-sustained density and current oscillations: where the static approach gives Coulomb blockade , the TD approach gives oscillations. The average of these oscillations corresponds to the L+DFT solution. The latter is a TDDFT solution only for an adiabatic switch-on of the time-dependent perturbation.

In conclusion, our results suggest that Coulomb blockade is an intrinsically TD phenomenon, i.e., it corresponds to an oscillatory current representing the intuitive picture of Coulomb blockade as a sequence of charging and discharging of the weakly coupled molecule or quantum dot. While our calculations are performed for a model consisting of a single correlated quantum dot coupled to non-interacting leads, we expect the results to be of general nature: In the continuum-real-space TDDFT description, whenever the particle number on the molecule or quantum dot crosses an integer, the discontinuity of the time-dependent XC potential [91] will trigger persisting charge and current oscillations which cannot be captured in any steady-state approach.

Chapter 7

Multistability at the Nanoscale: Real-time Switching between Multiple Steady-states and Correlation Effects

In this chapter, the possibility of finding multistability in the density and current of an interacting nanoscale junction coupled to semi-infinite leads is studied at various levels of approximation.

The occurrence of bistability has been the subject of several studies in the field of quantum transport. In their seminal paper Goldman *et al.* [92] reported the observation of bistability in the I-V curve of double-barrier resonant tunneling (DBRT) structures, thus stimulating many theoretical [93–96] and experimental investigations [97, 98] on the subject. Bistability is a non-linear effect induced by the electrostatic charge build-up in the quantum well and occurs in the bias window of negative differential resistance [92].

From the theoretical point of view, various techniques have been used to capture this phenomenon, ranging from a crude estimate of the charge build-up [97] to self-consistent calculations at the mean field-level [93–95, 99–101].

With the increasing interest in transport through nanoscale devices, in particular using molecules as a possible component of future electronic circuits with great promise in the process of miniaturization [70], the study of intrinsic bistability in nanoscale devices has gained new attention.

This is due to the fact that the success of molecular-devices is connected to the possibility of finding molecular devices equivalent to conventional non-linear devices, such as diodes and transistors. There have already been some successful attempts along these lines. Molecular devices with large on-off current ratio and large negative differential resistance, behaving similarly to mesoscopic DBRT structures, have been reported [102, 103]. So far, the great majority of bistability studies have been limited to the steady-state regime and performed within the framework of the Landauer formalism combined with static DFT. At the Hartree level, bistability was reported for a double quantum dot structure [39, 104].

Here we study an interacting nanoscale junction coupled to semi-infinite leads which is driven out of equilibrium by an external bias and the non-equilibrium properties are determined by real-time propagation using both time-dependent density functional theory and many-body perturbation theory. In TDDFT the exchange-correlation effects are described within the adiabatic Bethe ansatz local density approximation given in Eq. 5.22. In the context of TDDFT, the inclusion of memory effects beyond the adiabatic approximation is not straightforward and the development of accurate functionals to be used in numerical calculations is still under way. A promising and timely, even though computationally demanding, alternative is the solution of the Kadanoff-Baym equations [48–52, 63] using self-energies from MBPT. The advantage of MBPT over TDDFT is that the inclusion of dynamical exchange-correlation effects, i.e., effects arising from a frequency-dependent self-energy, can be achieved in a more systematic way through the selection of suitable Feynman diagrams. Thus, MBPT provides an important tool to go beyond the commonly used adiabatic approximations and to quantify the importance of memory effects through advanced approximations to the self-energy.

The fundamental issue which we address in this chapter is whether the bistability phenomenon found in static DFT, Hartree and Hartree-Fock approximation survives when dynamical XC effects are taken into account. In contrast to DFT and mean-field approximations the steady-state equations of MBPT do not form a closed set of equations for the density only. This difficulty renders the search for bistability in MBPT computationally very costly. To overcome the problem we implement a time-dependent strategy. We first solve the steady-state equations of DFT and mean-field theory to determine the parameter range for bistability. Then we go beyond the current state-of-the-art

and provide a TD description of the bistability phenomenon in adiabatic TDDFT [28–30, 78, 105–107] and TD mean field theory. We show how to switch between different stable states by means of ultrafast gate voltages. The possibility of reversibly switching between different stable steady-states is an aspect that has remained largely unexplored. Knowing how to steer the electron dynamics in real time we finally use the same driving fields in correlated MBPT simulations.

7.1 Stability Analysis of the Solutions: the Fixed-point Theorem

From Eq. 5.49 we have a set of N_c coupled, nonlinear equations for the steady state density n_j^∞, $j = 1, \ldots, N_c$ at the N_c sites of the interacting device region. These equations are nonlinear and it is therefore possible that they have more than one solution. We will use them to scan the parameter space for sets of parameters leading to multiple steady-states. Clearly, the time evolution of the system, will tell us if and how the system eventually reaches a steady state. In particular, the steady states accessible by time evolution are the ones that are stable. However, even without doing the time propagation, the stability of steady-state solutions can be analyzed by means of the fixed-point theorem. Consider a system of n_{Nc} coupled equations of the following general form [108]:

$$\mathbf{n} = \mathbf{g}(\mathbf{n}), \quad \mathbf{n} = (n_1, n_2, ..., n_{N_C})^T \tag{7.1}$$

Let the vector $\tilde{\mathbf{n}}$ be a solution of Eq. 5.49 called "fixed point" and $\mathbf{J}$ the Jacobian matrix $\frac{d\mathbf{g}}{d\mathbf{n}}$ evaluated at $\tilde{\mathbf{n}}$. The eigenvalues $\mu_1, \mu_2, ..., \mu_{N_C}$ of $\mathbf{J}$ are called the multipliers of the fixed point. We define m_-, m_0 and m_+ to be the number of the multipliers of the fixed point $\tilde{\mathbf{n}}$ lying inside, on, and outside of the unit circle centered at zero, respectively.

- A fixed point is *stable* if $m_- m_+ = 0$ and $m_- = N_c$, i.e, the absolute values of all multipliers are inside the unit circle ($|\mu_i| < 1$ for all values of i)

- A fixed point is *unstable* if $m_- m_+ = 0$ and $m_+ = N_c$, i.e, the absolute values of all multipliers are outside the unit circle ($|\mu_i| > 1$ for all values of i)

- A hyperbolic fixed point is called hyperbolic *saddle* point if $m_- m_+ \neq 0$ and $m_0 = 0$

7.2 Results

In this Section, we present the results of our numerical simulation for a certain set of parameters for which the self-consistency condition (5.49) admits multiple solutions. We investigate how one can switch between different stable solutions by applying a time-dependent gate voltage. We also demonstrate that for the same parameter sets the bistability is suppressed in the correlated many-body approximations, e.g., 2B and GW. The analysis will be carried out in two types of model devices, namely the one and two-site Hubbard models.

7.2.1 Single-site Hubbard Model

As a first example, we study a single-site Hubbard model connected to semi-infinite leads with the following parameters:$V_{\text{link}} = 0.3$, $W_L = 1.8$, $W_R = -1.0$, $U = 2.0$, $\varepsilon^C =$ -0.6, $\varepsilon_\alpha = \varepsilon_F = 0$ (half-filled leads), and the inverse temperature $\beta = 90$. All energies are measured in units of the lead-hopping parameter V. In the biased system the bandwidth of the leads extends from $\varepsilon_F + W_\alpha - 2V$ to $\varepsilon_F + W_\alpha + 2V$. With these parameters the self-consistent equation (5.49) admits five (three) solutions within the HF (BALDA) approximation . The fixed points are shown in the lower left corner of Fig 7.1 where we display the left and right hand side of Eq. 5.49. The corresponding densities in the case of HF are $\tilde{n}_1 = 0.17$, $\tilde{n}_2 = 0.54$, $\tilde{n}_3 = 1.0$, $\tilde{n}_4 = 1.46$ and $\tilde{n}_5 = 1.83$ while for the BALDA the three fixed-point densities are $\tilde{n}_1 = 0.18$, $\tilde{n}_2 = 1.00$, $\tilde{n}_3 = 1.82$.

For a single site the fixed-point theorem tells us that a solution is stable if $|\frac{dg}{dn}|_{n=\tilde{n}_i} < 1$, with g being the right-hand side of Eq. 5.49. Hence, one can see from Fig 7.1 that the fixed points $\tilde{n}_1$, $\tilde{n}_3$ and $\tilde{n}_5$ are stable in the case of the HF, while in the case of the BALDA the stable solutions are $\tilde{n}_1$ and $\tilde{n}_3$. Although the solution with density of unity exists for both approximations, it is stable in the HF approximation and unstable in the BALDA. In the upper panels of Fig 7.1 we plot the steady-state spectral functions corresponding to the fixed points of the HF and BALDA. The HF peak for density $\tilde{n}_1 = 0.17$ (and the BALDA peak for density $\tilde{n}_1 = 0.18$) is located within the right lead energy continuum, while the HF peak for density $\tilde{n}_5 = 1.83$ (and the BALDA peak for density $\tilde{n}_3 = 1.82$) is located within the left lead energy continuum. By contrast, the HF spectral function of the unstable fixed points, $\tilde{n}_2$ and $\tilde{n}_4$, are peaked at the edges

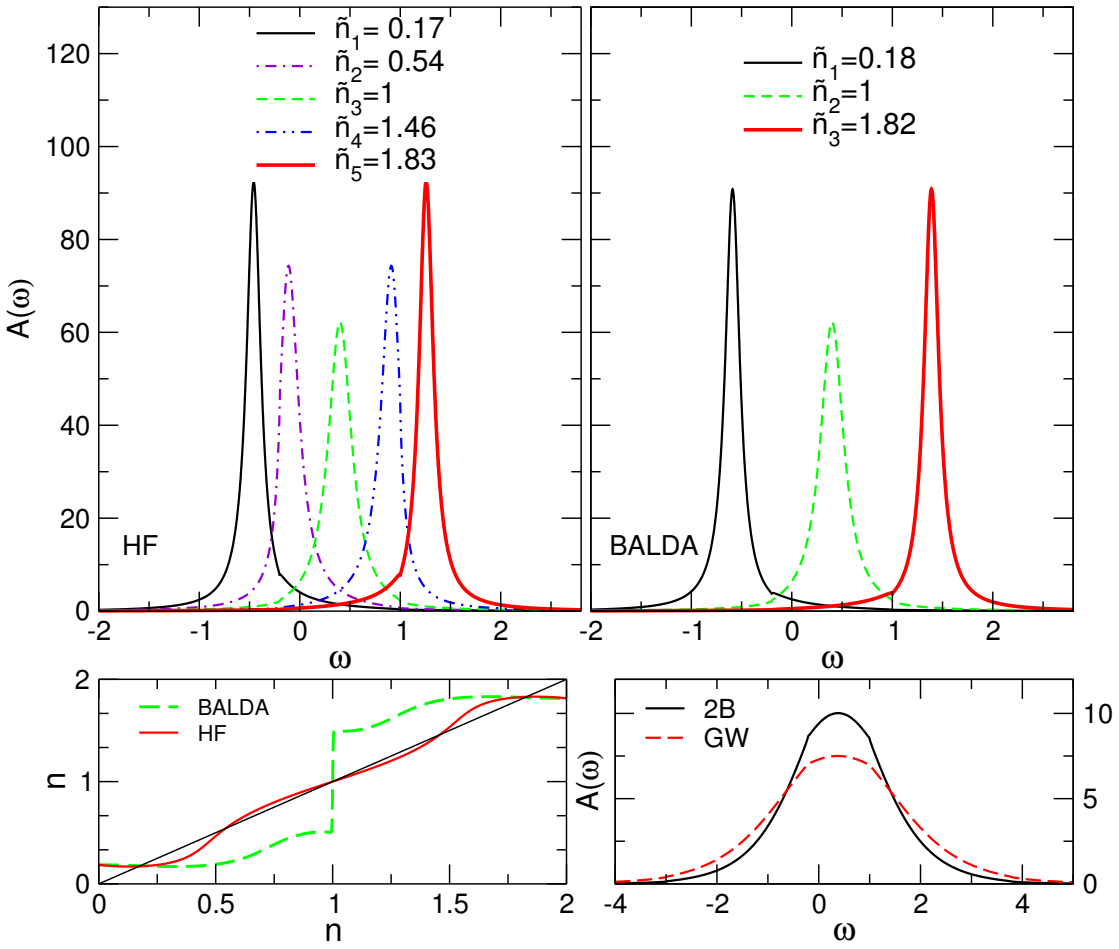

FIGURE 7.1: Spectral functions for the different steady-state solutions of the HF approximation(top-left panel) and BALDA (top-right panel). The graphical solution of Eq. 5.49 is displayed in the bottom-left panel for the HF and BALDA. For comparison we also report the 2B and *GW* steady-state spectral functions in the bottom-right panel. In 2B and *GW* the steady-state density is unique and has a value close to $\tilde{n} = 1.0$.

of the left and right lead band respectively. The HF and BALDA spectral functions of the fixed point with density of unity are identical (the XC potential is zero in this case) and the peak is located exactly in the middle of the overlapping region between the left and right bands. In spite of this, the stability condition of this fixed point is completely different in the HF and BALDA case. Since the multistability can be most easily observed if the spectral peaks of the stable solutions are well separated, we conclude that this phenomenon is favored when the energy bands have a small overlap and the system is in the negative differential resistance (NDR) regime.

As we shall see below, for the correlated MBPT approximations the situation is very different. In the lower right panel of Fig 7.1 we show the 2B and *GW* steady-state spectral functions, as obtained from the propagation of the KB equations. The spectral

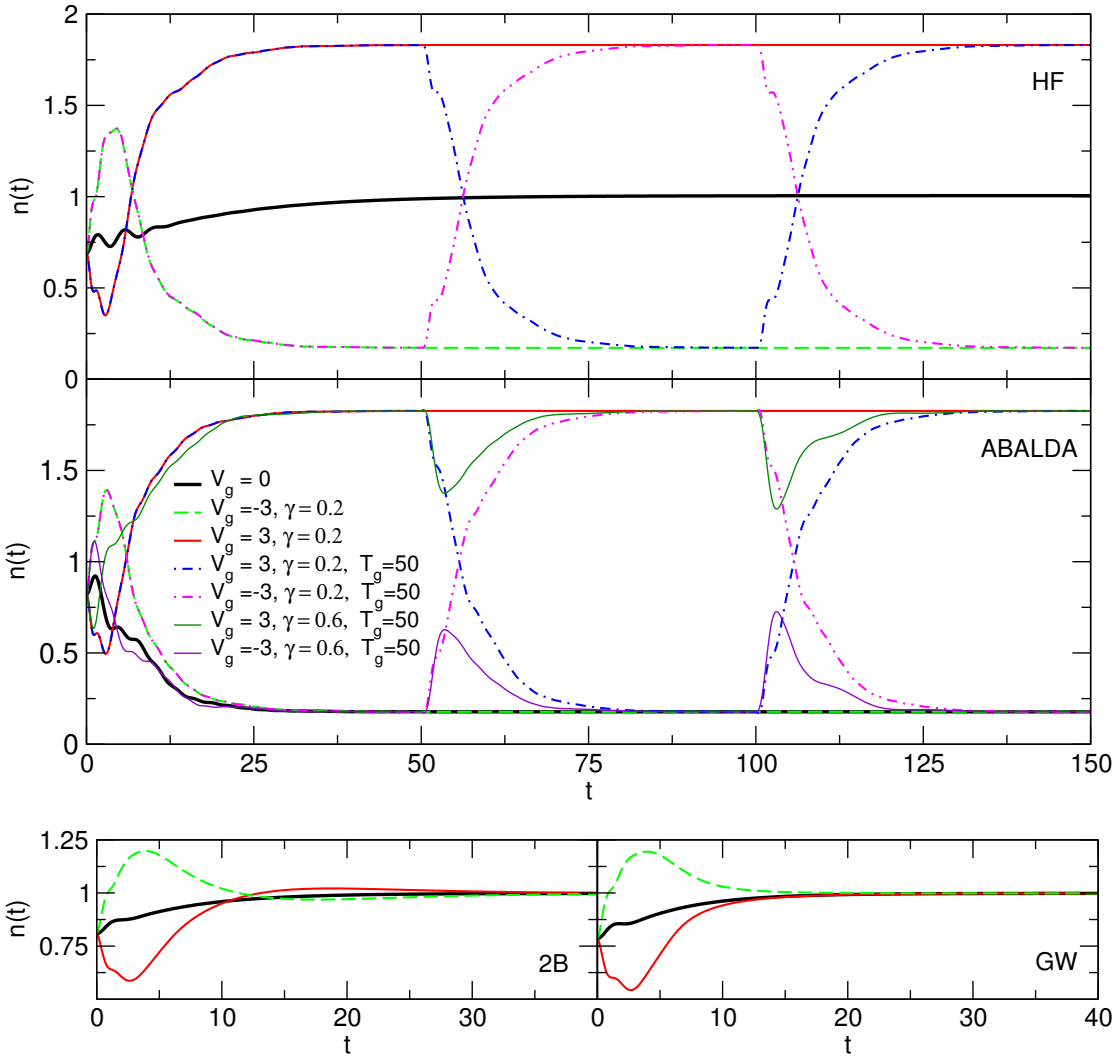

FIGURE 7.2: Top panel: Time-dependent density in the HF approximation (top) and ABALDA (bottom) after the sudden switch on of the bias voltage and a series of gate pulses as in Eq. 7.2. Bottom panel: Time-dependent density within 2B (left) and *GW* approximations (right) after the sudden switch on of the bias voltage and a gate pulse as in Eq. 7.2 with $V_g = -3, 0, 3$.

weight is spread over the whole lead energy range and beyond. Consequently, the height of the spectral function is also much smaller. The considerable broadening is due to an increased quasi-particle scattering in the out of equilibrium system as already observed in Ref. [49].

Let us now study how to switch between different stable steady-state densities using ultrafast time-dependent driving fields. We start from the initially unbiased equilibrium system with groundstate density $\tilde{n}_g = 0.69$ ($\tilde{n}_g = 0.82$) for HF (BALDA). In Fig 7.2 we show the time evolution of the density at the interacting site for different approximations after the sudden switch on of the bias voltage $W_L = 1.8$ and $W_R = -1.0$. In the HF

approximation we observe that, after some transient time, the density approaches the value 1. The behavior of the ABALDA density is very different: In agreement with the fact that the solution with density of unity is unstable, it cannot be reached by time evolution. At the steady state the ABALDA density equals the lowest value $\tilde{n}_1$.

To switch to the other stable solutions in real time we applied a time-dependent gate pulse on the Hubbard site. We have used an exponentially decaying gate voltage of the form

$$V_g(t) = \begin{cases} V_g e^{-\gamma t} & , \text{ if } 0 < t < T_g \\ -V_g e^{-\gamma(t-T_g)} & , \text{ if } T_g < t < 2T_g \\ V_g e^{-\gamma(t-2T_g)} & , \text{ if } t > 2T_g \end{cases} . \tag{7.2}$$

In Fig 7.2 we show that in the HF case, the state with the lowest density $\tilde{n}_1$ can be obtained (in addition to applying a sudden bias in the leads) by switching on a pulse with amplitude $V_g = -3.0$, decay rate $\gamma = 0.2$ and $T_g = \infty$. The state with highest density $\tilde{n}_5 = 1.83$ can be obtained in a similar fashion but now applying a gate with positive amplitude $V_g = 3.0$. Thus, by changing the amplitude of the gate voltage we can switch between stable steady-state solutions. For instance, with a first pulse of positive amplitude and $T_g = 50 \gg 1/\gamma$ the system reaches the state with $\tilde{n}_5$. At the time T_g we apply a second pulse but with negative amplitude. The density shows a transient behavior after which it approaches the value $\tilde{n}_1$. If we now apply a third pulse of positive amplitude at time $2T_g$ the density goes back to the initial value $\tilde{n}_5$. This is nicely visible in Fig 7.2. In Fig 7.3 we show the non-equilibrium HF spectral function $A(T, \omega)$ of Eq. 5.36 for a double switch with $V_g = -3.0$, $\gamma = 0.2$ and $T_g = 50$. The figure enlightens an interesting aspect regarding the transition from one steady-state to another. The density rises from the lowest $\tilde{n}_1$ to the highest $\tilde{n}_5$ lingering for a while in the middle stable solution $\tilde{n}_3$.

Going back to Fig 7.2 we see that also in the ABALDA the state with highest density $\tilde{n}_3 = 1.83$ is reached by applying a gate pulse with $V_g = 3.0$ and $\gamma = 0.2$ (in addition to a sudden bias in the leads). If the amplitude is negative instead ($V_g = -3.0$) the density increases first but eventually drops down and goes back to its initial value $\tilde{n}_1$. Like in the HF case we can switch back and forth between stable solutions by changing the sign of V_g. Not unexpectedly, however, the decay time $\tau_\gamma \sim 1/\gamma$ cannot be arbitrarily short. If τ_γ is too short the system does not have time to accumulate or lose enough density to

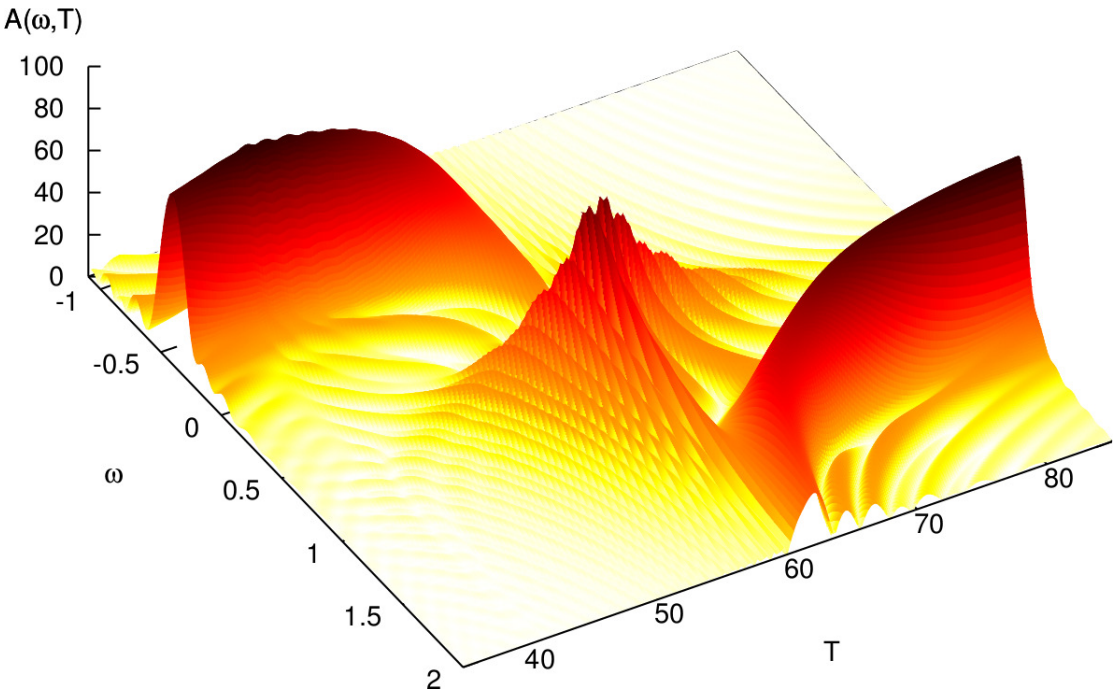

FIGURE 7.3: Non-equilibrium spectral function for a gate pulse $V_g = -3$, $\gamma = 0.2$ which brings the density to $\tilde{n}_1$ first, followed by a second identical gate pulse gate but with opposite amplitude which brings the density to $\tilde{n}_5$. The intermediate transition to the $\tilde{n}_3$ stable solution is clearly visible.

change the self-consistent potential and after some transient it falls back to the previous steady-state value. This is clearly shown in Fig 7.2 for the amplitude $V_g = \pm 3.0$, $T_g = 50$ and a faster decay rate $\gamma = 0.6$.

Intuitively one would expect that by increasing (decreasing) the on-site energy of the Hubbard site the density decreases (increases). However, the highest (lowest) stable steady-state density is obtained with a positive (negative) gate. This is due to the fact that in our case the on-site energy of the Hubbard site lies below the energy band of the left lead. By applying a positive gate a finite hybridization occurs, leading to the migration of extra charge from the left lead to the Hubbard site. A similar argument explains the reduction of the density on the impurity site when a negative gate is turned on.

In the lower panels of Fig 7.2 we plot the densities obtained within the 2B and *GW* self-energy approximations. We have applied the bias voltage and a gate pulse of the form $V_g(t) = V_g e^{-\gamma t}$ for $t > 0$ with $V_g = 0, \pm 3$. In all cases only one steady state emerges at the end of the propagation with a density of about 1.0. It is worth observing that the 2B and *GW* steady-state values of the densities are close to each other, indicating

that the single-bubble diagram, common to both approximations, is the dominant term of the perturbative expansion in this case [49].

By time propagation we have shown that the three HF densities, $\tilde{n}_1$, $\tilde{n}_3$ and $\tilde{n}_5$, and the two ABALDA densities, $\tilde{n}_1$ and $\tilde{n}_3$, are stable in a slightly different sense than that of the fixed-point theorem. The fixed-point theorem does not contain any information on the actual dynamics. Similarly, the HF solutions $\tilde{n}_2$ and $\tilde{n}_4$ as well as the ABALDA solution $\tilde{n}_2$ are unstable in the sense that there exist no external perturbation to drive the system toward them. Thus, the fixed-point theorem provides us with a good criterion to establish whether a given steady-state can be reached or not. This criterion is certainly rigorous in the limit of adiabatic switchings but, as we just found, its validity extends well beyond the adiabatic regime.

The time-dependent currents for the various approximations are shown in Fig 7.4. Corresponding to the three stable HF steady-state densities there exist only two distinguishable values for the current $I_R(t)$ at the interface between the Hubbard site and the right lead. The lower value corresponds to the solutions $\tilde{n}_1$ and $\tilde{n}_5$, while the higher value corresponds to the solution $\tilde{n}_3$. The existence of only two solutions for the current is the consequence of an approximate particle-hole symmetry of the self-consistent equation (5.49), i.e., $\tilde{n}_5 \sim 1 - \tilde{n}_1$. One particularly appealing feature of the HF currents is the large difference between the two steady-state values, a highly desirable property for designing nanoscale diodes.

The particle-hole symmetry holds also for the ABALDA and therefore the steady-state currents corresponding to the two stable solutions are almost indistinguishable. Finally, the 2B and *GW* steady-state values of the currents, approach the same value independent of the gate voltage, in agreement with the existence of a unique steady state.

Increasing the bias the number of HF fixed-point solutions reduces to three of which only two are stable. Also by increasing the interaction strength U the number of stable solutions reduces to two because a small amount of density causes a considerable change in the effective potential. As a consequence, the middle solution becomes unstable.

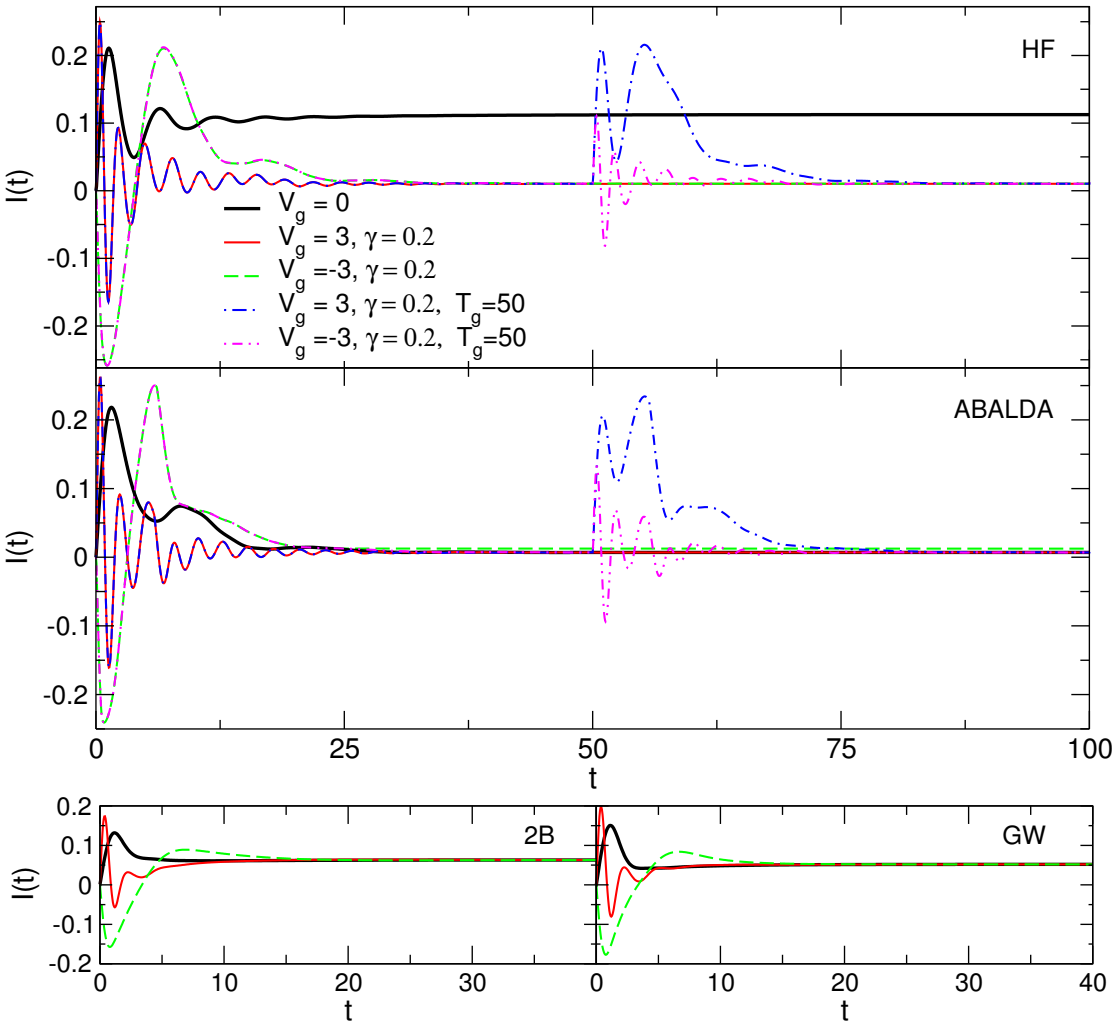

FIGURE 7.4: Time-dependent current after the sudden switch on of the bias voltage and of a gate pulse as in Eq. 7.2 in the HF (top-upper panel), ABALDA (top-lower panel), 2B (bottom-left panel) and GW (bottom-right panel) approximations. In the HF and ABALDA case a time-dependent switch between two different steady-states is shown.

7.2.2 Two-site Hubbard Model

In this Section we consider the case of two interacting sites ($N_C = 2$) connected to two semi-infinite, non-interacting tight-binding leads. We choose the following parameters: $V_{\rm link} = 0.4$, $W_{\rm L} = 2.2$, $W_{\rm R} = $ -1.2, $U = 2.0$, $V_C = V_{1,2} = 0.4$, $\varepsilon_\alpha = \varepsilon_F = 0$, $\varepsilon_1^C = \varepsilon_2^C = $ -0.6 and $\beta = 90$. The leads are half-filled and the lead bands have an energy range between $\varepsilon_\alpha + W_\alpha - 2V$ and $\varepsilon_\alpha + W_\alpha + 2V$.

Within the HF approximation, the steady-state condition (5.49) then has seven solutions which are shown in the upper panel of Fig 7.5. The black curve is obtained by finding the root of the equation $n_2 - g_2(n_1, n_2) = 0$ at fixed n_1 where $g_2(n_1, n_2)$ is the right

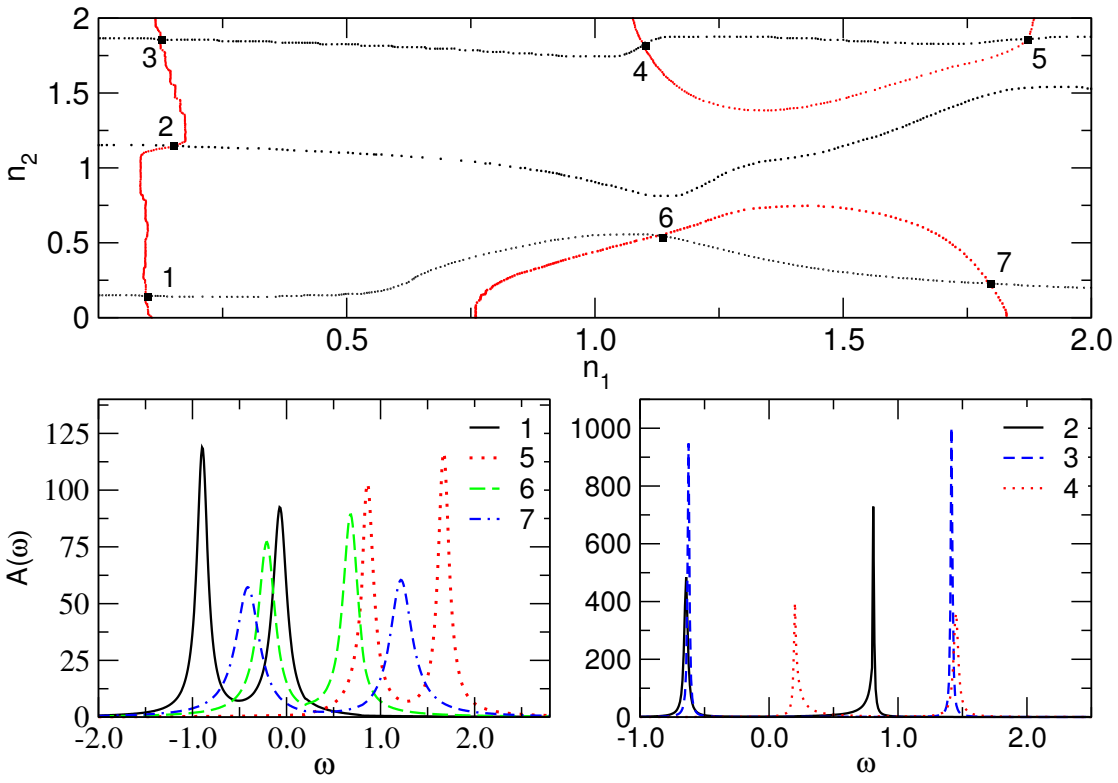

FIGURE 7.5: Upper panel: Graphical solution of the integral in Eq. 5.49. Lower panel: Spectral functions for the HF approximation with Hubbard interactions corresponding to the seven different steady-state solutions for the density.

FP	1	2	3	4	5	6	7
n_1	0.094	0.150	0.124	1.098	1.867	1.129	1.794
n_2	0.144	1.146	1.860	1.821	1.862	0.546	0.226

TABLE 7.1: Fixed point (FP) solutions of Eq. 5.49 for the steady-state densities of two interacting Hubbard sites connected to two biased, non-interacting leads in the HF approximation (see upper panel of Fig 7.5). The parameters are: $V_{\rm link} = 0.4$, $W_{\rm L} = 2.2$, $W_{\rm R} = -1.2$, $U = 2.0$, $V_{1,2} = 0.4$, $\varepsilon_\alpha = \varepsilon_F = 0$, and $\varepsilon_1^C = \varepsilon_2^C = -0.6$.

hand side of Eq. 5.49 with $j = 2$. The red curve is obtained in an analogous way by exchanging $1 \leftrightarrow 2$. Hence the intersections of the curves are the fixed points. The numerical values for the steady-state densities at the two Hubbard sites for the seven fixed points are given in Table 7.1.

In the lower panel of Fig 7.5 we show the spectral functions corresponding to the seven different fixed points (FPs). The spectral function for FP 1 is located mostly in an energy range within the energy band of the right lead, while the one for FP 5 has most of its weight in the energy range of the left lead. In contrast, FPs 6 and 7 have considerable weight in the energy bands of both leads. The spectral functions corresponding to FPs

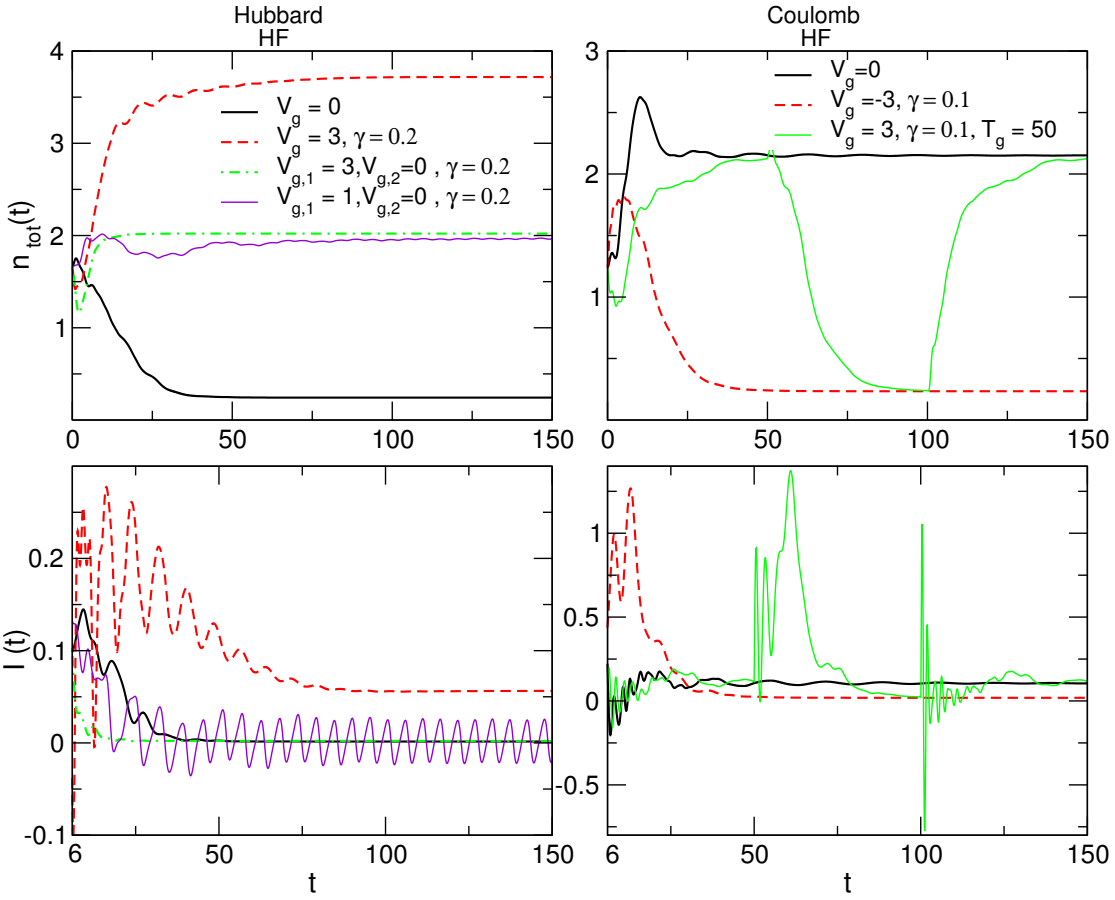

FIGURE 7.6: Densities and currents for the HF approximation in the case of short range (Hubbard) and long range (Coulomb) interactions. Switching between different steady states by applying an exponentially decaying gate of the form given in Eq. (7.2), is shown.

2, 3, and 4 have much narrower peaks than the spectral functions for the other fixed points. According to the fixed-point theorem only the FPs 1, 3, 5, and 7 are stable and we expect them to be accessible by time propagation. In the upper left panel of Fig 7.6 we show the time evolution of the total density on the two dots, $n_{\rm tot}(t) = n_1(t) + n_2(t)$, in the HF approximation for a sudden switch-on of the bias and several gate voltages starting from the equilibrium state with groundstate density $n_1 = n_2 = 0.83$. The steady state corresponding to FP 1 is obtained by applying only the bias (no gate). In the case where we apply, in addition to the bias, a decaying gate voltage of the form (7.2) to both sites with $V_{g,1} = V_{g,2} = V_g = 3.0$ and decay rate $\gamma = 0.2$, the total density increases and after some transient evolves towards the steady state corresponding to FP 5. In this case, lifting the on-site energy due to the gate voltage allows for extra charge to accumulate at the interacting sites such that the high-density steady-state solution can be achieved . In contrast, the solution of FP 7 can be obtained by applying the decaying

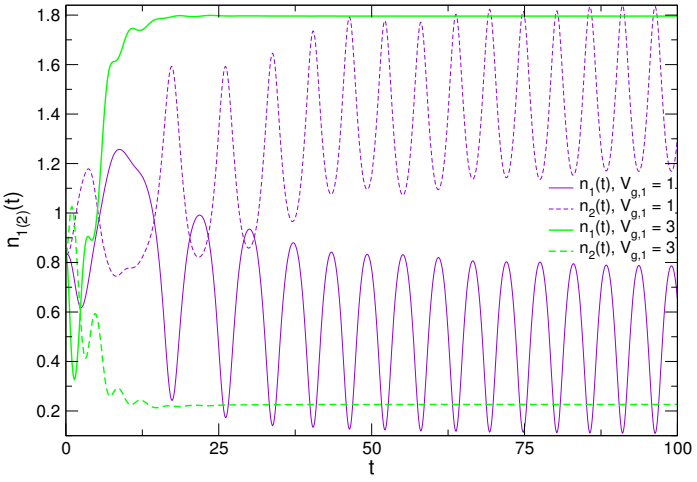

FIGURE 7.7: Densities of the first and second site for the HF approximation in the case of Hubbard interactions corresponding to the middle curves in the upper left panel of Fig 7.6

gate voltage to the first (left) site only with amplitude $V_{g,1} = 3.0$, $V_{g,2} = 0$ and $\gamma = 0.2$. Surprisingly, applying a similar asymmetric gate voltage but with a smaller amplitude ($V_{g,1} = 1.0, V_{g,2} = 0$), leads to a very different long time behavior. In this case the system does not evolve towards a steady state after the transients, instead we observe an oscillatory time-dependent density. In the long-time limit, the time-dependent total density (purple curve in the upper left panel of Fig 7.6) oscillates with an amplitude of the order of 10^{-3}, around 1.96. This value corresponds approximately to the total steady-state density of FP 3 of Fig 7.5. As observed from the upper left panel of Fig 7.6, after some transients the total time-dependent density (purple curve) goes close to the green curve which corresponds to the FP 7 with the total steady-state density of 2.02.

Despite this apparent similarity, the nature of these solutions is very different. While for the steady state of FP 7 the charge is mostly located at the first site, in the case of FP 3 the density on the first site is smaller than on the second one (see Table 7.1). The different nature of these two cases becomes even more obvious when looking at the time evolution of the density at the two interacting sites separately (see Fig 7.7). While in the first case ($V_{g,1} = 3.0$, $V_{g,2} = 0$) the steady state is attained quite rapidly, in the second case ($V_{g,1} = 1.0, V_{g,2} = 0$) we see non-decaying density oscillations at the individual sites with rather large amplitude of about 0.32 and frequency $\omega = 1.18$. In the long-time limit the density oscillates thus inducing an oscillating KS potential. The persistence of these oscillations means that the density solves the Floquet system of equations in which the harmonics of the potential depend on the density itself. At first

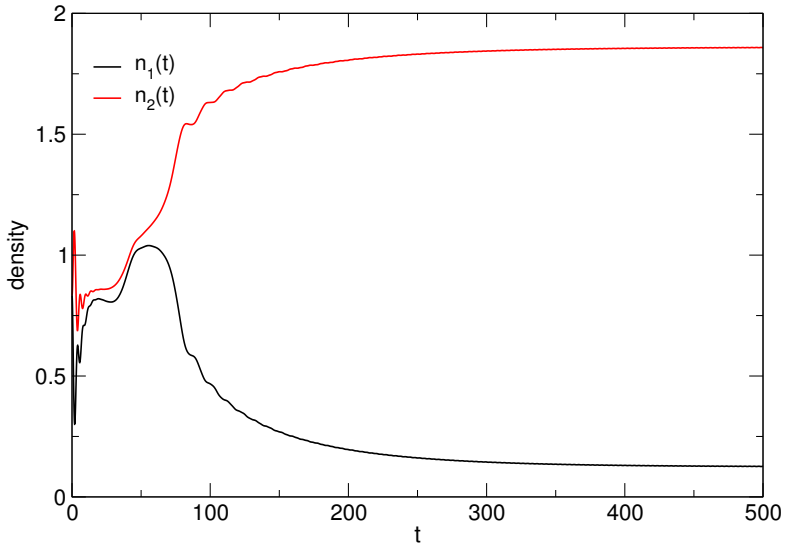

FIGURE 7.8: Densities of the first and second site for the HF approximation with the bias applied smoothly as $W_\alpha(t) = W_\alpha \sin^2(\omega_\alpha t)$ for $t < \frac{\pi}{2\omega_\alpha}$ and otherwise $W_\alpha(t) = W_\alpha$ with $\omega_\alpha = 0.04$, the other parameters are the same as the one of the middle curves in the upper left panel of Fig 7.6

sight one might be reminded of non-decaying density and current oscillations which can appear for non-interacting systems when the biased system possesses two or more bound states. However, here we work in the HF approximation and therefore the analysis of Refs. [43, 109, 110] needs to be modified, see below. Moreover, the HF density of state calculated at the average density does not posses two split-off state. On the other hand, the fact that the oscillations of the the total time-dependent density are negligible leads to presume that we have something similar to the Rabi oscillations between the two sharp levels of the Hubbard dimer. Looking at the spectral function, bottom right panel of Fig 7.5, corresponding to the solution $\tilde{n}_3$ we observe two sharp peaks at distance ~ 2.02 which is about twice as large as the frequency of the oscillations. Moreover, our further numerical investigations did not support this idea.

Some insight into the nature of these oscillations can be gained from the simple model of an *isolated* Hubbard dimer. In the HF approximation, the equation of motion for the electronic density matrix ρ of the isolated dimer reads

$$i\partial_t \rho(t) = [H_{HF}(t), \rho(t)], \tag{7.3}$$

where the HF Hamiltonian is given by

$$H_{HF}(t) = \begin{pmatrix} \varepsilon_1 + \frac{U}{2} n_1 & V_{1,2} \\ V_{1,2} & \varepsilon_2 + \frac{U}{2} n_2 \end{pmatrix} . \tag{7.4}$$

Let us define few quantities

$$\begin{aligned} \delta n &= n_1 - n_2 = \rho_{11}(t) - \rho_{22}(t) \\ J &= iV_{1,2}[\rho_{21} - \rho_{12}] \\ K &= V_{1,2}[\rho_{21} + \rho_{12}], \end{aligned} \tag{7.5}$$

for which the following equations of motion can be derived

$$\begin{aligned} \frac{d}{dt}\delta n &= 2J \\ \frac{d}{dt}\, J &= -2V_{1,2}^2\delta n + \partial h K = (-2V_{1,2}^2 + K\frac{U}{2})\delta n + \delta\varepsilon K \\ \frac{d}{dt}\, K &= -\delta h J = -\frac{UJ\delta n}{2} - \delta\varepsilon J \end{aligned} \tag{7.6}$$

where $\delta\varepsilon = \varepsilon_1 - \varepsilon_2$ and $\delta h = \delta\varepsilon + U\delta n/2$.
For the simpler case $\varepsilon_1 = \varepsilon_2$, we get $J^2 + K^2 - \frac{8V_{1,2}^2}{U}K = C$ and $K = -U/8\ (\delta n)^2 + D$ where C and D are constant numbers. In addition

$$\delta\ddot{n} = 2\dot{J} = -(4V_{1,2}^2 - KU)\delta n \tag{7.7}$$

and hence

$$\delta\ddot{n} + (4V_{1,2}^2 - UD)\delta n + \frac{U^2}{8}(\delta n)^3 = 0. \tag{7.8}$$

Here the constant D is related to the initial condition of the isolated Hubbard dimer and can be defined through the off-diagonal matrix elements of the density matrix as

$$D = V_{1,2}(\rho_{1,2}(0) + \rho_{2,1}(0)) + \frac{U}{8}(\delta n(0))^2\ . \tag{7.9}$$

We note that Eq. (7.8) is the equation of motion of a classical, anharmonic oscillator and therefore supports oscillating solutions. We now check if the model of the isolated Hubbard dimer has anything to do with the oscillations seen in our transport setup. To this end, we calculate D from Eq. (7.8), i.e., $D = \frac{\delta\ddot{n}}{\delta nU} + \frac{4V_{1,2}^2}{U} + \frac{U}{8}(\delta n)^2$, where the densities and their time-derivatives are taken from the transport calculation after the transients have died out. As Eq. (7.8) is only an approximation for the connected Hubbard dimer, D is not constant in time. Hence in order to compare the oscillation amplitudes and frequencies from the transport simulations with those resulting from Eq. (7.8) we averaged D over an oscillation period. In Fig. 7.9 we show the dependence of the oscillation frequency and amplitude for different switchings of the gate ($V_{g,1}(t) =$

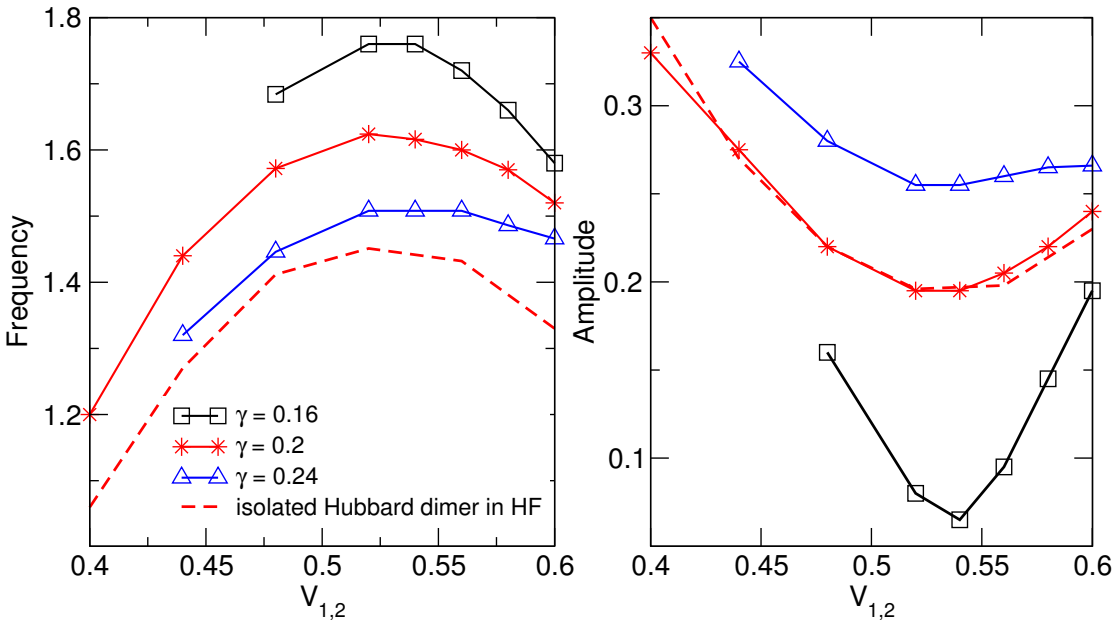

FIGURE 7.9: Oscillation frequency and amplitude of the density oscillations found in HF for certain gate switchings of the Hubbard dimer connected to biased leads as function of the hopping between the Hubbard sites. For comparison, oscillation frequencies and amplitudes are given for the isolated Hubbard dimer in HF approximation described by Eq. 7.8

$V_0 \exp(-\gamma t)$, $V_{g,2}(t) = 0$, $V_0 = 1$) as function of the hopping $V_{1,2}$ between the two sites of the Hubbard dimer connected to biased leads and compare to the corresponding solutions of Eq. (7.8). We see that both frequency and amplitude of the isolated and connected dimer behave qualitatively quite similar as function of the inter-site hopping and we conclude that the model of the isolated dimer certainly captures the physics behind these oscillations.

We also would like to point out that the regions of parameter space where the oscillations are found appear to be quite small. For most parameters the system actually does evolve towards one of the steady states of Table 7.1. In fact, the steady state corresponding to FP 3 can be reached in the long time limit by turning on the biases smoothly as $W_\alpha(t) = W_\alpha \sin^2(\omega_\alpha t)$ for $t < \frac{\pi}{2\omega_\alpha}$ and otherwise $W_\alpha(t) = W_\alpha$ with $\omega_\alpha = 0.04$ as shown in Fig 7.8. The gate is applied as $V_{g,1}(t) = \exp(-0.2t)$, $V_{g,2}(t) = 0$.

The occurrence of self-induced persistent oscillations in the HF mean field theory is likely to be favored by the short-range nature of the Hubbard interaction. In fact, we also have studied a modified version of our model where we replaced the last term of

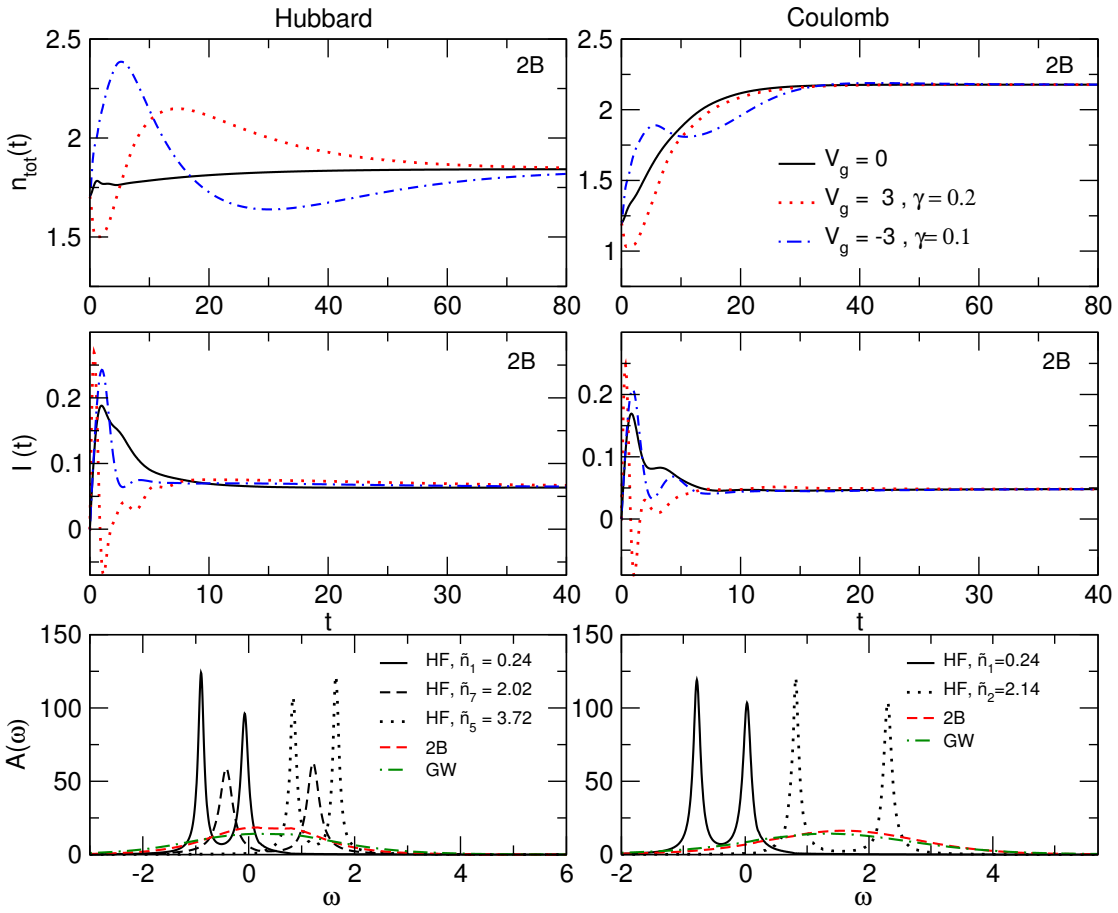

FIGURE 7.10: Densities and currents for the 2B approximation short range (Hubbard) and long range (Coulomb) interactions are used. *Lower panel*: Spectral functions for the different approximations at the end of the time propagation.

Eq. 5.2 by a more long-range, Coulomb-like interaction $\frac{1}{2}\sum_{\substack{i=1\\\sigma\sigma'}}^{2} U_{i,j}\hat{d}^{\dagger}_{i\sigma}\hat{d}^{\dagger}_{j\sigma'}\hat{d}_{j\sigma'}\hat{d}_{i\sigma}$ with

$$U_{i,j} = \begin{cases} U & i = j \\ \frac{U}{2|i-j|} & i \neq j \end{cases}. \tag{7.10}$$

In this case we have not found any oscillating solutions in the long-time limit. We have found two stable steady-state solutions accessible by time propagation. The first steady-state solution has densities $n_1 = 1.06$, $n_2 = 1.09$, the second one has $n_1 = 0.11$, $n_2 = 0.13$. The spectral functions corresponding to these solutions (see Fig 7.12) are localized around the Fermi-level of the left or right lead, respectively. The inclusion of the long range interaction destroys the states where the first peak is localized on the right lead energy band and the second peak is localized to the left lead energy band. Because the magnitude of the interaction felt by the electron on the site is now higher the density on the sites is decreased and the solution corresponding to the highest density

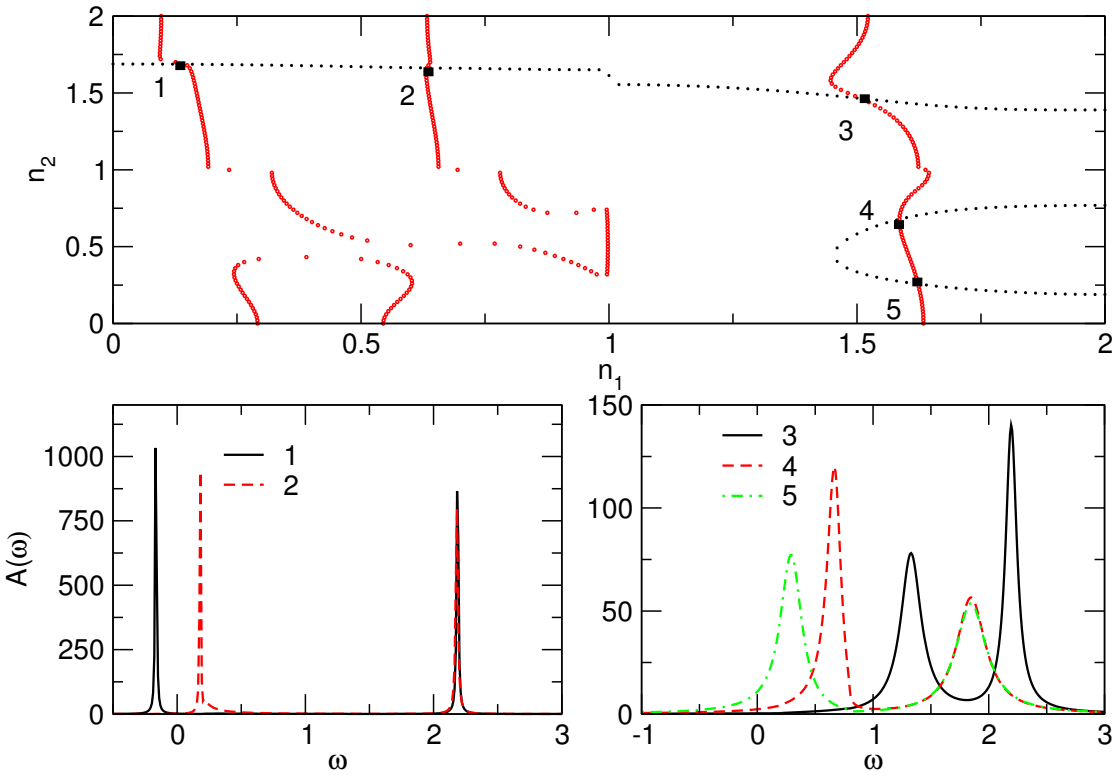

FIGURE 7.11: Upper panel: Graphical solution of the integral in Eq. 5.49. Lower panel: Spectral functions for the BALDA with Hubbard interactions corresponding to the five different steady-state solutions for the density.

FP	1	2	3	4	5
n_1	0.147	0.632	1.506	1.585	1.624
n_2	1.685	1.658	1.466	0.674	0.250

TABLE 7.2: Fixed-point (FP) solutions of Eq. 5.49 for the steady-state densities of two interacting Hubbard sites connected to two biased, non-interacting leads in the BALDA approximation (see upper panel of Fig 7.11). The parameters are: $V_{\text{link}} = 0.4$, $W_{\text{L}} = 2.2$, $W_{\text{R}} = -1.2$, $U = 2.0$, $V_{1,2} = 0.4$, $\varepsilon_\alpha = \varepsilon_F = 0$, and $\varepsilon_1^C = -0.04$, $\varepsilon_2^C = 0.2$.

is at half-filling. Also in this case we are able to switch between the two steady-states. The currents corresponding to these two solutions for the density have almost the same magnitude.

In Fig 7.12 we show the time-dependent densities and currents for the 2B approximation. Again within the correlated approximations we find only one solution for the density and current. In the lower panels of Fig 7.12 we show the spectral functions for the 2B and *GW* approximations compared to the spectral functions of the HF approximation. The 2B and *GW* spectral functions are qualitatively quite different from those of the HF approximation. Instead of the two peak structure of the HF approximation, with the 2B and *GW* approximations we have one very broad peak with much lower maximum.

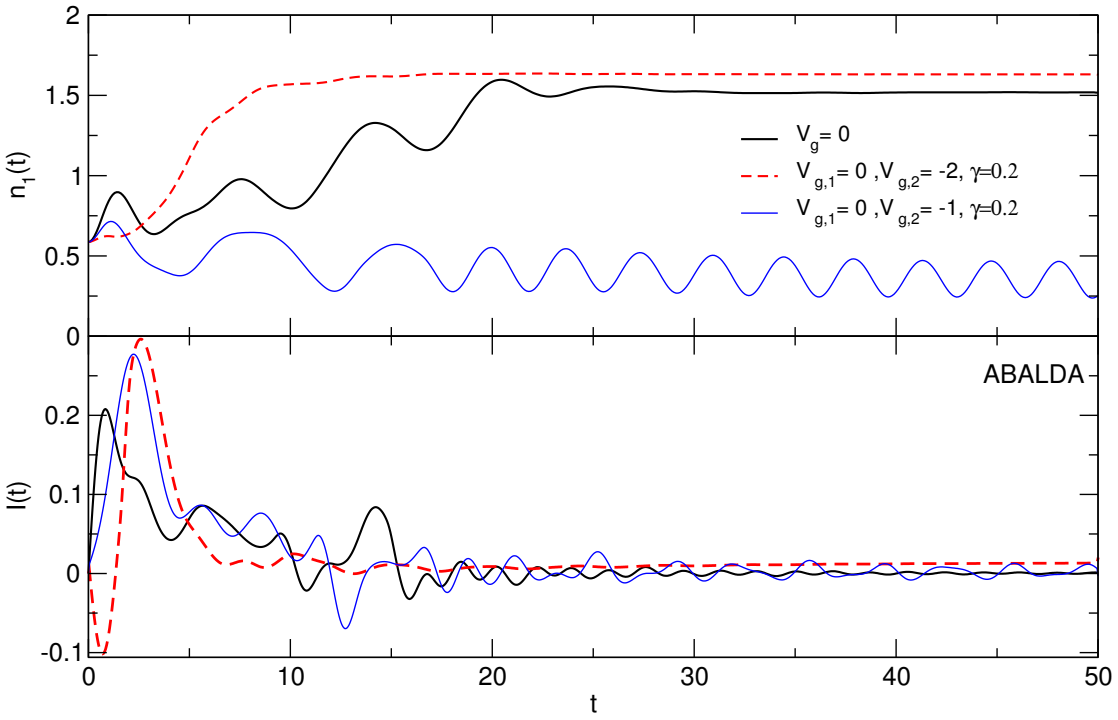

FIGURE 7.12: Time-dependent density and current for the ABALDA with different applied gates.

We also studied the possibility of multiple steady-states for the same model within the BALDA approximation. Using the same parameters as above, the BALDA has multiple solutions. However, at least one fixed point has a density on one of the dots very close to unity, exactly where the BALDA potential is discontinuous. For a single interacting dot, this discontinuity has been shown to be closely related to the Coulomb blockade phenomenon [111]. For the purposes of this chapter we avoid the regime of integer occupancy in an ABALDA treatment by changing the on-site energies of the interacting sites in an asymmetric way such that $\varepsilon_1^C = -0.04$ and $\varepsilon_2^C = 0.2$. With these modifications, the two coupled equations given by Eq. 5.49, are solved simultaneously, yielding five fixed-points (see Fig 7.11 and Table 7.2). Among these five fixed points, FP 1, FP 3, and FP 5 are stable, the other two unstable.

The spectral functions corresponding to FP 3 and FP 5 have two well separated smooth peaks, while the one corresponding to FP 1 has two sharp peaks, the first one located at $\omega_1 = -0.168$ outside the energy range of the left lead, the second one at $\omega_2 = 2.16$ outside the energy range of the right lead.

Again, the stable solutions are accessible by time propagation. Upon application of a sudden bias in the leads at $t = 0$, the system approaches the third solution if no external

gate voltage is turned on. On the other hand, if a gate voltage of the form (Eq. 7.2) is applied only to the second site, with amplitude $V_{g,2} = -2.0$ and $\gamma = 0.2$, the system attains a steady-state with a density corresponding to FP 5. As before switching between these two steady-state density is possible by changing the sign of the applied gate. A similar gate voltage applied only to the second site and smaller amplitude ($V_g = -1.0$) leads to an oscillatory time-dependent density, whose average total density is close to the one of FP 1.

The frequency of the time-dependent density is $\omega = 2.24$ which is close to the energy difference ($\omega = 2.34$) between the peaks of spectral function. Hence, these oscillations are due to the existence of bound-states in the biased interacting system. One possible way to explain the role of bound-states in the biased KS Hamiltonian is that in the long-time limit the KS potentials are time dependent (with the bound state eigenenergy differences as prominent frequencies) leading again to time-dependent currents and densities (by virtue of Floquet's theorem). This is evidently achieved in adiabatic approximations with the XC potential depending only on the local density such as the ABALDA and HF approximation.

7.3 Conclusions

In this chapter, we have investigated by means of real-time propagation within MBPT and TDDFT, the existence of multiple steady states in single and double interacting quantum dot systems connected to semi-infinite leads.

In order to find the parameter region for bistability, we first solved the self-consistent steady-state equations within the HF and BALDA approximation and determined the regime for which multiple solutions occur. We show that only the stable solutions are accessible by time propagation. Moreover, we find that by superimposing an exponentially decaying gate voltage pulse to the external bias, it is possible to reach the various stable solutions and also to switch between them. Interestingly, within adiabatic and spatially local approximations of the time-dependent exchange-correlation potential, we found special parameters for which the time-dependent current(density) exhibit persistent oscillations in the long-time limit, even though the fixed-point theorem predicts a stable steady-state solution. These oscillations die out provided the time-dependent gate or bias is applied in an adiabatic fashion. The question of when the adiabatic

and local approximation of the time-dependent exchange-correlation potential does not allow the system to reach a steady state, is still an open and interesting question. For the same parameters and driving fields, we then included dynamical XC effects by solving the Kadanoff-Baym equations with MBPT self-energies at the 2B and GW level of approximation. In all studied cases where adiabatic DFT and HF theory predict bistability *dynamical XC effects destroy the phenomenon*. Here we emphasize that we have performed 2B and *GW* calculations for many more parameter sets than those for which we have shown results here. We have found no indication for the existence of multiple steady states for any of these sets. However, due to the vastness of the parameter space, *we cannot rule out completely the possibility of multiple steady states when dynamical XC effects are included*.

We wish to point out that even though ABALDA already contains correlations it is based on two approximations: spatial locality and the adiabaticity. For any non-local but adiabatic approximation to the TDDFT functionals one could still derive a self-consistency condition for the steady-state density in the form of coupled, nonlinear equations. Because of the nonlinearity, multiple solutions, i.e., multiple steady states, can be possible. Therefore our results suggest that it is the adiabatic approximation which permits bistability while we expect that the inclusion of memory effects suppresses it. We also expect that bistable regimes induced by the electron-electron interaction only, are unlikely to be found in Hubbard or extended Hubbard model nanojunctions, and that other degrees of freedom, like nuclear motion, must be taken into account.

Chapter 8

Comparative Study of Many-Body Perturbation Theory and Time-dependent Density Functional Theory in the out-of-equilibrium Anderson Model

For the description of electron transport several numerical approaches have been developed that can deal with fully time-dependent systems [28, 30, 49, 65, 81, 82, 106, 112–117]. Among these are the tDMRG approach [118], time-dependent density functional theory [28, 30], and self-consistent many-body perturbation theory based on the Kadanoff-Baym equations [48, 65, 116]. Each of these methods has its own advantages and disadvantages. In the last two chapters, we investigated time-dependent electron transport through nanostructures described by an Anderson-like model where the interactions on the impurity site(s) are accounted for via the self-energy approximations at Hartree-Fock, second Born, GW, and T-Matrix level as well as within a time-dependent density functional scheme based on the adiabatic Bethe-Ansatz local density approximation for the exchange-correlation potential. The nonequilibrium dynamics of the Anderson model out of equilibrium is determined by real-time propagation. In this chapter, the time-dependent currents and densities obtained from the various MB approximation and also ABALDA are compared to results obtained with the tDMRG method which serves as benchmark for the approximate treatments. The tDMRG method is a numerically exact algorithm applicable to low-dimensional systems [119]. Here we used published

tDMRG results [83] as a benchmark for both the TDDFT and MBPT approaches. Such a study is expected to be valuable for gaining insight into these methods and into the direction in which each method needs to be improved. In the steady-state regime of quantum transport such comparisons of many-body and benchmark approaches were made by Wang *et al.* [88] within the GW-approximation and by Schmitt and Anders [120] at second Born and GW level. In both cases good agreement with benchmark results was found in certain parameter ranges. Here these comparisons are extended to the transient regime as well.

Many-body perturbation theory beyond HF turns out to give results in close agreement with tDMRG especially within the 2B approximation. To gain some insight about the quality of the ABALDA, we remind the reader that in Chapter 5, Eq. 5.6 is derived with the assumption that the exchange-correlation potential is zero in the leads. However, Eq. 5.6 is in principle exact only if $\mathbf{\Sigma}^R_{\rm em}$ is replaced by $\mathbf{\Sigma}^R_{\rm KS}$, i.e, when the interaction in the leads is correctly accounted for. Practically this can be done by including a finite portion of the leads into the central region, where the interactions are properly taken into account. Furthermore, most applications of TDDFT to quantum transport processes [24, 28–30, 40, 78, 105] use the adiabatic approximation which assumes that the XC potential instantaneously follows the density profile. This is a reasonable assumption when the density changes are slow on a time-scale of typical lead-to-molecule tunneling rates, and also when the switch-on times of the applied biases are small enough. However, it has also been pointed out that non-adiabatic effects can have substantial influence [40, 121] on calculated properties. In such cases there is also a need to introduce spatial non-locality in the density functional because the non-localities in space and time are strongly related by conservation laws [122]. This relation is virtually unexplored within the quantum transport context and such a comparison may help us to gain further insight into the importance of this issue.

The adiabatic approximation implies that

$$\frac{\delta v_{\rm xc}[n](t)}{\delta n(t')} = \delta(t-t')\, f_{\rm xc}(n(t)), \tag{8.1}$$

where $f_{\rm xc} = dv_{\rm xc}(n)/dn$, meaning the XC response kernel is local in time (and in space). This local and instantaneous approximation becomes valid for Hubbard systems in the limit of slowly varying density both in space and in time. These conditions are not

satisfied for the quantum transport system under consideration. Despite this fact, reasonable densities were obtained using the BALDA for finite Hubbard chains [86] and it is therefore worthwhile to try the approximation for quantum transport phenomena.

For future reference we make a connection with the many-body approach. The fully self-consistent Green function for the whole system (i.e. leads plus impurity) satisfies the following equation

$$\begin{aligned} G_{ij}(z,z') &= G^{\rm KS}_{ij}(z,z') \\ &+ \sum_{kl}\int {\rm d}\bar{z}d\bar{z}' G^{\rm KS}_{ik}(z,\bar{z})[\Sigma_{kl,{\rm xc}}(\bar{z},\bar{z}') \\ &- \delta(\bar{z},\bar{z}')\delta_{kl}v_{k,{\rm xc}}(\bar{z})]G_{lj}(\bar{z}',z'). \end{aligned} \tag{8.2}$$

Since the exact density is given by both the KS and the exact Green function, *i.e.*, $n_k(z) = -iG_{kk}(z,z^+) = -iG^{\rm KS}_{kk}(z,z^+)$, it follows that

$$\begin{aligned} \sum_k \int_{\mathcal{C}} {\rm d}\bar{z}\, G^{\rm KS}_{ik}(z,\bar{z})v_{k,{\rm xc}}(\bar{z})G_{ki}(\bar{z},z) = \\ \sum_{kl}\int_{\mathcal{C}} {\rm d}\bar{z}{\rm d}\bar{z}'\, G^{\rm KS}_{ik}(z,\bar{z})\Sigma_{kl,{\rm xc}}(\bar{z},\bar{z}')G_{li}(\bar{z}',z), \end{aligned} \tag{8.3}$$

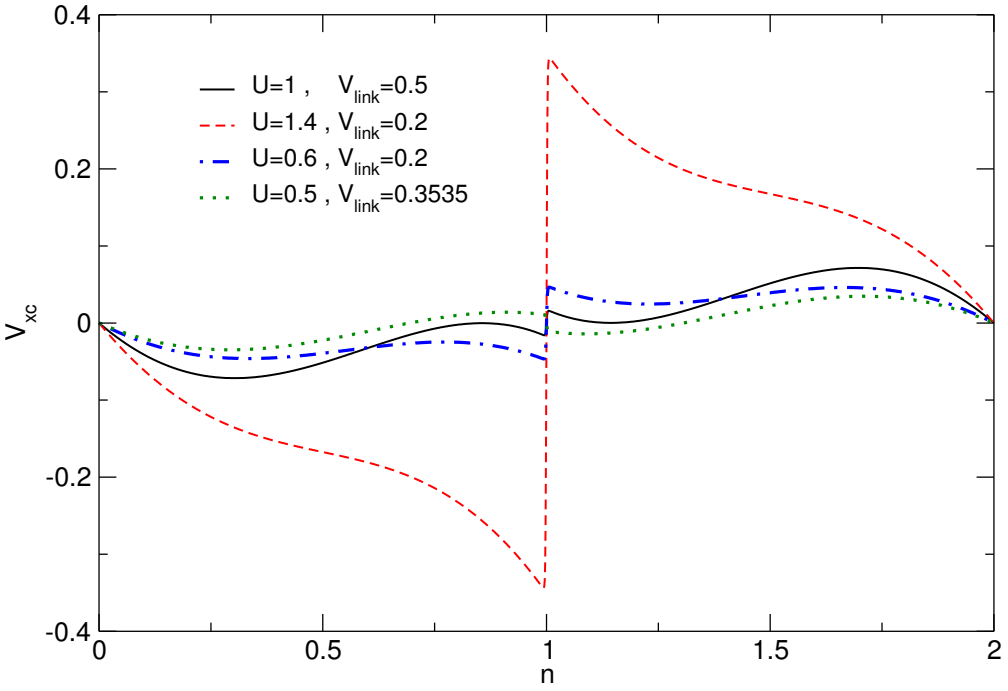

FIGURE 8.1: The BALDA XC potential as a function of the density for parameters used in the subsequent sections.

where Σ_{xc} is the many-body self-energy with the Hartree potential subtracted. If the self-energy is exact then the corresponding XC potential that solves this Sham-Schlüter equation [123] yields the exact density of the system. We see that the integral kernel on the left hand side of this equation is nonlocal in space and time. Hence, the solution of this integral equation for $v_{k,\text{xc}}$ will in general have values on any site k. This has been confirmed by recent work of Schenk *et al.* [124]. It is important to note that this is true even if the many-body interactions are restricted to the impurity site only. We therefore make an approximation if we set the XC potential to zero in the leads. We will discuss the validity of this approximation in the results section.

In MBPT one has direct access to quantities like quasiparticle spectra, lifetimes, and screened interactions which provide insight into the effects of electron correlation. In particular, the non-locality in time of the 2B, GW, and T-Matrix approximations allows for a description of dynamic XC effects and quasi-particle broadening. Furthermore, the MBPT approach can be used to derive new improved time-dependent density functionals with memory and conserving properties [125].

8.1 Transport through a Weakly Coupled Correlated Site

We perform many-body and density-functional transport calculations for the Anderson impurity model. As mentioned in last chapters, the single quantum dot model is fully specified by three parameters: the Hubbard interaction (or charging energy) U, the on-site energy ε_0 and the hopping V_{link} connecting the interacting impurity site to the leads. In the leads, the on-site energies are $\varepsilon_L = \varepsilon_R = 0$ and the hopping in the left and right lead is $V_L = V_R = V$. All parameters are given in units of the lead hopping V. For times $t < 0$ the contacted system is in the groundstate with Fermi energy ε_F. A constant bias W_α in lead $\alpha = L, R$ is suddenly switched on at $t = 0$ after which the time-dependent observables are calculated. We only consider weak coupling to the leads, *i.e.*, $V_{\text{link}} \ll V$, since in this regime the role of correlation effects is enhanced. The equilibrium Green function is obtained as the self-consistent solution of the Dyson equation [60] for different approximate many-body self-energies. In the TDDFT calculations the initial state is obtained by a self-consistent static DFT calculation [28]. For the XC potential we use the modified BALDA defined in Section 5.2.1.1.

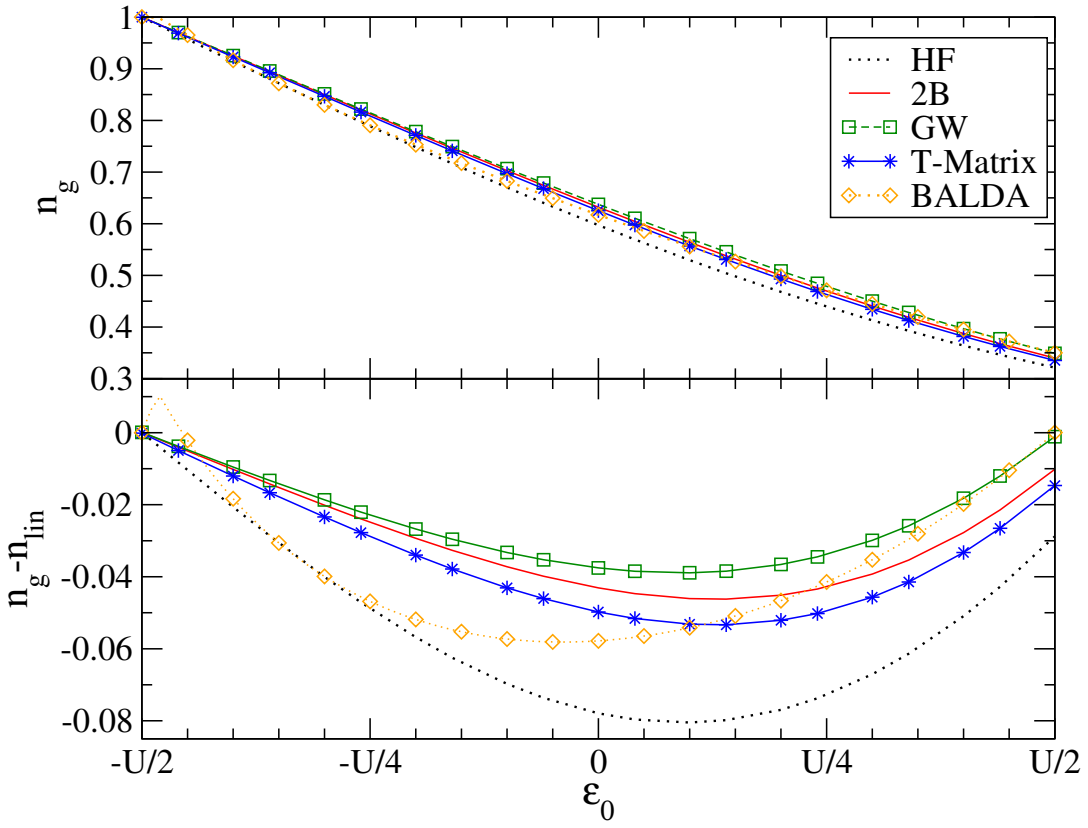

FIGURE 8.2: Groundstate density n_g on the correlated site versus the on-site energy, ε_0, for $U = 1$, $V_{\rm link} = 0.5$ and $\varepsilon_F = 0$. In the bottom panel we subtracted $n_{\rm lin}(\varepsilon_0) = a\varepsilon_0 + b$ in order to enhance the difference between the curves. The constants a and b are such that $n_{\rm lin}(-U/2) = 1$ and $n_{\rm lin}(U/2) = 0.35$.

8.1.1 Equilibrium Results

We start by considering a system with interaction $U = 1$ and coupling to leads $V_{\rm link} = 0.5$. The Fermi energy of the system is $\varepsilon_F = 0$ (half-filling). In Fig 8.2 we display the groundstate density n_g on the correlated site for all values of the on-site energy, ε_0, for the density functional BALDA and the many-body HF, 2B, GW, and T-Matrix approximations. For $\varepsilon_0 = -U/2$ the system is invariant under the particle-hole transformation $\hat{d}_{j\sigma} \to (-)^j \hat{d}^\dagger_{j\sigma}$ and therefore the exact density on the impurity site equals $n_g = 1$. This remains valid in all the approximation schemes employed. If we increase the gate potential ε_0 away from the particle-hole symmetric point, the density on the impurity site decreases almost linearly in all approximations. In order to enhance the differences between the approximations, in the bottom panel we plot $n(\varepsilon_0) - n_{\rm lin}(\varepsilon_0)$ where $n_{\rm lin}(\varepsilon_0) = a\varepsilon_0 + b$ and the constants a and b are chosen such that $n_{\rm lin}(-U/2) = 1$ and $n_{\rm lin}(U/2) = 0.35$. In the vicinity of the particle-hole symmetric point, the BALDA

has a cusp that is responsible for correlation induced density oscillations on the impurity site. This gives a time-dependent description of the Coulomb blockade (see Chapter 6). The HF approximation can describe the Coulomb blockade provided we allow the spin symmetry to be broken. The many-body approximations that we use here do not seem to be able to describe the Coulomb blockade without spin-symmetry breaking [88] although the onset of the Coulomb blockade is observed [120]. It can be concluded from the above observations that among these approximations only BALDA yields the Coulomb blockade *without* spin symmetry breaking [111]. For $\varepsilon_0 < -U/4$ the groundstate density of the interacting dot is around 0.7 which gives an XC potential close to zero as shown in Fig 8.1 and BALDA consequently differs substantially from the correlated MBPT results and follows more closely the HF curve. When ε_0 attains positive values, the correlation potential is large and negative, favoring charge accumulation (see Fig 8.1). Consequently, the BALDA deviates from HF and follows the correlated MBPT results, in particular with the GW results for ε_0 around $U/2$. As a general feature, we find that correlations favor the presence of electrons on the interacting site (for density less than 1), since the density in the BALDA and the many-body approaches is larger than the HF density for all values of the on-site energy.

8.1.2 Nonequilibrium Steady-state Results

We now shift our attention to the nonequilibrium case. In the left panel of Fig 8.3 we display the steady-state density and current (within ABALDA, HF, and 2B) for a symmetrically applied bias $W_L = -W_R = W/2$ and for three different values of the on-site energy $\varepsilon_0 = -U/2\,, 0\,, U/2$. To improve the clarity of the plot we do not display the results for GW and T-Matrix as they are, in this parameter range, in close agreement to those obtained within 2B. In the left panel of Fig 8.3 we see that the 2B, HF, and ABALDA densities are generally in good agreement with each other.

For the corresponding steady-state current, benchmark results are available from tDMRG calculations (see Ref. [83]). In the right panel of Fig 8.3 we plot the currents as a function of the bias W/U. Because the current is proportional to the overlap of the energy bands of the leads, for higher biases, *i.e.*, $W/U > 1.5$, the steady-state current decrease with increasing bias.

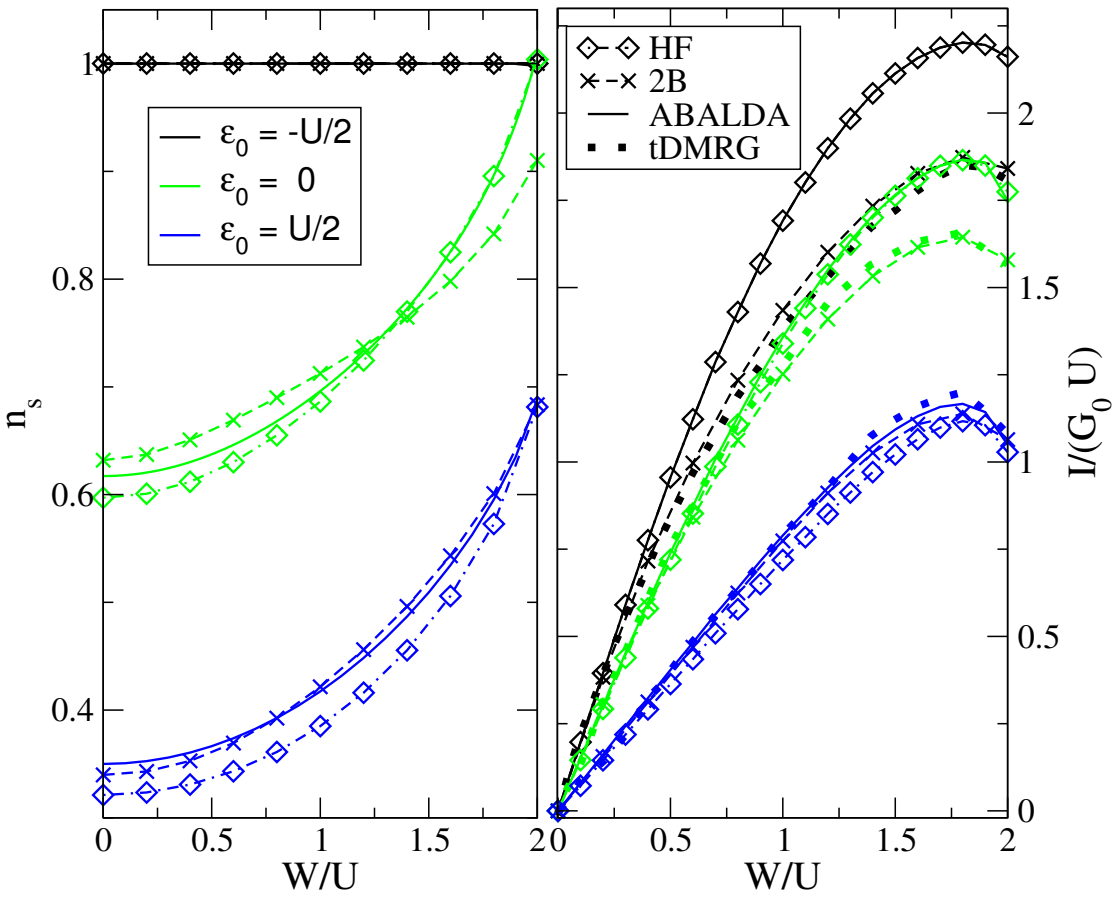

FIGURE 8.3: Steady-state density n_s (left) and current I (right) for a symmetrically applied bias $W_L = -W_R = W/2$ and for three different values of the on-site energy ε_0. The other parameters are $U = 1$, $V_{\text{link}} = 0.5$ and $\varepsilon_F = 0$.

We note that for small bias values all the approximations yield values for the current which are on top of the numerically exact tDMRG results for all on-site energies considered. However, for higher biases, only the current obtained within 2B follows closely the tDMRG values for all on-site energies. Therefore, in this range of parameters, we will use the 2B results for benchmarking the other approximations. For $\varepsilon_0 = U/2$, the HF and specially ABALDA results follow closely the tDMRG and 2B curves, and for the whole bias-range. This corresponds to small density on the dot. For higher biases and smaller on-site energies, *i.e.* $\varepsilon_0 = 0$ and $\varepsilon_0 = -U/2$, they considerably overestimate the exact results. However, the conductances, *i.e.* the initial slopes of the I-V curves in Fig 8.3, still remain in close agreement with the 2B approximation and the tDMRG approach. This agrees with the Friedel sum rule that relates the conductance to the density [126].

For the results displayed in Fig 8.4 we considered the same system parameters and

plotted the density (left panel) and the current (right panel) for an asymmetrically applied bias $W_L = W$, $W_R = 0$. The overlap between the lead energy bands starts to decrease for $W/U > 1$ and, consequently, the currents decrease with increasing bias. The steady-state densities behave similarly to the case of symmetric biases (see Fig 8.3): the ABALDA and the HF results are in agreement with 2B results except for the case of gate potential $\varepsilon_0 = 0$ at high bias. For the steady-state current (left panel) we also see the same trend: the ABALDA results are close to the HF results and overestimate the 2B results.

8.1.3 Time-dependent Results: Adiabatic Effects

We now study the performance of the different approximations in the description of transient phenomena. The results are compared to the numerically exact tDMRG data of Ref. [83], obtained for a lead-impurity hopping parameter $V_{\text{link}} = 0.3535$ and $U = 0.5$. This decrease in the hopping parameter amounts to a slight enhancement of correlations

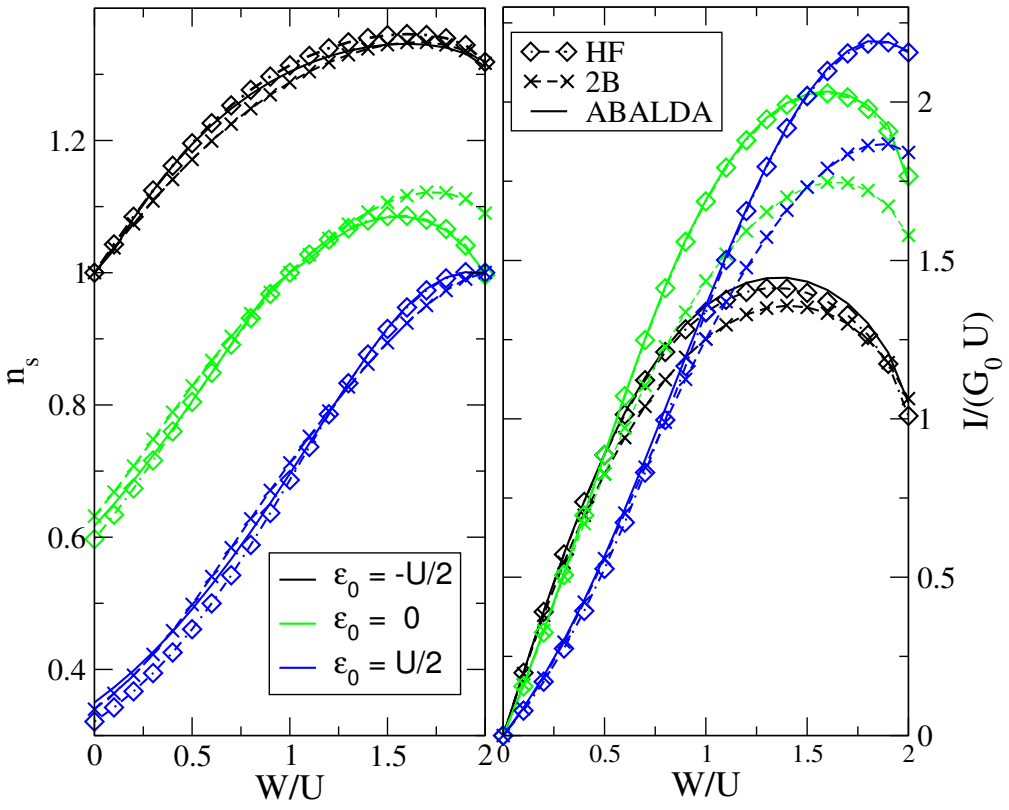

FIGURE 8.4: Steady-state density n_s (left) and current I (right) for a asymmetrically applied bias $W_L = W$, $W_R = 0$ and for three different values of the on-site energy ε_0. The other the parameters are $U = 1$, $V_{\text{link}} = 0.5$ and $\varepsilon_F = 0$.

as compared to the steady-state results of the previous section. The tDMRG calculations [83] were done for a particle-hole symmetric situation with $\varepsilon_0 = -U/2$. In addition, we compare the many-body results with ABALDA for the on-site potential $\varepsilon_0 = U/2$, which is away from the discontinuity of the $v_{\rm xc}$.

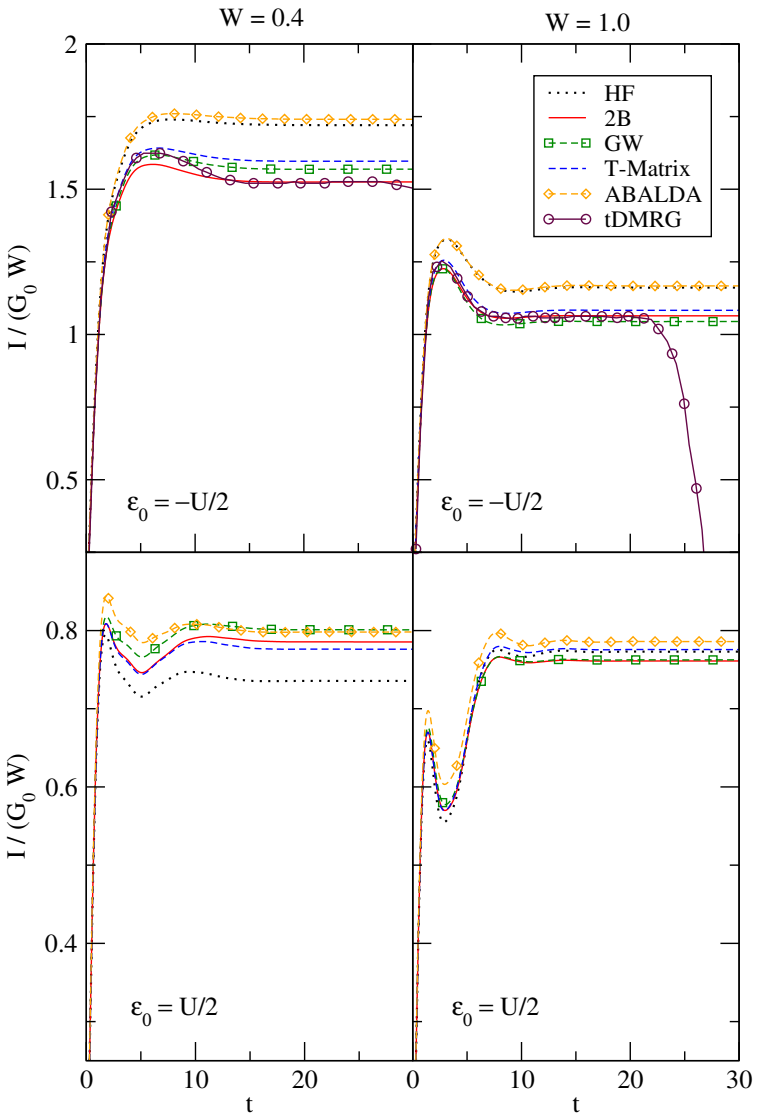

FIGURE 8.5: Transient currents for different values of the applied bias $W_L = -W_R = W/2$, $U = 0.5$ and $V_{\rm link} = 0.3535$. In the upper panels, $\varepsilon_0 = -U/2$ corresponds to the particle-hole symmetric point. In the lower panels $\varepsilon_0 = U/2$.

In the upper panels of Fig 8.5 we display the transient currents as a function of time for the various many-body approaches and the ABALDA as compared to the benchmark tDMRG data. Since the tDMRG calculations are performed on finite systems, one sees the influence of reflections at the system boundaries after a sufficiently long propagation time. The many-body results beyond HF are all in good agreement with the tDMRG

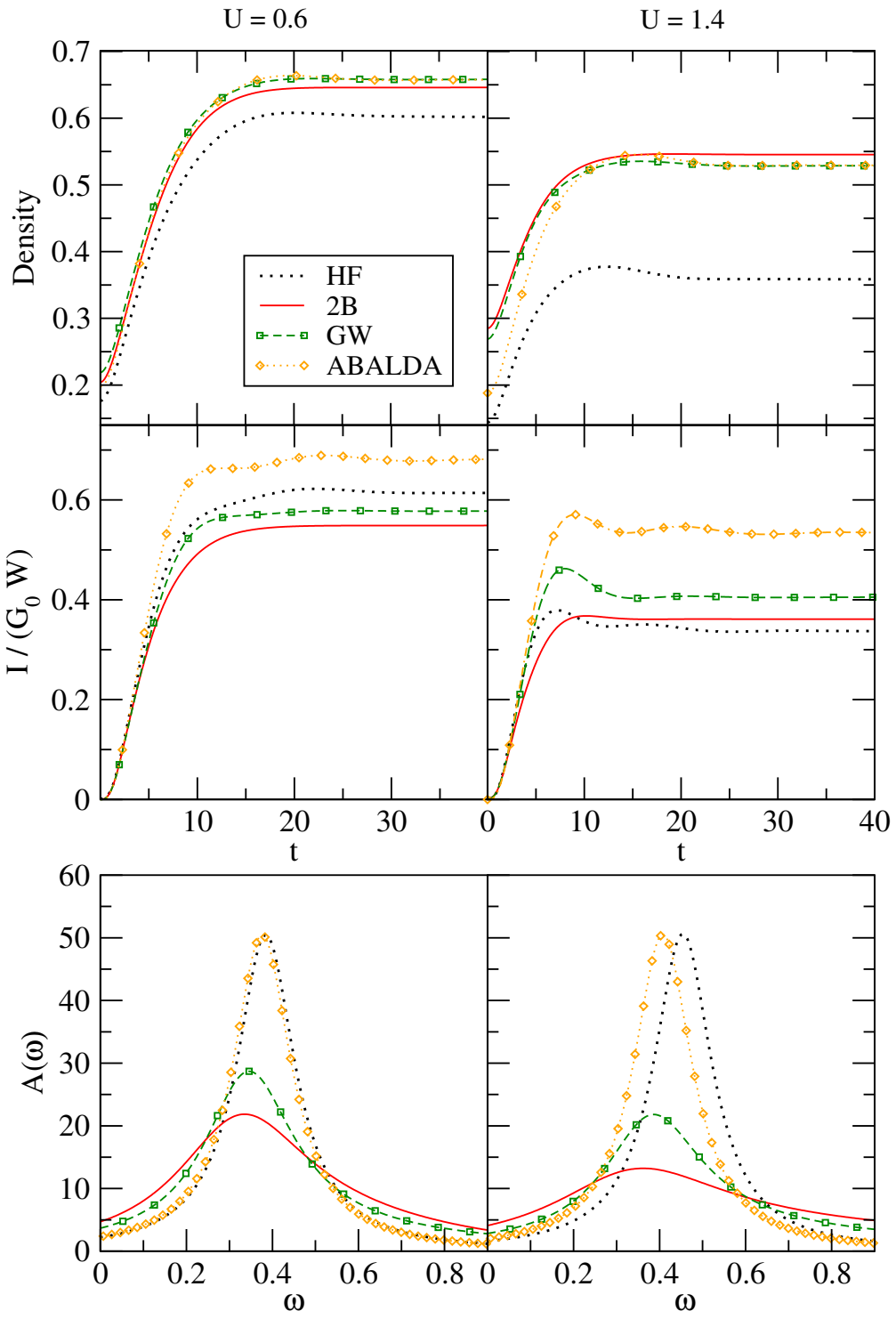

FIGURE 8.6: Time-dependent density $n_0(t)$ for a system with Fermi energy $\varepsilon_F = 0$, and $\varepsilon_0 = 0.2$, $V_{\text{link}} = 0.2$ and for different values of the charging energy $U = 0.6$ (left column), 1.4 (right column). The system is driven out of equilibrium by an external bias $W_L = 0.4$ and $W_R = 0$. The constant $G_0 = e^2/(2\pi\hbar) = 1/(2\pi)$ is the quantum of conduction in atomic units.

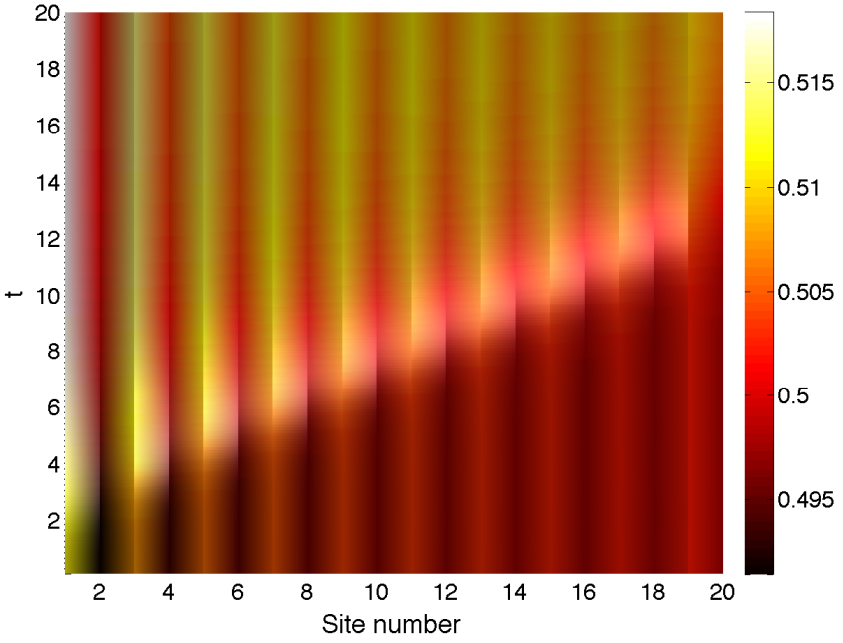

FIGURE 8.7: Time-dependent density in the right lead within the 2B approximation for a system with Fermi energy $\varepsilon_F = 0$, and $\varepsilon_0 = 0.2$, $V_{\text{link}} = 0.2$ and $U = 0.6$). The system is driven out of equilibrium by an external bias $W_L = 0.4$ and $W_R = 0$. A density wave entering the lead can be clearly observed.

results, the most accurate one being the 2B approximation. Not only the values of the steady-state current but also the characteristic bump in the transient is reasonably well-reproduced. The ABALDA and the HF approximations perform very similarly; they overestimate the values of the steady-state current and for a bias value of $W = 0.4$ they underestimate the height of the transient bump. Also the many-body approximations underestimate the height of the bump somewhat. However, the best agreement is again found for the 2B approximation. It is difficult to pinpoint the origin of the different behavior of the transient bump in the ABALDA and HF when compared to results obtained within correlated approximations. It is worth emphasizing, however, that in time-local approximations such as HF the terms responsible for the initial correlation in the current formula of Eq. 5.34, *i.e.*, the terms with components on the vertical track of the Keldysh contour, are lacking. In general these terms lead to damping and hence time-local approaches such as HF tend to overshoot the bump in the transient current [49]. In the upper left panel of Fig 8.5 such overshoots for the HF and ABALDA are probably masked by the fact that the final steady state current goes to a value that is too large. We finally like to point out that in systems with more levels the transient

structure has a more rich oscillatory time-dependence which can be used to analyze the level structure of the central molecule [49]. In these cases the differences between the HF and the correlated approaches become more visible.

In the lower panels of Fig 8.5, we display the transient currents, with the on-site energy on the impurity site being $\varepsilon_0 = U/2$. The transients show a more pronounced oscillatory behavior because of the increased energy-gap between the impurity level and the Fermi level of the right lead. This determines the oscillation frequency in the transient current (see Ref. [49]). The many-body approaches agree rather well with each other whereas the HF approximation underestimates the value of the steady-state current for lower biases. In this case the ABALDA results agree closely with the correlated many-body results. Due to the increased on-site energy $v_{\rm xc}$ becomes negative favoring charge accumulation on the Anderson impurity site (see Fig 8.1 and Section 8.1.1).

In order to increase the effects of correlation we now reduce the hopping between the interacting site and leads to $V_{\rm link} = 0.2$ and consider two different charging energies $U = 0.6$ and $U = 1.4$. We also set $\varepsilon_0 = 0.2$ and the Fermi energy to $\varepsilon_F = 0$. The system is driven out of equilibrium by a sudden switch-on of a constant, asymmetric bias $W_L = 0.4$, $W_R = 0$.

In the upper panel of Fig 8.6 we show the time-dependent density for the interacting site. For $U = 0.6$, all results obtained within correlated approximations are in close agreement to each other. Obviously, if the interaction approaches zero, ABALDA and HF are close to the MBPT approximations and all MBPT approximations become homologous. By increasing the interaction the correlated MBPT approximations and ABALDA start to detach from HF. For stronger interactions, *i.e.*, $U = 1.4$ (right panel-column), the HF density deviates considerably from the ABALDA and the many-body results.

In the middle panel of Fig 8.6 we show the time-dependent current through the right interface (from the interacting site to the lead). As expected from the discussion in Section 8.1.2 the ABALDA overestimates the current given by tDMRG and 2B. The deviation from the 2B increases with increasing the interaction. The GW approximation also shows a smaller but noticeable deviation from the 2B approximation. The agreement between the ABALDA and the many-body results deteriorates gradually with an even further increase of the charging energy. For the MBPT results, the differences in the currents when increasing the interaction can be explained with the aid of the spectral

function. We display the *steady-state* spectral functions in the lower panel of the Fig 8.6. Since the current is approximately proportional to the integral of the spectral function over the bias window (see Eq. 5.35), the highest current is given by the approximation which has most spectral weight inside the bias window. As in the case of the site densities, for small charging energies the spectral functions of all the approximations remain closer to each other.

The spectral functions of correlated MBPT approximations are broadened compared to the HF spectral functions. This is because many-body interactions lead to a fast decay of many-body states generated by adding and removing particles. More precisely, the states $|\Psi(t)\rangle = \hat{d}_H^\dagger(t)|\Psi_0\rangle$ and $|\Phi(t)\rangle = \hat{d}_H(t)|\Psi_0\rangle$ in which we add or remove a particle at time t to the impurity in the presence of a bias have decreased survival probabilities $|\langle\Psi(t)|\Psi(t')\rangle|^2$ and $|\langle\Phi(t)|\Phi(t')\rangle|^2$ for $|t-t'| \to \infty$ when we include interactions. This process is often referred to as quasi-particle scattering. When the charging energy is increased quasi-particle scattering broadens the spectral functions and lowers the intensity of the spectral peak in the case of correlated MBPT approximations [49, 66, 127].

The broadening of the HF spectral function is independent of U due to the absence of quasi-particle scattering and depends only on the embedding to the leads. The same holds true for the ABALDA spectral function which remains very close to the HF spectral function when increasing the interaction. It should be noted, however, that the ABALDA spectral function is the one of the KS system and should not be regarded as an approximation to the true spectral function. The clear broadening of the MBPT spectral functions as compared to HF demonstrates the importance of dynamical XC effects in the transient regime. Therefore, memory must be taken into account for a proper description of ultrafast time-dependent processes. In the next section, however, we show that memory is not enough to improve the results of the steady-state current and we identify a second important direction to go in order to improve the ABALDA.

8.1.4 Time-dependent Lead Densities and Non-locality

In order to gain some insight on how to cure the deficiencies of the ABALDA XC potential, so as to yield an improved time-dependent current, we argue as follows: In equilibrium, the density deep inside the leads is the same in all approximations and it is uniquely determined by the Fermi energy ε_F. Let us denote with n_g (g=groundstate)

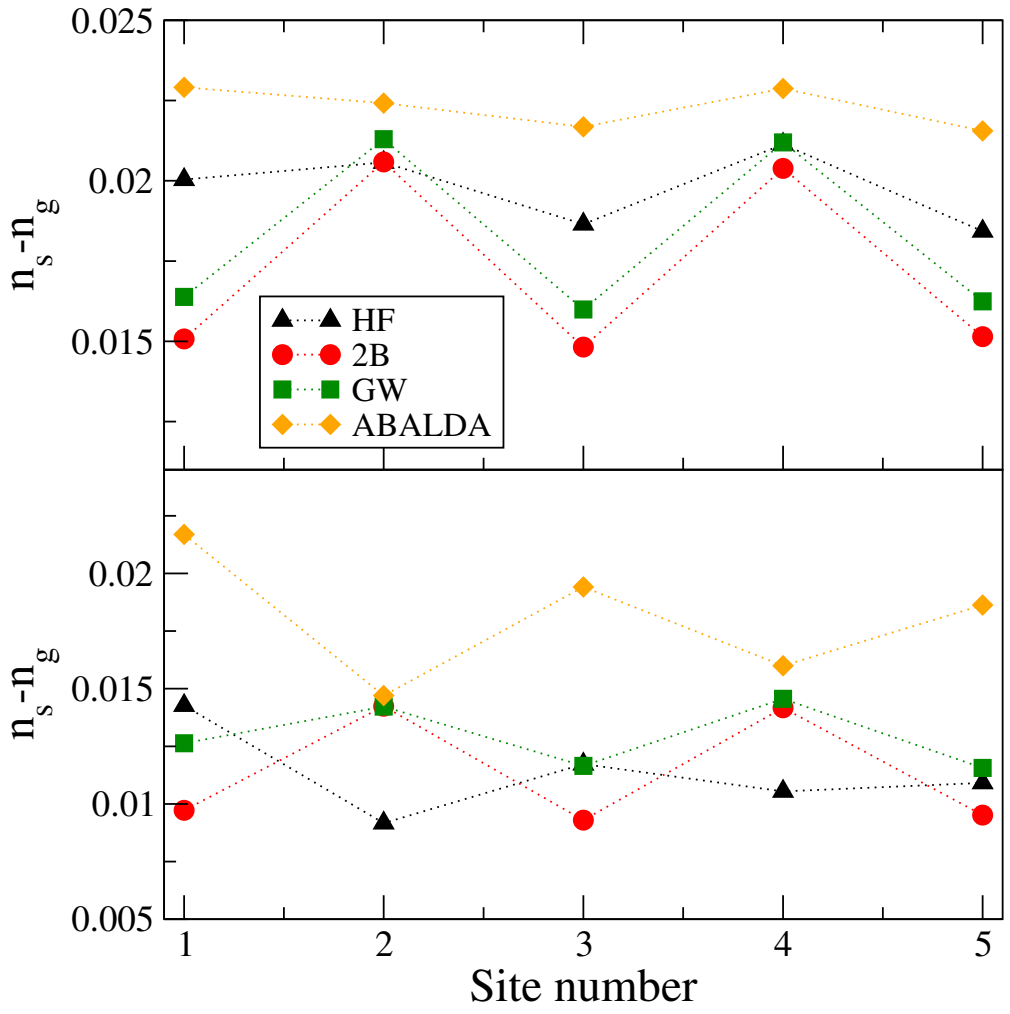

FIGURE 8.8: Difference between steady-state and groundstate density in the right lead for a system with Fermi energy $\varepsilon_F = 0$, and $\varepsilon_0 = 0.2$, $V_{\text{link}} = 0.2$ and for different values of the charging energy $U = 0.6$ (top panel) and $U = 1.4$ (bottom panel). The system is driven out of equilibrium by an external bias $W_L = 0.4$ and $W_R = 0$.

the density at a site with index j_d deep inside, say, the right lead, such that $n_j = n_g$ for all $j > j_d$. If we plot the current $I_d(t)$ to the right of j_d, no difference will be observed in the site-density until after a time t_d. This is clearly illustrated in Fig 8.7 where we show the time-dependent lead densities obtained from a 2B calculation at interaction strength $U = 0.6$ for the first 20 sites in the right lead. In the lower side of the figure we clearly see a wave front moving into the right lead.

Let us then consider an interval of the right lead that extends from j_d to $j_d + N_d$ with $N_d \gg 1$. In equilibrium the number of electrons in this interval is simply $n_g N_d$. At the time $t \sim t_d$ the current wave-front reaches the site j_d, enters inside the interval $(j_d, j_d + N_d)$ and after a time $T_d = N_d/v$ it goes out through the site $j_d + N_d$, where v

is the velocity of the density wave-front moving into the right lead

For times $t > t_d + T_d$ an equal amount of electrons enters in and exits from the interval, and a *local* steady-state is reached. The number of electrons in the considered interval is then given by

$$n_s N_d = n_g N_d + \int_{t_d}^{t_d+T_d} dt\, I_d(t) \sim n_g N_d + I_s T_d, \tag{8.4}$$

with I_s the value of the steady-state current. Taking into account that $T_d = N_d/v$ we conclude that the steady-state density deep inside the leads must be

$$n_s = n_g + I_s/v. \tag{8.5}$$

From Fig 8.7 we see that for our 2B calculation the velocity v has the value $v = 1.88$. Given the value of the current of $I_s^{\mathrm{BO}} = 0.034$ for this case ($U = 0.6$) we find that the density difference $n_s - n_g$ is approximately 0.018 which is in good agreement with the value in the upper panel of Fig 8.8. Also for the case of the $U = 1.4$ interaction strength we see from the lower panel of Fig 8.8 that the ratio of the density differences $n_s - n_g$ for ABALDA and 2B is the same as the corresponding ratio for the currents in Fig 8.6. We note that the value v is close to the Fermi velocity in the lead at half-filling as obtained from a semi-classical calculation. This is given by $v = 2V$. Equation (8.5) shows that if different approximations yield different values of the steady-state current they must also yield different values of the difference between steady-state and groundstate densities deep inside the leads. This can indeed be seen in Fig 8.8 where we plot $n_s - n_g$ for the various approximations for the first five sites in the right lead. The ordering of the density differences is identical to that of the currents in Fig 8.6. Therefore, the ABALDA overestimates the difference between steady-state and groundstate densities in the leads. However, in the regime of weak bias values, ABALDA turns out to be a quite good description of the density on the impurity site, comparable to those obtained within the many-body approximations. We thus conclude that the ABALDA xc-potential is quite accurate on the impurity site but that setting the potential to zero in the leads is a too crude approximation. As was discussed in relation to the Sham-Schlüter equation (see Eq. 8.3) the XC potential will in general have values in the leads even when the interaction is localized on the impurity site only. Hence, in order to obtain accurate values for the current within a TDDFT approach one needs an XC potential that has a nonzero value in the leads. We wish to observe that this nonlocality is different in nature from the non-local dependence of the XC potential on the density. The latter is

already implied by the conclusions of the previous section since non-locality in time and space are intimately related by conservation laws.

8.2 Conclusions

We study electron transport through an interacting Anderson impurity model within TDDFT and MBPT frameworks. Results obtained in the groundstate, transient and steady-state regimes are compared with numerically exact tDMRG values.

In the groundstate, we find that for large values of the on-site energy, the density obtained using the ABALDA XC functional is close to the densities obtained within correlated MBPT approximations. However, for smaller values of the on-site energy, the difference between the ABALDA and the correlated MBPT densities is significant, ABALDA being closer to HF in this parameter range.

In all the cases where benchmark tDMRG results are available we find that the MBPT approximations beyond HF which we considered give densities and currents close to the benchmark ones for the entire parameter range considered. This is true for both the transient and steady-state regimes. We find that in particular the 2B approximation performs very well. The transients obtained within the 2B approximation are the closest to the tDMRG ones, while the HF and ABALDA transients deviate significantly. This indicates that it is important to include memory or retardation effects to properly describe quasi-particle scattering in non-equilibrium transport.

Regarding the TDDFT approach we find that the ABALDA performs very well and yields accurate densities on the interacting site in the weak bias limit but in many cases overestimates the steady-state currents. This problem can be linked to an overestimation of the lead-densities within the ABALDA. The results strongly suggest that it is necessary to go beyond the local approximation and that one especially needs to take into account XC-potentials that are nonlocal and non-zero within the leads. Improved functionals should therefore be nonlocal functionals in space. As has been clearly pointed out by Vignale [122], this implies that the functionals also need to be nonlocal in time in order to satisfy basic conservation laws. The construction of such functionals is a clear challenge for the future. One way to proceed would be to make connections to many-body theory with conserving approximations [125].

Chapter 9

Outlook

By treating quantum transport in an explicitly time-dependent way, we have found several physically different situations where no steady state is reached. Bound-state oscillations are found even for non-interacting electrons while other cases, such as the Coulomb blockade oscillations, appear only when sufficiently strong on-site interactions are present.
Unfortunately, all these results have been obtained within certain approximations. Since exact solutions of the transport problem are hardly available, it is difficult to assess to what extent the time-dependent phenomena found in this thesis are a consequence of the approximations made.

Comparing TDDFT and MBPT we have found that, generally speaking, MBPT introduces damping which annihilates the phenomenon of multistability, and may also affect the oscillatory behavior in the Coulomb blockade regime and in the presence of bound states. However, MBPT within present approximations for the many-body self-energy appears to over emphasize damping. Whether TDDFT or MBPT is closer to the truth is currently unknown.

To assess both TDDFT and MBPT approaches, numerically exact solutions of the many-body problem will be indispensable. The first attempts along this line, namely using either tDMRG [83, 128] or time-dependent quantum Monte Carlo [129] or a hierarchical equation of motion approach [130] are beginning to appear.

The future will show the truth.

Bibliography

[1] A. Aviram, and M. Ratner, Chem. Phys. Lett. **29**, 277 (1974).

[2] R. M. Metzger, B. Chen, U. Höpfner, M. V. Lakshmikantham, D. Vuillaume, T. Kawai, X. Wu, H. Tachibana, T. V. Hughes, H. Sakurai, J. W. Baldwin, C. Hosch, M. P. Cava, L. Brehmer, and G. J. Ashwell, J. Am. Chem. Soc. **119**, 10455 (1997).

[3] C. Zhou, M. R. Deshpande, M. A. Reed, L. Jones, and J. M. Tour, Appl. Phys. Lett. **71**, 611 (1997).

[4] E. Runge, and E. K. U. Gross, Phys. Rev. Lett. **52**, 997 (1984).

[5] T. Ando, Z. Phys. B **26**, 263 (1977).

[6] T. Ando, Solid State Commun **21**, 133 (1977).

[7] V. Peuckert, J. Phys.C **11**, 4945 (1978).

[8] A. Zangwill, and P. Soven, Phys. Rev. A **21**, 1561 (1980).

[9] B. M. Deb, and S. K. Ghosh, J. Chem. Phys. **77**, 342 (1982).

[10] S. K. Ghosh, and B. M. Deb, Chem. Phys. **71**, 295 (1982).

[11] S. K. Ghosh, and B. M. Deb, Theoret. Chim. Acta **62**, 209 (1983).

[12] S. K. Ghosh, and B. M. Deb, J. Mol. Struct. (Theochem) **103**, 163 (1983).

[13] L. Bartolotti, Phys. Rev. A **24**, 1661 (1981).

[14] R. van Leeuwen, Phys. Rev. Lett. **82**, 3863 (1999).

[15] P. Hohenberg, and W. Kohn, Physical Review **136**, B864 (1964).

[16] F. von Oppen, J. Koch, *Novel quantum transport effects in single-molecule transistors*, Advances in Solid State Physics **46** (Springer-Verlag, Berlin, 2006).

[17] N. Lang, Phys. Rev. B **52**, 5335 (1995).

[18] K. Hirose, and M. Tsukada, Phys. Rev. B **51**, 5278 (1995).

[19] J. Seminario, A. Zacarias, and J. Tour, J. Am. Chem. Soc. **120**, 3970 (1998).

[20] J. Taylor, H. Guo, and J. Wang, Phys. Rev. B **63**, 245407 (2001).

[21] J. J. Palacios, A. J. Pérez-Jiménez, E. Louis, and J. Vergés, Phys. Rev. B **64**, 115411 (2001).

[22] Y. Xue, S. Datta, and M.A. Ratner, Chem. Phys. **281**, 151 (2002).

[23] M. Brandbyge, J. Mozos, P. Ordejon, J. Taylor, and K. Stokbro, Phys. Rev. B **65**, 165401 (2002).

[24] F. Evers, F. Weigend, and M. Koentopp, Phys. Rev. B **69**, 235411 (2004).

[25] S. V. Faleev, F. Leonard, D. A. Stewart, and M. van Schilfgaarde, Phys. Rev. B **71**, 195422 (2005).

[26] M. Koentopp, C. Chang, K. Burke, and R. Car, J. Phys. Condens. Matter **20**, 083203 (2008).

[27] M. Petersilka, U. J. Gossmann, and E. K. U. Gross, Phys. Rev. Lett. **76**, 1212 (1996).

[28] G. Stefanucci, and C.-O. Almbladh, Europhys. Lett. **67**, 14 (2004).

[29] G. Stefanucci, and C.-O. Almbladh, Phys. Rev. B **69**, 195318 (2004).

[30] S. Kurth, G. Stefanucci, C.-O. Almbladh, A. Rubio, and E. K. U. Gross, Phys. Rev. B **72**, 035308 (2005).

[31] D. Nitsche, Diploma thesis, Freie Universität Berlin, 2008.

[32] A. Castro, M. Marques, and A. Rubio, The Journal of chemical physics **121**, 3425 (2004).

[33] H. Appel and E. K. U. Gross, Quantum Simulations of Complex Many-Body Systems: From Theory to Algorithms, J. Grotendorst, D. Marx, A. Muramatsu, ed(s), (John von Neumann Institute for Computing, NIC Series, Volume 10, 2002) p. 255-268.

[34] R. Landauer, IBM J. Res. Develop. **1**, 233 (1957).

[35] M. Büttiker, Phys. Rev. Lett. **57**, 1761 (1986).

[36] Y. Meir, and N. S. Wingreen, Phys. Rev. Lett. **68**, 2512 (1992).

[37] M.A. Reed, C. Zhou, C.J. Muller, T.P. Burgin, and J.M. Tour, Science **278**, 252 (1997).

[38] N. Bushong, N. Sai, and M. D. Ventra, Nano Lett. **5**, 2569 (2005).

[39] C. G. Sanchez, M. Stamenova, S. Sanvito, D. R. Bowler, A. P. Horsfield, and T. N. Todorov, J. Chem. Phys. **124**, 214708 (2006).

[40] N. Sai, N. Bushong, R. Hatcher, and M. D. Ventra, Phys. Rev. B **75**, 115410 (2007).

[41] M. Cini, Phys. Rev. B **22**, 5887 (1980).

[42] A. Dhar, and D. Sen, Phys. Rev. B **73**, 085119 (2006).

[43] G. Stefanucci, Phys. Rev. B **75**, 195115 (2007).

[44] A. Blandin, A. Nourtier, and D. W. Hone, J. Phys. (Paris) **37**, 369 (1976).

[45] P. Danielewicz, Ann. Phys. (NY) **152**, 239 (1984).

[46] S.-H. Ke, H. Baranger, and W. Yang, Phys. Rev. B **70**, 085410 (2004).

[47] R. Li, J. Zhang, S. Hou, Z. Qian, Z. Shen, X. Zhao, and Z. Xue, Chem. Phys. **336**, 127 (2007).

[48] P. Myöhänen, A. Stan, G. Stefanucci, and R. van Leeuwen, Europhys. Lett. **84**, 67001 (2008).

[49] P. Myöhänen, A. Stan, G. Stefanucci, and R. van Leeuwen, Phys. Rev. B **80**, 115107 (2009).

[50] L. Kadanoff, and G. Baym, *Quantum Statistical Mechanics* (BenjaminNew York, 1962).

[51] N. E. Dahlen, and R. van Leeuwen, Phys. Rev. Lett. **98**, 153004 (2007).

[52] A. Stan, N. E. Dahlen, and R. van Leeuwen, J. Chem. Phys. **130**, 224101d (2009).

[53] M.A.L. Marques, C.A. Ullrich, F. Nogueira, A. Rubio, K. Burke, and E. K. U. Gross, *Time-Dependent Density Functional Theory* (SpringerHeidelberg, 2006).

[54] E. Lieb, and F. Wu, Phys. Rev. Lett. **20**, 1445 (1968).

[55] N. Lima, L. Oliveira, and K. Capelle, Europhys. Lett. **60**, 601 (2002).

[56] L. Keldysh, Sov. Phys. JETP **20**, 1965 (1965).

[57] G. Baym, Phys. Rev. **127**, 1391 (1962).

[58] N. E. Dahlen, and R. van Leeuwen, J. Chem. Phys. **122**, 164102 (2005).

[59] L. Hedin, Phys. Rev. **139**, 796 (1965).

[60] A. Stan, N. E. Dahlen, and R. van Leeuwen, J. Chem. Phys. **130**, 114105 (2009).

[61] A. L. Fetter, and J. D. Walecka, *Quantum theory of many-particle systems* (Dover PublicationsNew York, 1971).

[62] R. van Leeuwen, N. E. Dahlen, G. Stefanucci, C.-O. Almbladh, and U. von Barth, Lect. Notes Phys. **706**, 33 (2006).

[63] N. E. Dahlen, A. Stan, and R. van Leeuwen, J. Phys., Conf.Ser. **35**, 324 (2005).

[64] P. Myöhänen, A. Stan, R. van Leeuwen, and G. Stefanucci, J. Phys.: Conf. Ser. **220**, 012017 (2010).

[65] M. P. von Friesen, C. Verdozzi, and C.-O. Almbladh, Phys. Rev. Lett. **103**, 176404 (2009).

[66] K. Thygesen, and A. Rubio, Phys. Rev. B **77**, 115333 (2008).

[67] C. J. Gorter, Physica **17**, 777 (1951).

[68] I. Kulik, and R. Shekhter, Zh. Eksp. Teor. Fiz. **68**, 623 (1975).

[69] See e.g. *Single Charge Tunneling: Coulomb Blockade Phenomena in Nanostructures*, H. Grabert and M. H. Devoret (eds.), NATO ASI Series B 234 (Plenum, New York, 1992) and K. Phoa, J. B. Neaton, V. Subramanian, Nano Lett. **9**, 3225 (2009).

[70] M. D. Ventra, *Electrical Transport in Nanoscale Systems* (Cambridge University PressCambridge, 2008).

[71] V. S. K. Phoa, J. B. Neaton, Nano Lett. **9**, 3225 (2009).

[72] S. Gustavsson, R. Leturcq, M. Studer, I. Shorubalko, T. Ihn, K. Ensslin, D.C. Driscoll, and A.C. Gossard, Surf. Sci. Rep **64**, 191 (2009).

[73] C. Beenakker, Phys. Rev. B **44**, 1646 (1991).

[74] R. Berkovits, F. von Oppen, and J. Kantelhardt, Europhys. Lett. **68**, 699 (2004).

[75] P. Schmitteckert, and F. Evers, Phys. Rev. Lett. **100**, 086401 (2008).

[76] C. Toher, A. Filippetti, S. Sanvito, and K. Burke, Phys. Rev. Lett. **95**, 146402 (2005).

[77] K. Capelle, M. Borgh, K. Karkkainen, and S. Reimann, Phys. Rev. Lett. **99**, 010402 (2007).

[78] K. Burke, R. Car, and R. Gebauer, Phys. Rev. Lett. **94**, 146803 (2005).

[79] C. Verdozzi, G. Stefanucci, and C.-O. Almbladh, Phys. Rev. Lett. **97**, 046603 (2006).

[80] C.-L. Cheng, J. Evans, S. Jeremy, and T. V. Voorhis, Phys. Rev. B **74**, 155112 (2006).

[81] X. Zheng, F. Wang, C. Yam, Y. Mo, and G. Chen, Phys. Rev. B **75**, 195127 (2007).

[82] P. Bokes, F. Corsetti, and R. W. Godby, Phys. Rev. Lett. **101**, 046402 (2008).

[83] F. Heidrich-Meisner, A. Feiguin, and E. Dagotto, Phys. Rev. B **79**, 235336 (2009).

[84] V. Moldoveanu, A. Manolescu, and V. Gudmundsson, New J. Phys. **11**, 073019 (2009).

[85] N. Lima, M. Silva, L. Oliveira, and K. Capelle, Phys. Rev. Lett. **90**, 146402 (2003).

[86] C. Verdozzi, Phys. Rev. Lett. **101**, 166401 (2008).

[87] The steady-state solution achieved in TDDFT with an adiabatically switched bias clearly depends on the approximation used for the TD XC functional. Only for adiabatic approximations to the XC functional the steady-state current is the same as the L+DFT one [28, 131, 132].

[88] X. Wang, C. D. Spataru, M. S. Hybertsen, and A. J. Millis, Phys. Rev. B **77**, 045119 (2008).

[89] J. F. Dobson, J, M. J. Bünner, and E. K. U. Gross, Phys. Rev. Lett. **79**, 1905 (1997).

[90] I. V. Tokatly, Phys. Rev. B **75**, 125105 (2007).

[91] M. Lein, and S. Kümmel, Phys. Rev. Lett. **94**, 143003 (2005).

[92] V. J. Goldman, and D. C. Tsui, Phys. Rev. Lett. **58**, 12 (1987).

[93] J. O. Sofo, and A. Balsero, Phys. Rev. B **42**, 7292 (1990).

[94] T. Fiig, and A. P. Jauho, Surface Science **267**, 392 (1992).

[95] P. L. Pernas, and F. Florens, Phys. Rev. B **47**, 4779 (1993).

[96] Z. Dai, and J. Ni, Phys. Lett. A **342**, 272 (2005).

[97] F. W. Sheard, and G. A. Toombs, Appl. Phys. Lett. **52**, 15 (1988).

[98] A. Zaslavsky, V.J. Goldman, D.C. Tsui, and J.E. Cunningham, Appl. Phys. Lett. **53**, 1408 (1988).

[99] N. Zou, M. Willander, I. Linnerud, U. Hanke, K. A. Chao, and Y. M. Galperin, Phys. Rev. B **49**, 2193 (1994).

[100] C. Zhang, Appl. Phys. Lett. **78**, 4187 (2001).

[101] A. A. Dzhioev, and D. S. Kosov, J. Chem. Phys. **135**, 174111 (2011).

[102] J. Chen, M.A. Reed, A.M. Rawlett, and J.M. Tour, Science **286**, 1550 (1999).

[103] J. Chen, and M. A. Reed, Chem. Phys. **281**, 127 (2002).

[104] C. F. A. Negre, P. A. Gallay, and C. G. Sánchez, Chem. Phys. Lett. **460**, 220 (2008).

[105] R. Baer, T. S. andS. Ilani, and D. Neuhauser, J. Chem. Phys. **120**, 3387 (2004).

[106] X. Zheng, G. Chen, Y. Mo, S. Koo, H. Tian, C. Yam, and Y. Yan, J. Chem. Phys. **133**, 114101 (2010).

[107] C.Y. Yam, X. Zheng, G.H. Chen, Y. Wang, T. Frauenheim, and T. Tiehaus, Phys. Rev. B **83**, 245448 (2011).

[108] Y. A. Kuznetsov, *Elements of Applied Bifurcation Theory* (Springer-VerlagNew York, 1995).

[109] E. Khosravi, G. Stefanucci, S. Kurth, and E. K. U. Gross, Phys. Chem. Chem. Phys **11**, 4535 (2009).

[110] E. Khosravi, S. Kurth, G. Stefanucci, and E. K. U. Gross, Appl. Phys. A **93**, 355 (2008).

[111] S. Kurth, G. Stefanucci, E. Khosravi, C. Verdozzi, and E. K. U. Gross, Phys. Rev. Lett. **104**, 236801 (2010).

[112] S. A. Gurvitz, and Y. Prager, Phys. Rev. B **53**, 15932 (1996).

[113] V. Moldoveanu, V. Gudmundsson, and A. Manolescu, Phys. Rev. B **76**, 165308 (2007).

[114] D. Ryndyk, R. Gutierrez, B. Song, and G. Cuniberti, Springer Berlin Heidelberg **93**, 213 (2009).

[115] S. Andergassen, V. Medenand, H. Schoeller, J. Splettstoesser, and M. Wegewijs, Nanotechnology **21**, 272001 (2010).

[116] M. P. von Friesen, C. Verdozzi, and C.-O. Almbladh, Phys. Rev. B **82**, 155108 (2010).

[117] A. Brandschädel, G. Schneider, and P. Schmitteckert, Annalen der Physik **522**, 657 (2010).

[118] E. Boulat, H. Saleur, and P. Schmitteckert, Phys. Rev. Lett. **101**, 140601 (2008).

[119] U. Schollwöck, Reviews of modern physics **77**, 259 (2005).

[120] S. Schmitt, and F.B. Anders, Phys. Rev. B **81**, 165106 (2010).

[121] G. Vignale, and M. D. Ventra, Phys. Rev. B **79**, 014201 (2009).

[122] G. Vignale, and W. Kohn, Phys. Rev. Lett. **77**, 2037 (1996).

[123] R. van Leeuwen, Phys. Rev. Lett. **76**, 3610 (1996).

[124] S. Schenk, P. Schwab, M. Dzierzawa, and U. Eckern, Phys. Rev. B **83**, 115128 (2011).

[125] U. von Barth, N. E. Dahlen, R. van Leeuwen, and G. Stefanucci, Phys. Rev. B **72**, 235109 (2005).

[126] H. Mera, K. Kaasbjerg, Y. M. Niquet, and G. Stefanucci, Phys. Rev. B **81**, 035110 (2010).

[127] A.-M. Uimonen, E. Khosravi, G. Stefanucci, S. Kurth, R. van Leeuwen, and E. K. U. Gross, Journal of Physics, Conf.Ser. **220**, 012018 (2010).

[128] J. Eckel, F. Heidrich-Meisner, S. Jakobs, M. Thorwart, M. Pletyukhov, and R. Egger, New J. Phys. **12**, 043042 (2010).

[129] P. Werner, T. Oka, M. Eckstein, and A. J. Millis, Phys. Rev. B **81**, 035108 (2010).

[130] J. Jin, X. Zheng, and Y. Yan, J. Chem. Phys. **128**, 234703 (2008).

[131] M. Koentopp, K. Burke, and F. Evers, Phys. Rev. B **73**, 121403 (2006).

[132] G. Stefanucci, S. Kurth, A. Rubio, and E. K. U. Gross,*Molecular and Nano Electronics: Analysis, Design, and Simulation*, ed. by J. Seminario (Elsevier, Amsterdam, 2006).

Deutsche Kurzfassung

Der Standardansatz für Quantentransport vereint den Landauer-Buettiker Formalismus mit der Grundzustands-Dichtefunktionaltheorie (DFT). Die Grundannahme hierbei ist, dass bei konstanter Spannung letztendlich ein zeitunabhängiger Zustand (steady state) erreicht wird. Wir werden hier aufzeigen, dass diese Annahme im Allgemeinen nicht gültig ist, und einige Beispiele geben, bei denen innerhalb verschiedener Näherungen kein zeitunabhängiger Zustand erreicht wird. In diesen Fällen ist eine explizit zeitabhängige Beschreibung des Elektronentransports notwendig. Hierzu vewenden wir die zeitabhängige Dichtefunktionaltheorie (TDDFT) sowie die Vielteilchen-Störungstheorie (MBPT). Für den nicht-wechselwirkenden Fall zeigen wir analytisch und numerisch, dass das Vorhandensein von gebundenen Zuständen anhaltende und lokalisierte Stromoszillationen hervorruft. Diese können deutlich grösser als der stationäre Anteil des Stromes sein. Es zeigt sich, dass der Beitrag der gebundenen Zustände zur zeitlich gemittelten Dichte vom zeitlichen Ablauf abhängt und eine elementare Definition der dynamischen Besetzungszahlen von gebundenen Zuständen ermöglicht. Im Falle von Elektronentransport durch wechselwirkende Nanokontakte mit angelegter Spannung führt die Unstetigkeit des Austauschkorrelationspotentials der DFT zu einem dynamischen Zustand, welcher durch korrelationsinduzierte Oszillationen im Regime der Coulomb-Blockade charakterisiert wird. Zusätzlich kann die zeitabhängige Methode bei multistabilen Systemen beschreiben, ob und wie man reversibel zwischen verschiedenen stabilen Lösungen der stationären Zustandsgleichung wechseln kann, indem man eine passende zeitabhängige Gate-Spannung anlegt. Die numerischen Berechnungen in diesem Regime zeigen, dass eine zeit- und ortslokale Näherung für das Austausch-Korrelations-Potential der TDDFT zu ungedämpften Oszillationen im Strom führt, selbst wenn eigentlich ein stationärer Zustand erwartet wird. Ausserdem befassen wir uns mit dem grundsätzlichen Problem, ob das Bistabilitätsphänomen fortbesteht, wenn man dynamische Austausch-Korrelations-Effekte in Betracht zieht. Wir vergleichen unsere Ergebnisse der TDDFT und MBPT

eines Modellsystems mit denen aus der Methode der zeitabhängigen Dichtematrix Renormalisierungsgruppe. Wir bekommen dadurch Einblicke in die Leistungsfähigkeit der verschiedenen in dieser Arbeit verwendeten Näherungen.

Acknowledgment

It is a pleasure to convey my appreciation to all the people whose contribution in different ways, have made this thesis possible.

First of all I would like to express my deepest gratitude to my supervisor Prof. Dr. E. K. U. Gross, who supported me throughout my PhD work with his encouragement, stimulating suggestions and also the freedom he gave to find my own pathways. I have profited enormously from his unique way of thinking and special way of explaining physics. Thank you Hardy for all the great discussions we had, for your novel ideas, guidance, and most importantly for making the AG-Gross such a nice and fun place to be.

I gratefully acknowledge Prof. Dr. Felix von Oppen for accepting the role as second referee and for taking the time to read the thesis. Similarly, I would like to thank all other members of the committee for the time they have invested.

I am very grateful to Prof. Dr. Stefan Kurth for all his help, many fruitful discussions and specially, for co-advising my thesis during the first years of my PhD.

It was a great pleasure to work in close collaboration with Dr. Gianluca Stefanucci. I gained a lot from his deep knowledge of physics, novel ideas and would like to thank him for numerous enlightening discussions we have had.

I would like to thank the group of Prof. Robert van Leeuwen in Jyväskylä Finland, specially Prof. van Leeuwen, Anna-Maija Uimonen and Dr. Adrian Stan, for many exciting discussions we had on our joint projects. I profited a lot from their deep understanding of many-body physics. I also like to thank Dr. Claudio Verdozzi for wonderful discussions we had on the Coulomb blockade project and also Danilo Nitsche, Klaus Pototzky for many general and constructive discussions about quantum transport.

Many thanks to Dr. Jan Werschnik for his very kind support during the initial period of my work in AG-Gross in Berlin.

My special thanks go to Gabriele Herrmann, the group secretary in Berlin, not only for helping on bureaucratic matters, but also for being so kind and lovely and making my first years in Germany such a memorable time.

In my daily work I have been blessed with a friendly and cheerful group of colleagues. I would like to thank Andrea Floris, Sangeeta Sharma, Angelica Zacarias, Antonio Sanna, Esa Räsänen, Florian Eich, Kay Dewhurst, David Jacob, Heiko Appel, Stefan Kurth and Hossein Mirhosseini for their supports and the whole group for the very friendly atmosphere not only at work but also numerous social gatherings.

I feel really lucky for having amazing friends like Javad, Somi, Raheleh, Maziar, Ali Barandov, Ali Akbari, Padideh, Faegheh, Yegane, Hossien, Somi, Pari and ... Thank you all for being there for me whenever I needed you and also for all the wonderful moments we shared together.

Very special thanks to Hedieh and Majid for all their support and kindness. Majid, thank you for showing me how to be full of life and energy despite all the hardships. I will never forget your indelible dance ...

Baba joon and maman joonam, you are my real treasure in life. Without your unconditional love, endless kindness and constant support and encouragement, the completion of this thesis would have been impossible. I love you more than words can express. Amir-Hossein and Emad thank you for everything you taught me and for always supporting your younger sister.

Last but not least, my very special thanks to my best friend Ali! Ali what can I say about you?! We have started this journey together in 1998 and gone through its ups and downs together. Thanks for standing by my side through this sometimes daunting journey. I love you!

Lebenslauf

For reasons of data protection, the curriculum vitae is not published in the electronic version

Publications

• E. Khosravi, A.-M. Uimonen, A. Stan, G. Stefanucci, S. Kurth, R. van Leeuwen, E. K. U. Gross

Correlation effects in bistability at the nanoscale: steady state and beyond

Phys. Rev. B **85**, 075103 (2012)

This paper was selected as an Editors' Suggestion.

• A.-M. Uimonen, E. Khosravi, A. Stan, G. Stefanucci, S. Kurth, R. van Leeuwen, E. K. U. Gross

Comparative study of many-body perturbation theory and time-dependent density functional theory in the out-of-equilibrium Anderson model

Phys. Rev. B **84**, 115103 (2011).

• S. Kurth, G. Stefanucci, E. Khosravi, C. Verdozzi, E. K. U. Gross

Dynamical Coulomb blockade and the derivative discontinuity of time-dependent density functional theory

Phys. Rev. Lett. **104**, 236801 (2010).

This paper was featured in a Physics Viewpoint at Physics "Spotlighting exceptional research" Physics 3, 47 (2010).

This paper was selected as an Editors' Suggestion.

• A.-M. Uimonen, E. Khosravi, G. Stefanucci, S. Kurth, R. van Leeuwen, E. K. U. Gross

Real-time switching between multiple steady-states in quantum transport

Journal of Phys.: Conf. Ser. **220**, 012018 (2010).

• E. Khosravi, G. Stefanucci, S. Kurth, E. K. U. Gross

Bound States in Time-Dependent Quantum Transport: Oscillations and Memory Effects in Current and Density

Phys. Chem. Chem. Phys. **11**, 4535 (2009).

• E. Khosravi, S. Kurth, G. Stefanucci, E. K. U. Gross

The role of bound states in time-dependent quantum transport

Appl. Phys. A **93**, 355 (2008).